

**UNIVERSIDADE DE SÃO PAULO
INSTITUTO DE QUÍMICA**

Programa de Pós-Graduação em Ciências Biológicas (Bioquímica)

LILIAN CRISTINA COSTA ALECRIM DE OLIVEIRA

**Um estudo de biologia de sistemas da retina
angiogênica: identificação de novas vias e
marcadores moleculares relevantes para doenças
dependentes da angiogênese**

Versão Corrigida da Tese

São Paulo

Data do Depósito na SPG:

16/02/2023

LILIAN CRISTINA COSTA ALECRIM DE OLIVEIRA

**Um estudo de biologia de sistemas da retina
angiogênica: identificação de novas vias e
marcadores moleculares relevantes para doenças
dependentes da angiogênese**

*Tese apresentada ao Instituto de Química da
Universidade de São Paulo para obtenção do
Título de Doutora em Ciências - Ciências
Biológicas (Bioquímica)*

Área: Bioquímica

Orientador: Prof. Dr. Ricardo José Giordano

São Paulo

2023

Autorizo a reprodução e divulgação total ou parcial deste trabalho, por qualquer meio convencional ou eletrônico, para fins de estudo e pesquisa, desde que citada a fonte.

Ficha Catalográfica elaborada eletronicamente pelo autor, utilizando o programa desenvolvido pela Seção Técnica de Informática do ICMC/USP e adaptado para a Divisão de Biblioteca e Documentação do Conjunto das Químicas da USP

Bibliotecária responsável pela orientação de catalogação da publicação:
Marlene Aparecida Vieira - CRB - 8/5562

A366e Alecrim, Lilian Costa
Um estudo de biologia de sistemas da retina angiogênica: identificação de novas vias e marcadores moleculares relevantes para doenças dependentes da angiogênese / Lilian Costa Alecrim. - São Paulo, 2023.
122 p.

Tese (doutorado) - Instituto de Química da Universidade de São Paulo. Departamento de Bioquímica.
Orientador: Giordano, Ricardo José

1. Angiogênese. 2. Retinopatia. 3. Biologia de sistemas. 4. Lipidômica. 5. Proteômica. I. T. II. Giordano, Ricardo José , orientador.



Universidade de São Paulo
Instituto de Química

"Um estudo de biologia de sistemas da retina angiogênica:
identificação de novas vias e marcadores moleculares relevantes
para doenças dependentes da angiogênese"

LILIAN CRISTINA COSTA ALECRIM DE OLIVEIRA

Tese de Doutorado submetida ao Instituto de Química da Universidade de São Paulo como parte dos requisitos necessários à obtenção do grau de Doutora em Ciências obtido no Programa Ciências Biológicas (Bioquímica) - Área de Concentração: Bioquímica.

Prof. Dr. Ricardo José Giordano
(Orientador e Presidente)

APROVADO(A) POR:

Profa. Dra. Graziella Eliza Ronsein
IQ - USP

Prof. Dr. Emer Suavinho Ferro
ICB - USP

Prof. Dr. Isaias Glezer
UNIFESP

SÃO PAULO
24 de março de 2023

Dedico este trabalho ao meu “paidrinho” José Carlos (in memoriam) e a toda a minha família, com todo o meu amor e gratidão por tudo que fizeram por mim.

AGRADECIMENTOS

A Deus, por ter me guiado durante esses anos, me iluminando e me dando força nos momentos difíceis, principalmente nos de saudade da minha família.

Ao meu orientador, Prof. Dr. Ricardo José Giordano, por ter me dado a oportunidade de integrar ao seu grupo de pesquisa. Muito obrigada por toda dedicação, ensinamentos, apoio no desenvolvimento da tese e, principalmente, pela paciência com alguém que transitou da área de ensino para a de pesquisa em bioquímica.

À Prof.^a Dra. Sayuri Miyamoto, por disponibilizar o seu laboratório para a realização da análise lipídômica e pelas contribuições nas análises e escrita do artigo.

À Prof.^a Dra. Graziella Eliza Rosein, por permitir realizar a análise de proteômica em seu laboratório, por esclarecer dúvidas e pelos ensinamentos de proteômica.

À minha querida amiga Fenny, que foi muito receptiva com a minha chegada ao laboratório e me acompanhou no difícil início, me ensinando as principais técnicas do laboratório. Obrigada pelos ensinamentos, dicas e pela parceria na vida.

Ao Alex, que das aulas de Bioquímica Avançada se tornou um grande amigo e companheiro no trabalho de lipidoma. Obrigada pelos momentos de distrações, lazer, desabafos de pós-graduação e por compartilhar seus conhecimentos sobre lipídeos comigo.

Aos companheiros de laboratório e de IQ, os quais tornaram os dias mais felizes e divertidos: Luis, Heloíse, Samantha, Paulo, André, Carlos e, em especial, à Erika, pelas conversas e muitos experimentos realizados juntas.

À Dra. Leila Magalhães, por me ensinar a delicada técnica de dissecação de retina.

À equipe técnica: Alessandra, Ednailson, Célia, Layla, Flávia, Renata e Maria Luiza pelo apoio indispensável que deram no desenvolvimento deste trabalho.

À técnica de laboratório Dra. Mariana Pereira Massafra, pela gentileza em me acompanhar nos protocolos do proteoma e no tratamento de dados.

Ao Milton e ao Vanderlei, por todo suporte com os assuntos de secretaria.

À minha amada grande família, que sempre esteve torcendo por mim, a todos os tios, tias, primos e primas, pelo carinho, apoio e por sempre me incentivar a ir em busca de conhecimentos.

À minha mãe, por todo amor, dedicação e suporte, e à minha avó “mãe Maria”, pelo cuidado, amor incondicional e por ser a minha inspiração de sabedoria.

Ao meu amado namorado, Caio, que de amigo de laboratório se tornou o meu companheiro de vida. Obrigada por todo amor, carinho, parceria, companhia, decisões tomadas juntos e esportes no CEPE.

Aos amigos que sempre me acompanham, independente da distância: Deise, João Raul, Dani e Thaís.

Ao professor de Bioquímica no meu último ano de graduação, Dr. Anderson Soares. Foi um privilégio ser sua aluna. Suas explicações e didática impecável foram essenciais para ampliar a minha visão e tomar a decisão de seguir nessa área fascinante.

À CAPES pela bolsa cedida e à FAPESP pelo financiamento do projeto.

*“Mas é preciso ter força, é preciso ter raça
É preciso ter gana sempre
Quem traz no corpo a marca
Maria, Maria mistura a dor e a alegria*

*Mas é preciso ter manha, é preciso ter graça
É preciso ter sonho sempre
Quem traz na pele essa marca
Possui a estranha mania de ter fé na vida”*

(Fernando Brant e Milton Nascimento)

RESUMO

Alecrim, L.C., **Um estudo de biologia de sistemas da retina angiogênica: identificação de novas vias e marcadores moleculares relevantes para doenças dependentes da angiogênese.** 2023. 122p. Tese - Programa de Pós-Graduação em Ciências Biológicas (Bioquímica). Instituto de Química, Universidade de São Paulo, São Paulo.

A angiogênese é a formação de novos vasos sanguíneos a partir dos já existentes, processo que contribui para a saúde, mas que também participa de doenças humanas. Câncer e retinopatias são exemplos destas doenças e para as quais medicamentos antiangiogênicos já se mostraram eficazes para seus tratamentos. No entanto, esses medicamentos ainda apresentam eficácia limitada e nem todos os pacientes respondem à terapia. Por isso, é urgente compreender melhor os mecanismos moleculares da angiogênese para o desenvolvimento de uma nova geração de inibidores angiogênicos. Uma das dificuldades para estudar a angiogênese se dá pelo fato dos vasos sanguíneos crescerem dentro de tecidos, o que nem sempre é facilmente reproduzido no laboratório. Por isso, modelos animais são importantes para estudar a angiogênese. Dentre eles, destacamos o OIR (*oxygen-induced retinopathy*), modelo animal que reproduz vários aspectos da retinopatia da prematuridade, doença dependente de angiogênese. Em trabalhos anteriores, demonstramos que o transcriptoma do modelo OIR pode ser utilizado para prever a gravidade de outra doença dependente da angiogênese: o câncer de mama. Neste trabalho de tese, expandimos estes estudos determinando o proteoma e o lipidoma do modelo OIR, integrando-os com os dados já existentes de transcriptoma, para construir um modelo de biologia de sistema da retina angiogênica. Este modelo permitiu identificar uma assinatura lipídica da angiogênese patológica que favorece a formação de gotículas lipídicas e produção de ácido de mead (*mead acid*), um marcador de deficiência de ácidos graxos essenciais. Corroborando esses dados, a análise proteômica também revelou uma abundância de proteínas relacionadas com o metabolismo e vias de lipoproteínas, colesterol, quilomicrons e triacilglicerol. Em resumo, a integração dos resultados de diferentes tecnologias de ômicas numa plataforma de biologia de sistema permitiu uma melhor compreensão das bases moleculares da angiogênese patológica, com a identificação de vias e marcadores moleculares para o desenvolvimento de novas alternativas terapêuticas e diagnósticas para as doenças dependentes da angiogênese, como câncer e retinopatias.

Palavras-chave: Angiogênese, retinopatia, transcriptômica, lipidômica, proteômica, biologia de sistemas.

ABSTRACT

Alecrim, L.C., **A systems biology study of the angiogenic retina: identification of novel pathways and molecular markers relevant to angiogenesis-dependent diseases.** 2023. 122p PhD Thesis - Graduate Program in Biochemistry. Instituto de Química, Universidade de São Paulo, São Paulo.

Angiogenesis is the formation of new blood vessels from existing ones, a process that contributes to health, but which also participates in human diseases. Cancer and retinopathies are examples of these diseases and for which antiangiogenic drugs have already proven effective for their treatments. However, these drugs still have limited effectiveness and not all patients respond to therapy. Therefore, it is urgent to better understand the molecular mechanisms of angiogenesis for the development of a new generation of angiogenic inhibitors. One of the difficulties in studying angiogenesis is due to the fact that blood vessels grow within tissues, which is not always easily reproduced in the laboratory. Therefore, animal models are important to study angiogenesis. Among them, we highlight the OIR (oxygen-induced retinopathy), an animal model that reproduces several aspects of retinopathy of prematurity, an angiogenesis-dependent disease. In previous works, we demonstrated that the transcriptome of the OIR model can be used to predict the severity of another angiogenesis-dependent disease: breast cancer. In this thesis work, we expand these studies by determining the proteome and lipome of the OIR model, integrating them with the already existing transcriptome data, to build a system biology model of the angiogenic retina. This model allowed identifying a lipid signature of pathological angiogenesis that favors the formation of lipid droplets and the production of mead acid, a marker of essential fatty acid deficiency. Corroborating these data, the proteomic analysis also revealed an abundance of proteins related to the metabolism and pathways of lipoproteins, cholesterol, chylomicrons and triacylglycerol. In summary, the integration of results from different omics technologies into a system biology platform allowed a better understanding of the molecular bases of pathological angiogenesis, with the identification of pathways and molecular markers for the development of new therapeutic and diagnostic alternatives for dependent diseases of angiogenesis, such as cancer and retinopathies.

Keywords: Angiogenesis, retinopathy, transcriptomics, lipidomics, proteomics, systems biology.

SUMÁRIO

1. INTRODUÇÃO	9
1.1 ANGIOGÊNESE	9
1.2. FAMÍLIA DO FATOR VEGF	10
1.3. A RETINA COMO MODELO DE ESTUDO DA ANGIOGÊNESE PATOLÓGICA	13
1.4. O USO DE TÉCNICAS ÔMICAS PARA A IDENTIFICAÇÃO DE NOVOS ALVOS ANGIOGÊNICOS	15
1.4.1. Transcriptoma	15
1.4.2. Lipidoma	16
1.4.3. Proteoma	19
2. OBJETIVOS	21
3. CAPÍTULO 1	22
4. CAPÍTULO 2	46
5. CAPÍTULO 3	84
5.1. MATERIAIS E MÉTODOS	84
5.1.1. Animais	84
5.1.2. Amostras de retinas no modelo animal de OIR	84
5.1.3. Preparo das amostras para a análise proteômica	84
5.1.4. Análise por espectrometria de massas	85
5.1.5. Busca das proteínas e análise dos dados da proteômica de <i>shotgun</i>	86
5.2. RESULTADOS PRÉVIOS	88
5.2.1. Variáveis que influenciam o proteoma	90
5.2.2. Identificação de proteínas diferencialmente produzidas na angiogênese fisiológica e patológica	94
5.2.3. Processos biológicos enriquecidos na retinopatia	99
5.2.4. Proteoma, lipidoma e transcriptoma convergem no metabolismo de gotículas de gordura	104
5.3. DISCUSSÃO	106
6. CONCLUSÃO DA TESE	111
7. REFERÊNCIAS	112
8. APÊNDICE	119

1. INTRODUÇÃO

1.1. ANGIOGÊNESE

A partir da ideia do médico Judah Folkman, que em 1971 propôs que o crescimento de tumores seria dependente da formação de vasos sanguíneos para alimentar e nutrir as células tumorais, surgiu o campo de pesquisa em angiogênese (FOLKMAN, 1971). A importância da formação de vasos sanguíneos associados ao crescimento tumoral já havia sido observada anteriormente (IDE; BAKER; WARREN, 1939), mas foram as pesquisas pioneiras do Dr. Folkman que alavancaram o campo da angiogênese com a identificação do TAF (*Tumor Angiogenic Factor*) e a demonstração de que sem angiogênese, tumores ficam num estado de dormência (FOLKMAN, 1971). Isso o fez sugerir que a inibição da angiogênese poderia ser uma nova alternativa terapêutica para o tratamento do câncer. Há dois tipos básicos de processos de formação dos vasos sanguíneos: vasculogênese e angiogênese. Na vasculogênese ocorre a formação de vasos sanguíneos a partir de células progenitoras e na angiogênese os vasos se formam (germinam e bifurcam) a partir de vasos já existentes. Esta distinção é importante porque é a angiogênese que persiste na vida adulta, uma vez que, de forma geral, a vasculogênese ocorre preferencialmente na fase embrionária (CARMELIET, 2005; CARMELIET; JAIN, 2011).

A angiogênese é essencial para vários processos fisiológicos importantes, tais como: ciclo reprodutivo feminino (menstruação, ovulação, formação de placenta), inflamação e cicatrização. Em condições fisiológicas, a angiogênese ocorre de forma localizada e restrita ao tempo necessário para a conclusão do processo. Mas a angiogênese também pode estar associada a processos patológicos. Neste caso, a angiogênese patológica se torna um processo crônico, resultando em vasos irregulares, desordenados e, muitas vezes, hemorrágicos.

Como mencionado, foram os estudos pioneiros do médico Judah Folkman, que alavancaram os estudos em angiogênese, levando diversos laboratórios pelo mundo a entrarem neste campo de pesquisa em busca de um melhor entendimento dos fatores envolvidos e dos mecanismos moleculares da angiogênese. Com isso, agentes terapêuticos capazes de inibir a neovascularização patológica puderam então ser desenvolvidos. Isso ganhou uma importância ainda maior quando se constatou que outras doenças, não-neoplásicas, também dependem da formação de vasos sanguíneos; essas doenças foram denominadas de "doenças dependentes de angiogênese" (CARMELIET, 2003; FOLKMAN, 2007). Exemplos destas doenças são: retinopatias (edema macular diabético, degeneração

macular relacionada à idade e a retinopatia da prematuridade), endometriose, artrite reumatoide e psoríase.

1.2. FAMÍLIA DO FATOR VEGF

Dentre os diversos fatores envolvidos na angiogênese, o VEGF (Fator de Crescimento Endotelial Vascular), também conhecido como VEGF-A, tem papel central no processo. Ele faz parte de uma família de potentes fatores de crescimento estimuladores do crescimento de células endoteliais e reguladores angiogênicos, que inclui cinco membros: VEGF-A, VEGF-B, VEGF-C, VEGF-D e o fator de crescimento placentário (PIGF) (ADAMS; ALITALO, 2007). O VEGF desempenha uma função essencial na formação de vasos sanguíneos, sendo necessário para o crescimento, migração e sobrevivência de células endoteliais (KOWANETZ; FERRARA, 2006). A importância da molécula de VEGF na formação de vasos é evidenciada pela demonstração de que a deleção de um único alelo do gene que codifica para VEGF resulta em morte do embrião por ausência de vasos sanguíneos (CARMELIET et al., 1996).

Os membros da família do VEGF ligam-se de forma seletiva e diferenciada a três receptores tirosina quinase (VEGFR-1, VEGFR-2 e VEGFR-3), assim como as neuropilinas (NRP-1 e NRP-2), que agem como co-receptores destas moléculas. A atividade de VEGF é mediada, principalmente, pela interação com o receptor VEGFR-2. Esta interação promove a auto fosforilação do domínio tirosina quinase de VEGFR-2, e consequente ativação de diversas cascatas de sinalização intracelular, resultando na proliferação e diferenciação de células endoteliais (ADAMS; ALITALO, 2007). A interação, entre VEGF e seu receptor VEGFR-2 é considerada a principal via de sinalização positiva do processo angiogênico e animais deficientes em VEGFR-2 morrem nos primeiros dias de vida uterina devido a uma ausência absoluta de vasos sanguíneos (SHALABY et al., 1995).

O receptor VEGFR-1 é o que interage com mais alta afinidade com VEGF, mas devido à baixa atividade de tirosina quinase, exerce menor ativação intracelular (ELLIS; HICKLIN, 2008). Animais deficientes em VEGFR-1 morrem nos primeiros dias de vida uterina devido à proliferação exacerbada de células endoteliais sugerindo que a falta de VEGFR-1 provoca um excesso de VEGF livre capaz de ativar o receptor VEGFR-2 (FONG et al., 1995). Já camundongos expressando VEGFR-1 sem o domínio de tirosina quinase não têm o desenvolvimento e angiogênese comprometidos, indicando que a sinalização deste receptor é dispensável para o processo angiogênico (HIRATSUKA et al., 1998). Acredita-se,

então, que o VEGFR-1 funcione como um modulador da angiogênese, sequestrando VEGF e diminuindo sua disponibilidade para interagir com VEGFR-2.

A produção de fator de crescimento placentário (PlGF) e VEGF-B, ligantes de VEGFR-1, aumenta a disponibilidade de VEGF para ativar o receptor VEGFR-2, induzindo angiogênese. A presença dos ligantes PlGF e VEGF-B e do receptor VEGFR-1 no processo de angiogênese mostra que estes atuam como reguladores positivos da ligação e atividade de VEGF via ativação de VEGFR-2. Porém, camundongos que não expressam PlGF, ou VEGF-B ou expressam somente o VEGFR-1 sem os domínios transmembrânicos e intracelular são viáveis e apresentam angiogênese fisiológica normal. No entanto, na angiogênese patológica a deficiência de PlGF, VEGF-B e VEGFR-1 podem ser notadas. Observou-se que o crescimento de tumores em animais deficientes em PlGF ou expressando VEGFR-1 sem os domínios transmembrânicos e intracelular é reduzido (LUTTUN; TJWA; CARMELIET, 2002). A ausência de PlGF e VEGF-B reduz significativamente a vascularização e sobrevivência de vasos em modelos animais de retinopatias (KOWANETZ; FERRARA, 2006). Assim, VEGFR-1 e seus ligantes PlGF e VEGF-B são alvos importantes para inibir a angiogênese patológica.

O outro receptor tirosina quinase, VEGFR-3, interage com VEGF-C e VEGF-D, sendo expresso preferencialmente em células endoteliais linfáticas e está envolvido na linfangiogênese (ELLIS; HICKLIN, 2008). Dados mais recentes, porém, demonstram a expressão de VEGFR-3 também em células endoteliais de vasos sanguíneos, particularmente, durante a angiogênese, nas células de ponta (*tip cells*), as quais são células presentes nas extremidades dos novos vasos e que guiam o processo migratório do vaso sanguíneo em formação. Estas células possuem longos filamentos citoplasmáticos (filopódios) ricos em VEGFR-2 e VEGFR-3, além de outros receptores, utilizados para sentir as pistas moleculares do ambiente, como por exemplo, gradientes de VEGF, e orientar o processo migratório.

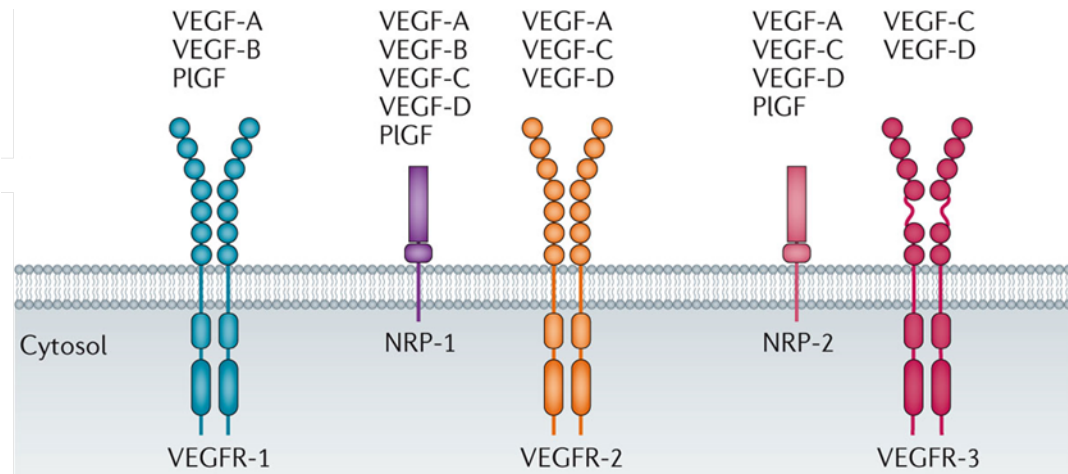


Figura 1. VEGF e seus receptores regulam a angiogênese. O VEGF (também conhecido como VEGF-A) é o membro fundador de uma família de fatores de crescimento e principal mitógeno para células endoteliais. A família compreende VEGF, VEGF-B, VEGF-C, VEGF-D, VEGF-E e fator de crescimento placentário (PIGF). Os membros da família VEGF ligam-se aos receptores tirosina quinase VEGFR-1, VEGFR-2 e VEGFR-3. Vários membros também se ligam a receptores não tirosina quinase da família da neuropilina (NRP), NRP-1 e NRP-2, que funcionam como co-receptores para os VEGFRs (Adaptado de LANGE et al., 2016).

Devido a sua importância no processo de angiogênese, VEGF e seus receptores têm sido os alvos principais para o desenvolvimento de agentes antiangiogênicos (ADAMS; ALITALO, 2007). Atualmente, já existem medicamentos antiangiogênicos disponíveis na clínica, todos eles direcionados contra o VEGF ou suas vias de sinalização. Um exemplo é o bevacizumab (nome comercial de Avastin®), que é um anticorpo monoclonal neutralizante dirigido contra VEGF. Outro exemplo, é o sunitinibe (nome comercial de Sutent), inibidor seletivo do domínio quinase dos receptores de VEGF (ELLIS; HICKLIN, 2008). Entretanto, sabe-se que, apesar de eficiente no tratamento do câncer e algumas retinopatias, nem todos os pacientes e tipos de câncer respondem a esta terapia e muitos desenvolvem resistência ao medicamento. Além disso, por ser um fator central na angiogênese, o tratamento anti-VEGF pode causar alguns efeitos indesejados: perfurações intestinais, alterações nas funções cardíacas, e hipertensão e cardiotoxicidade (BUENO; MOURON; QUINTELA-FANDINO, 2017; CHINTALGATTU et al., 2013). Consequentemente, os tratamentos atuais antiangiogênicos, de forma geral, apenas aumentam a sobrevida dos pacientes em alguns meses.

Nesse sentido, uma melhor compreensão dos fatores e processo associados à angiogênese patológica poderá auxiliar no desenvolvimento de novas terapias antiangiogênicas. Com isso em mente, nosso grupo vem se dedicando à identificação de novos

fatores moleculares que participem, preferencialmente, da angiogênese patológica e que possam ser utilizadas como alvos moleculares no desenvolvimento de novos fármacos antiangiogênicos com maior eficácia para os tratamentos das doenças dependentes de angiogênese.

1.3. A RETINA COMO MODELO DE ESTUDO DA ANGIOGÊNESE PATOLÓGICA

A retina é uma excelente ferramenta para se estudar e elucidar os mecanismos moleculares da neovascularização. Por ser um tecido de fácil acesso, translucido e com uma histologia conhecida, a retina permite a fácil visualização dos vasos sanguíneos que se formam, desde o desenvolvimento, por angiogênese. Em humanos, a vascularização da retina inicia-se no útero aproximadamente na 16ª semana de gestação, completando-se na 40ª semana. Já em camundongos, o desenvolvimento vascular da retina inicia-se logo após o nascimento e perdura durante as duas primeiras semanas de vida dos jovens camundongos.

A retinopatia da prematuridade (ROP) é uma doença que afeta recém-nascidos prematuros, mais especificamente, bebês com menos de 1,5 kg. Por necessitarem de suplementação de oxigênio, esses prematuros são frequentemente submetidos à hiperóxia (altas concentrações de O₂) (KUMAWAT et al., 2021). Como a formação de vasos sanguíneos é controlada pelos níveis de oxigênio e HIF-1 α (*Hypoxia Inducible Factor*), a exposição à alta pressão de oxigênio inibe o processo fisiológico de angiogênese que está ocorrendo nesses jovens bebês. Quando a terapia de administração de oxigênio termina e o prematuro passa a respirar o ar atmosférico, um estado de hipóxia relativa (baixa concentração de O₂) surge, levando à produção de grandes quantidades de VEGF e, conseqüentemente, na formação exacerbada de vasos sanguíneos. Se não for tratada de forma adequada, essa angiogênese patológica pode levar à retinopatia da prematuridade com diversos graus de severidade, inclusive com o descolamento da retina e cegueira permanente (CHEN; SMITH, 2007). Como a formação dos vasos sanguíneos na retina de camundongos (e ratos) ocorre pós-nascimento, é possível reproduzir a ROP nesses animais (PIERCE; FOLEY; SMITH, 1996). Sendo assim, o modelo animal OIR (*oxygen-induced retinopathy*) é amplamente utilizado na análise do papel do VEGF e de outros fatores moleculares envolvidos na neovascularização da retina, assim como para avaliar possíveis terapias para a doença. No modelo animal de OIR, os jovens camundongos com duas semanas de vida (P7-P12), e suas mães, são colocados numa incubadora e mantidos numa atmosfera com 75% de pO₂. Assim como nos bebês prematuros humanos, a exposição a altas concentrações de O₂

provoca vaso-inibição e queda na expressão de VEGF. No dia P12, os animais são, então, transferidos de volta para a atmosfera ambiente (20,8% de pO_2), o que induz um quadro de hipóxia relativa, resultando na expressão elevada e persistente de VEGF. As retinas são analisadas após 5-9 dias (P17-P21), período em que, devido à hipóxia relativa, vasos protuberantes surgem sobre a superfície da retina. Este processo inicia-se entre 6 e 12 horas após retorno aos níveis normais de O_2 e leva à produção exacerbada de vasos sanguíneos (**Fig.2**) (ALON et al., 1995; PIERCE et al., 1995; SMITH et al., 1994).

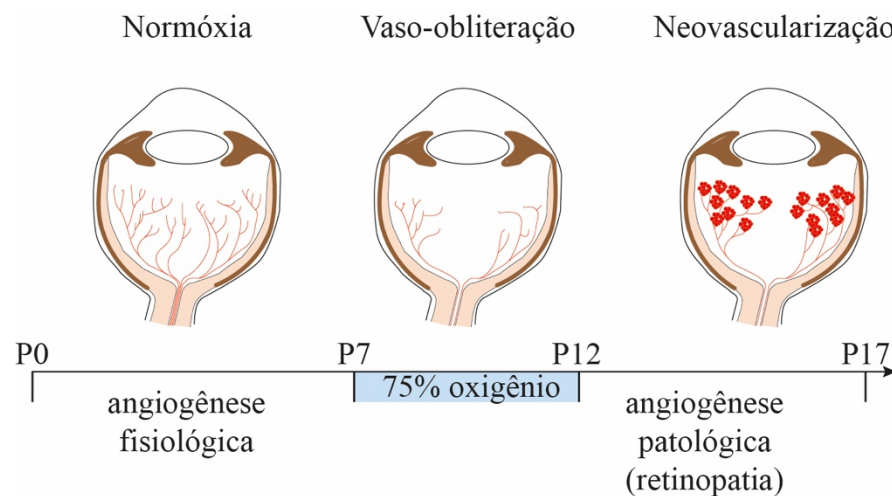


Figura 2. O modelo OIR para o estudo da angiogênese patológica e retinopatia. Representação do modelo da retinopatia induzida por oxigênio em camundongos, indicando as diferentes fases: normóxia, vaso-obliteração e neovascularização (Adaptado de GUARISCHI-SOUSA et al., 2019).

Os níveis de VEGF refletem as variações na pressão de O_2 e, portanto, VEGF tem papel central e duplo neste modelo: hiperóxia diminui a produção de VEGF e induz a regressão de vasos sanguíneos, enquanto que a subsequente diminuição relativa de O_2 resulta na produção elevada de VEGF e formação exacerbada de vasos, levando a um estado de neovascularização patológica.

O modelo OIR é considerado um dos melhores modelos animais para estudar a angiogênese *in vivo*, e tem muitas vantagens em relação a outros modelos de neovascularização. O crescimento dos vasos sanguíneos ocorre dentro de um tecido vivo (retina) e não em uma matriz artificial, tal como a Matrigel ou *scaffolds* de colágeno, usada em outros ensaios de angiogênese. Portanto, a sinalização entre diferentes células é preservada, como em um organismo vivo. Outra vantagem, bastante relevante, é que a indução de angiogênese é modulada por oxigênio e não por compostos químicos ou outros componentes externos adicionados artificialmente. Além disso, a configuração experimental

desse modelo se assemelha muito a uma doença humana, a retinopatia da prematuridade, e até certo ponto, a retinopatia diabética (CHEN; SMITH, 2007).

1.4. O USO DE TÉCNICAS ÔMICAS PARA A IDENTIFICAÇÃO DE NOVOS ALVOS ANGIOGÊNICOS

Os avanços nas tecnologias permitiram a geração de grandes quantidades de dados em várias camadas de um sistema biológico, incluindo dados de sequência de DNA (genômica), níveis de expressão de RNA (transcriptômica), alterações epigenéticas (epigenômica), abundância de proteínas (proteômica), níveis de metabólitos (metabolômica) e lipídeos (lipidômica). Considerando cada uma dessas camadas biológicas separadamente, estudos com diferentes tecnologias e formas de análise de métodos ômicos, têm permitido identificar genes, proteínas e metabólitos associados às mais diversas doenças humanas ou fenótipos de interesse.

Neste trabalho, apresentado na modalidade de tese no formato de compêndio, realizamos análises de transcriptômica, lipidômica e proteômica em condições fisiológicas e patológicas das retinas do modelo animal de retinopatia da prematuridade que foram integrados, ainda que de forma parcial neste momento, para construir um modelo de biologia de sistema da retina fisiológica e patológica (Guarisch-Sousa et al., 2019; Monteiro, 2022 e Inague & Alecrim et al., submetido). Nosso objetivo maior é o de identificar novos fatores moleculares que participam da angiogênese patológica e que possam ser utilizadas como alvos moleculares no desenvolvimento de novos fármacos anti-angiogênicos.

1.4.1. Transcriptoma

A análise da expressão gênica é possível por diferentes métodos. Algumas tecnologias podem ser usadas para identificar a expressão de um único gene, enquanto métodos de alto rendimento são capazes de avaliar a expressão de múltiplos ou mesmo de todo o conjunto de genes de uma só vez, o transcriptoma.

O transcriptoma é o conjunto completo de transcritos (RNAs mensageiros, RNAs ribossômicos, RNAs transportadores e os microRNAs) em uma célula e sua quantidade em um estágio específico de desenvolvimento ou condição fisiológica/patológica. Compreender o transcriptoma é essencial para interpretar os elementos funcionais do genoma e revelar os constituintes moleculares de células e tecidos, e também para entender o desenvolvimento e a doença em estudo (WANG; GERSTEIN; SNYDER, 2009).

No capítulo 1 desta tese, será apresentado um estudo do transcriptoma de mRNAs por RNA-seq da retina dos camundongos com angiogênese em condições fisiológicas e retinopáticas (OIR), realizado pelo nosso grupo e que contou com a minha colaboração desenvolvendo o modelo OIR para obtenção de amostras de RNA e na validação de genes por RT-qPCR. Neste estudo, observamos a presença de mais de 21.000 transcritos na retina, sendo que destes, mais de 3.800 genes são diferencialmente expressos entre as condições fisiológicas e patológicas. Dentre estes, identificamos 153 genes que apresentam a expressão diferencial mais pronunciada entre a angiogênese em condições patológicas e fisiológicas (com valores de \log_2 (fold-change) ≥ 2). A importância destes genes na angiogênese foi confirmada e validada por meio de uma assinatura gênica prognóstica para o câncer de mama, uma doença dependente da angiogênese (GUARISCHI-SOUSA et al., 2019). Esta assinatura utilizou como base estes 153 genes, com expressão significativamente aumentada na angiogênese patológica, demonstrando que o transcriptoma deste modelo animal reproduz aspectos de doenças humanas dependentes da angiogênese, neste caso, o tumor de mama.

A assinatura gênica que identificamos utilizando os 153 genes com expressão diferencial aumentada na angiogênese patológica é um início importante. Porém, observamos que, no total, são mais de 3.800 genes diferencialmente expressos na retina patológica e precisamos de mais informações para entender sua contribuição no processo e potencial terapêutico. É esperado que o fluxo de informações do DNA para o RNA se correlacionasse com a conversão do RNA para a proteína, ou seja, prevê-se que mudanças no transcriptoma levem a alterações correspondentes no proteoma e no metaboloma. No entanto, sabemos que outros elementos influenciam nesta relação, por exemplo, os RNAs regulatórios (VOGEL; MARCOTTE, 2012). Por isso, avaliar a correspondência entre transcritos de mRNA e os correspondentes níveis de proteicos e lipídicos, seria algo muito interessante. Nesse sentido, no capítulo 2 desta tese, abordamos um estudo de análise lipídica e, no capítulo 3, uma análise proteômica de retinas dos camundongos com angiogênese em condições fisiológicas e retinopáticas (OIR).

1.4.2. Lipidoma

A lipidômica estuda os lipídios celulares em larga escala com base em princípios de química analítica e ferramentas tecnológicas, particularmente, espectrometria de massa (YANG; HAN, 2016). O desenvolvimento de técnicas de espectrometria de massa (MS) marcou o início de uma nova era para o estudo de lipídios, abrindo uma série de

oportunidades experimentais. Com a implementação de técnicas de ionização, como a ionização por eletrospray (ESI) e a ionização química à pressão atmosférica (APCI), capazes de acoplar cromatografia líquida (LC) com MS, tornou-se possível separar e analisar até mesmo os lipídios mais hidrofóbicos (ASTARITA; AHMED; PIOMELLI, 2009).

O objetivo final da lipidômica é entender o papel dos lipídios na biologia dos organismos vivos. Ela representa uma ferramenta em rápida evolução em biologia de sistemas, que integra conjuntos multidisciplinares de dados derivados de técnicas de perfil molecular, como genômica, transcriptômica e proteômica. Portanto, há um crescente interesse científico em usar a lipidômica para responder a várias questões biológicas decorrentes de organismos vivos com todo grau de complexidade biológica, como animais, plantas, fungos, bactérias e vírus (ASTARITA; AHMED; PIOMELLI, 2009).

Com o avanço das tecnologias analíticas, a lipidômica se tornou uma ferramenta para a investigação de aplicações clínicas, como diabetes, obesidade, arteriosclerose, doença coronariana, lesões cerebrais, e assim por diante (SHAMIM et al., 2018). Portanto, com esta abordagem foi possível identificar novas moléculas de sinalização, revelar os mecanismos subjacentes responsáveis por condições fisiopatológicas, descobrir potenciais biomarcadores para diagnóstico precoce e prognóstico de doenças, rastrear alvos de drogas e/ou testar a eficácia de drogas, orientar a intervenção nutricional e alcançar resultados personalizados na medicina. Essas realizações são devidas não apenas ao desenvolvimento da técnica, mas também à natureza da lipidômica em si, de ser capaz de analisar de forma cada vez mais abrangente centenas a milhares de espécies lipídicas para estudar o metabolismo lipídico (YANG; HAN, 2016). Um exemplo interessante de estudo envolvendo a análise lipidômica foi com glioblastoma multiforme (GBM), que é o tumor cerebral mais comum e agressivo do sistema nervoso central. Neste estudo, utilizaram uma técnica avançada de MS em tempo real. 13 metabólitos lipídicos foram reconhecidos como biomarcadores desse tecido tumoral, sugerindo que possam ser utilizados em diagnósticos, como também para orientar os cirurgiões a ressecarem com precisão o tecido GBM e manter o tecido cerebral normal em operação (MA et al., 2021).

Compreender os mecanismos moleculares associados a doenças específicas e seus papéis na saúde e na doença é essencial para o desenvolvimento de novos tratamentos terapêuticos para doenças humanas. A retina é um tecido incrivelmente sofisticado que lê a luz que entra no olho e, por sua vez, a converte em informações que podem ser transmitidas

ao cérebro. Para isso, ela depende de um suprimento constante de gordura dietética necessária para sintetizar e produzir uma variedade muito grande de ácidos graxos poliinsaturados de cadeia muito longa (VLC-PUFA, >26 carbonos), muitos deles, encontrados exclusivamente neste tecido. Esses lipídios especializados são necessários para o bom funcionamento da retina, em particular das células fotorreceptoras, protegendo-as do estresse oxidativo causado pela incidência de luz, e também para a modulação da fluidez da membrana, (JOYAL et al., 2016).

A retina também é metabolicamente muito ativa e, ao contrário do que se pensava, requer um suprimento constante de ácidos graxos para a produção de ATP via fosforilação oxidativa (FU et al., 2021). Portanto, não é surpreendente que alterações no metabolismo lipídico tenham sido associadas a muitas das doenças oculares que levam à perda de visão ou cegueira, tanto em crianças quanto em adultos (CAMPOCHIARO, 2015; FLIESLER, 2021; FU et al., 2021; JOYAL et al., 2016). Nesse sentido, para compreendermos melhor o papel dos lipídeos específicos e do metabolismo lipídico na retina, realizamos uma análise lipidômica, apresentada no capítulo 2, em retinas dos camundongos com angiogênese em condições fisiológicas e retinopáticas (OIR). Além de ser, até onde sabemos, o primeiro estudo de lipidoma deste modelo, nosso trabalho também é inovador num outro aspecto, uma vez que combinamos os dados da lipidômica com os do transcriptoma de mRNA para identificar não apenas as espécies lipídicas alteradas pela retinopatia, mas também para mapear as principais vias metabólicas perturbadas pela angiogênese patológica.

Em resumo, neste novo estudo, mostramos que a angiogênese patológica induz intensa remodelação lipídica na retina, favorecendo vias para síntese lipídica neutra, importação/exportação de colesterol e formação de gotículas lipídicas. Mapeamos e quantificamos um total de 300 espécies lipídicas em condições fisiológicas (P) e patológicas (R). Desta forma, combinando cuidadosamente o perfil lipídico com as alterações no transcriptoma do mRNA, pudemos identificar uma assinatura lipídica associada à retinopatia induzida por oxigênio.

Essa assinatura lipídica indica que, desde seus estágios iniciais, a angiogênese patológica é responsável por alterações que culminam na intensa formação de gotículas lipídicas, possivelmente, como fonte energética das células fotorreceptoras. Também induz mudanças profundas nas vias envolvidas na síntese de ácidos graxos poliinsaturados de cadeia muito longa, vitais para a homeostase da retina. Essas alterações levam à produção de

quantidades significativas de ácido de mead (*mead acid*), um ácido graxo ômega-9, marcador de deficiência de ácidos graxos essenciais. Estes são novos resultados, empolgantes, que nos levam a sugerir que o *mead acid* possa ser um novo marcador para a gravidade da retinopatia e talvez de outras doenças oculares.

1.4.3. Proteoma

Finalmente, no capítulo 3, vamos abordar o estudo, ainda em andamento, do proteoma da retina. Estudos de proteômica se referem à identificação e quantificação das proteínas presentes num sistema biológico (células, tecido, órgão, fluido biológico ou organismo), em um momento específico, sendo o proteoma o conjunto de proteínas codificadas pelo genoma de um organismo, incluindo processos pós-transcricionais e pós-traducionais. O proteoma de um organismo é dinâmico, pois se altera nas condições ambientais e em momentos distintos, como as fases de diferenciação celular, refletindo o funcionamento atual do organismo (AHRENS et al., 2010).

As proteínas atuam no controle e catálise dos vários processos biológicos e são responsáveis pelo fenótipo celular, desta forma, a análise proteômica possibilita estudar simultaneamente vários aspectos, como a identificação de proteínas contidas numa unidade biológica, interações proteína-proteína e entre outras moléculas, vias de interação bem como quantificação, identificação de subgrupos de proteínas, análise funcional, diferenças de expressão proteica em populações celulares distintas, desenvolvimento de respostas ao ambiente e modificações pós-traducionais (LAM; JIMENEZ; BOVEN, 2014).

O avanço de outras áreas, como a genômica e a bioinformática, permitiu a construção *in silico* de bancos de dados de sequências derivadas dos diversos genomas dos mais diferentes organismos. Por outro lado, métodos cada vez mais sofisticados de ionização, permitiram o desenvolvimento de novas tecnologias de proteômica baseada em espectrometria de massas (MS – *mass spectrometry*). A ionização por *eletrospray* permite a análise de biomoléculas com elevado peso molecular, como as proteínas, através da produção de íons carregados na fase gasosa (CASTLEBERRY; RODICIO; LIMBACH, 2008).

A espectrometria de massa realiza a análise de identificação dos analitos (no caso da proteômica, fragmentos na forma de peptídeos derivados das diferentes proteínas na amostra) e é baseada na ionização do composto e avaliação massa carga (m/z) dos íons. Ela fornece informações estruturais sobre a proteína, como a massa dos peptídeos e sequências de

aminoácidos, possibilitando a identificação de proteínas utilizando a comparação em bancos de dados, além de determinar o tipo e local das modificações proteicas (GRAVES et al., 2002).

O método baseado em espectrometria de massas denominado Proteômica *Shotgun* é o mais utilizado quando não há conhecimento prévio da amostra e se deseja identificar um grande número de proteínas. Além disso, esse método permite a quantificação relativa das proteínas por meio da mensuração da área dos picos cromatográficos de cada peptídeo que são comparados entre as amostras, mesmo quando livres de marcação, chamada de quantificação *label-free* (BENSIMON; HECK; AEBERSOLD, 2012; NEILSON et al., 2011).

Utilizando o método de *Shotgun*, realizamos uma análise proteômica com retinas fisiológicas e patológicas do modelo animal OIR e identificamos um total de 2.806 proteínas. Novamente, a análise proteômica mostrou uma grande correlação com o estudo do transcriptoma, apresentando perfis de transcrição e tradução simultâneos. Porém, o que merece destaque é o fato de que as proteínas mais abundantes da análise proteômica na retinopatia estão relacionadas com o metabolismo e vias de lipoproteínas, colesterol, quilomicrons e triacilglicerol, ou seja, esses dados corroboram com o nosso estudo do lipidoma, sugerindo a participação importante de vias de lipídios neutros na formação de gotículas lipídicas e com a ocorrência de transporte reverso de colesterol em retinas patológicas.

Em resumo, observamos uma convergência interessante nesses três estudos e acreditamos que os dados dessas três técnicas, detalhados a seguir, permitem uma melhor integração das vias celulares e metabólicas da retina, levando a uma melhor compreensão das bases moleculares da angiogênese fisiológica e patológica. Esses conhecimentos poderão contribuir para o desenvolvimento de novas alternativas terapêuticas para as diversas doenças dependentes da angiogênese, em particular, doenças oculares.

2. OBJETIVOS

Pelo fato da retina ser uma excelente ferramenta para elucidar os componentes que participam da neovascularização, tanto em condições fisiológicas como patológicas, este trabalho teve por objetivo:

2.1. Construir um modelo de biologia de sistemas da retina em condições fisiológica e patológica, em busca de um melhor entendimento dos mecanismos moleculares que participam da angiogênese patológica e da retinopatia.

Para atingirmos o nosso objetivo geral, os objetivos específicos foram:

2.1.1. Caracterizar o perfil lipídico da angiogênese na retina. Realizar uma análise lipidômica global ao longo do tempo de retinas retinopáticas e fisiológicas.

2.1.2. Caracterizar o proteoma da retina angiogênica. Investigar o processo angiogênico utilizando métodos de proteoma por espectrometria de massas da retina ao longo de seu desenvolvimento no modelo animal de retinopatia da prematuridade. Realizar um estudo de proteômica comparativa, a fim de observar as flutuações de produção das diferentes proteínas da retina em condições normais e, principalmente, retinopáticas.

2.1.3. Integrar os dados de lipidômica e proteômica com os dados de transcritômica de mRNA. Identificar as vias moleculares, proteínas e metabólitos lipídicos que foram afetados pela angiogênese patológica. Esses estudos poderão contribuir para identificarmos novos alvos moleculares para o desenvolvimento de medicamentos antiangiogênicos.

3. CAPÍTULO 1

Capítulo descrito na forma de artigo com Digital Object Identifier (DOI): 10.1371/journal.pgen.1008482

A transcriptome-based signature of pathological angiogenesis predicts breast cancer patient survival

Abstract

The specific genes and molecules that drive physiological angiogenesis differ from those involved in pathological angiogenesis, suggesting distinct mechanisms for these seemingly related processes. Unveiling genes and pathways preferentially associated with pathologic angiogenesis is key to understanding its mechanisms, thereby facilitating development of novel approaches to managing angiogenesis-dependent diseases. To better understand these different processes, we elucidated the transcriptome of the mouse retina in the well accepted oxygen-induced retinopathy (OIR) model of pathological angiogenesis. We identified 153 genes changed between normal and OIR retinas, which represent a molecular signature relevant to other angiogenesis-dependent processes such as cancer. These genes robustly predict the survival of breast cancer patients, which was validated in an independent 1,000-patient test cohort (40% difference in 15-year survival; $p = 2.56 \times 10^{-21}$). These results suggest that the OIR model reveals key genes involved in pathological angiogenesis, and these may find important applications in stratifying tumors for treatment intensification or for angiogenesis-targeted therapies.

RESEARCH ARTICLE

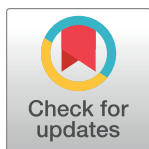
A transcriptome-based signature of pathological angiogenesis predicts breast cancer patient survival

Rodrigo Guarischi-Sousa^{1,2}, Jhonatas S. Monteiro¹, Lilian C. Alecrim¹, Jussara S. Michaloski¹, Laura B. Cardeal¹, Elisa N. Ferreira³, Dirce M. Carraro³, Diana N. Nunes³, Emmanuel Dias-Neto^{3,4}, Jüri Reimand^{2,5}, Paul C. Boutros⁶*, João C. Setubal¹*, Ricardo J. Giordano¹*

1 Biochemistry Department, Institute of Chemistry, University of São Paulo, São Paulo, Brazil, **2** Computational Biology Program, Ontario Institute for Cancer Research, Toronto, Ontario, Canada, **3** International Research Center (CIPE) A.C. Camargo Cancer Center, São Paulo, SP, Brazil, **4** Laboratory of Neurosciences (LIM27), Institute & Department of Psychiatry, University of São Paulo, São Paulo, Brazil, **5** Department of Medical Biophysics, University of Toronto, Toronto, Ontario, Canada, **6** Department of Human Genetics, University of California Los Angeles (UCLA), Los Angeles, CA, United States of America

* These authors contributed equally to this work.

* PBoutros@mednet.ucla.edu (PCB); setubal@iq.usp.br (JCS); giordano@iq.usp.br (RJG)



OPEN ACCESS

Citation: Guarischi-Sousa R, Monteiro JS, Alecrim LC, Michaloski JS, Cardeal LB, Ferreira EN, et al. (2019) A transcriptome-based signature of pathological angiogenesis predicts breast cancer patient survival. *PLoS Genet* 15(12): e1008482. <https://doi.org/10.1371/journal.pgen.1008482>

Editor: Kornelia Polyak, Dana-Farber Cancer Institute/Harvard Medical School, UNITED STATES

Received: February 28, 2019

Accepted: October 15, 2019

Published: December 17, 2019

Copyright: © 2019 Guarischi-Sousa et al. This is an open access article distributed under the terms of the [Creative Commons Attribution License](https://creativecommons.org/licenses/by/4.0/), which permits unrestricted use, distribution, and reproduction in any medium, provided the original author and source are credited.

Data Availability Statement: Sequencing metadata is available in the Sequence Read Archive (SRA) under accession code BioProject PRJNA483866. RNA-seq data is available under accession SRP155931. Rdata object is available as [S1 File](#).

Funding: This work was supported by research grants from: São Paulo Research Foundation (FAPESP; www.fapesp.br) (grant 2008/54.806-8 and 2016/22.645-1 to R.J.G., and fellowships 2012/15.197-1 and 2014/21.360-8 to R.G.S.), the National Council for Scientific and Technological

Abstract

The specific genes and molecules that drive physiological angiogenesis differ from those involved in pathological angiogenesis, suggesting distinct mechanisms for these seemingly related processes. Unveiling genes and pathways preferentially associated with pathologic angiogenesis is key to understanding its mechanisms, thereby facilitating development of novel approaches to managing angiogenesis-dependent diseases. To better understand these different processes, we elucidated the transcriptome of the mouse retina in the well-accepted oxygen-induced retinopathy (OIR) model of pathological angiogenesis. We identified 153 genes changed between normal and OIR retinas, which represent a molecular signature relevant to other angiogenesis-dependent processes such as cancer. These genes robustly predict the survival of breast cancer patients, which was validated in an independent 1,000-patient test cohort (40% difference in 15-year survival; $p = 2.56 \times 10^{-21}$). These results suggest that the OIR model reveals key genes involved in pathological angiogenesis, and these may find important applications in stratifying tumors for treatment intensification or for angiogenesis-targeted therapies.

Author summary

Angiogenesis is the formation of new blood vessels from pre-existing ones and it is the process for revascularization that predominates in adult life. Although angiogenesis is essential in physiological processes, such as wound healing, it also participates in pathological conditions, collectively known as angiogenesis-dependent diseases. Cancer and retinopathies are examples of such diseases. In cancer, angiogenesis is considered one of

Development (CNPq; www.cnpq.br) (grant number 560.860/2010) (to R.J.G.) and research fellowships (to J.C.S. and R.J.G.). This study was also financed in part by the Coordenação de Aperfeiçoamento de Pessoal de Nível Superior Brasil (CAPES; www.capes.gov.br), Finance Code 001. The funders had no role in study design, data collection and analysis, decision to publish, or preparation of the manuscript.

Competing interests: The authors have declared that no competing interests exist.

its hallmarks as tumors depend on a constant supply of oxygen and nutrients to grow. The more angiogenic the tumor, the more aggressive it is for the patient. In the present work, we used a well-suited animal model of retinopathy, an angiogenesis-dependent disease, to study the molecular signature for angiogenesis. We analyzed differences in gene expression from retinas developing under physiological and in retinopathic conditions to identify a molecular gene signature for angiogenesis. Because of the association between these two diseases, we tested our gene signature using data from human cancer. We showed that our gene signature has a robust prognostic value to predict breast cancer patient survival. Our results may lead to a better understanding of molecular mechanisms of pathological angiogenesis and its contribution to breast cancer.

Introduction

It has been almost half a century that the field of angiogenesis ascended based on the thoughtful idea that tumor growth is dependent on neovascularization [1–3]. This exciting hypothesis evolved and matured over the decades, and today patients from at least two important groups of diseases benefit from anti-angiogenesis therapy: cancer and ocular diseases [2,4]. Most of the drugs in the clinic are directed at the vascular endothelial growth factors (VEGF) or their receptors and pathways, all essential players in blood vessel formation [4,5,6].

Although successful, anti-VEGF therapy still has important deficiencies. Patients from both groups of diseases, ocular and oncologic, may have incomplete response to anti-VEGF therapy or eventually become refractory to treatment [5–7]. Not all tumors respond to anti-VEGF therapy and response is far from homogenous, even for patients with the same type of tumor. While, in general, patients with renal and metastatic colon cancer respond well to anti-VEGF therapy, the approval of bevacizumab for breast cancer treatment was suspended in the US after two studies showed contradictory results (reviewed by ref. [8]). Therefore, there is a pressing need for reliable methods of assessing patient response to anti-angiogenesis therapy.

We propose that mRNA abundance gene signatures may have an important role in separating patients that would benefit from anti-VEGF therapy from those that do not. The challenge for developing these signatures lies in identifying sets of genes that are representative of and tightly associated with specific diseases. This can be a challenge when using data obtained from human tumors for which angiogenesis is a hallmark [9] or, for that matter, any cohort of human samples given the genetic variability amongst patients. Cancer cells are notoriously heterogeneous, and tumors themselves are surrounded and affected by a dynamic microenvironment comprised of a diversity of parenchymal, vascular, immune, and even prokaryotic cells [10–12].

To minimize these confounding factors and to identify a core of genes associated with angiogenesis, we relied on a mouse model that has been extensively used to study pathological angiogenesis [13–18]. The oxygen-induced retinopathy (OIR) mouse model works by varying the levels of oxygen in the developing retina in order to modulate VEGF expression [19,20]. The result is a state of pathological angiogenesis that is driven by hypoxia and VEGF, as in human tumors. The OIR model also reproduces many aspects of another important human disease that affects premature babies: the retinopathy of prematurity (ROP) [20,21]. Thus, by comparing transcripts of mouse retinas developing under physiological and pathological conditions (OIR), we were able to identify a set of genes that may capture the gene expression basis of hypoxia and VEGF-driven pathological angiogenesis. These genes were next validated by building an angiogenesis signature with prognostic value in human breast cancer.

Collectively, our data validate these differentially expressed genes as representative of pathological angiogenesis not only in the retina but also in an important human disease, breast cancer, suggesting that other signatures and therapeutic gateways may be developed based on this gene set.

Results

OIR sequencing

The ideal animal model for studying angiogenesis should have the following features. First, it should be isogenic, to reduce genetic variation and increase reproducibility. Second, it should not require transient genetic manipulation or administration of exogenous materials (e.g. drugs, scaffolds or viral vectors). Third, it should mimic physiologic processes like retinal neovascularization, recapitulating aspects of human diseases [19]. The model we have used (OIR) has all these benefits, thus avoiding confounding factors present in other strategies. The OIR model consists of placing seven-day-old mice (postnatal day 7, P7) with their nursing mothers in 75% oxygen for five days (Fig 1A). The hyperoxic environment halts the physiological vascular development in the retina and its effect is particularly visible in the central area of the retina, where vessel regression can be clearly observed [22]. Thus, when mice return to room air (20.8% oxygen) on P12, the now under-vascularized retina experiences a sudden hypoxic condition leading to VEGFA overexpression compared to physiological retinas, resulting in abnormal vascular growth and pathological angiogenesis, which peaks at P17 [20].

To confirm that in our experimental settings mice had indeed developed OIR, we analyzed sample retinas and observed the characteristic phenotype: vaso-oblivation (VO) in central retina, formation of vascular tufts, and vitreous humour vascular invasion (Fig 1B). Retinas under physiological development did not show any sign of retinopathy. Having confirmed the development of the OIR phenotype, we proceeded to determine the transcriptome of retinas at different time points of development in physiological and pathological conditions. Two OIR experiments were performed and retinas from 4 mice ($N = 8$ retinas) were analyzed. In physiological conditions, we collected samples at P12, P15 and P17 (physiological angiogenesis); from OIR mice we collected samples at P12 (immediately after leaving the chamber with 75% oxygen) along with retinas 12 hours after exposure to 75% oxygen (P12.5); then at P15 (mid-ROP) and P17 (ROP peak). To distinguish physiological and pathological samples, the OIR retina samples will be referred to as R12, R12.5, R15 and R17. High quality total RNA was obtained from all retinas, treated with DNase to remove genomic DNA contamination, and utilized for RNA-seq library construction, preserving RNA strand information. To enrich for exonic reads, we rebuilt all libraries using poly-A+ RNA and performed very high-depth sequencing (average: 147 million reads per sample). Approximately 90% of the reads confidently mapped to the mouse genome and 86% to exons (S1 Table). Our reads mapped to 21,390 annotated genes (out of 47,069 genes in the primary assembly), representing 45% of all mouse genes and reflecting the intense transcriptional activity of the retina. To confirm the quality of our RNA-seq data, we performed real time PCR for 42 candidate genes selected based on their role in angiogenesis or large effect-sizes. The RT-PCR and RNA-seq data were in agreement in all samples and stages of retinal development or OIR (Fig 1C and S1A Fig), with a strong linear relation between the abundance values obtained with each of the two technologies ($r_2 = 0.93$; $p_R = 2.31 \times 10^{-104}$; S1B Fig).

Transcriptome landscape of the developing retina

We observed that physiological and pathological retinas share over 3,800 differentially expressed genes (1.5-fold, \log_2), which were associated with multiple cellular functions and

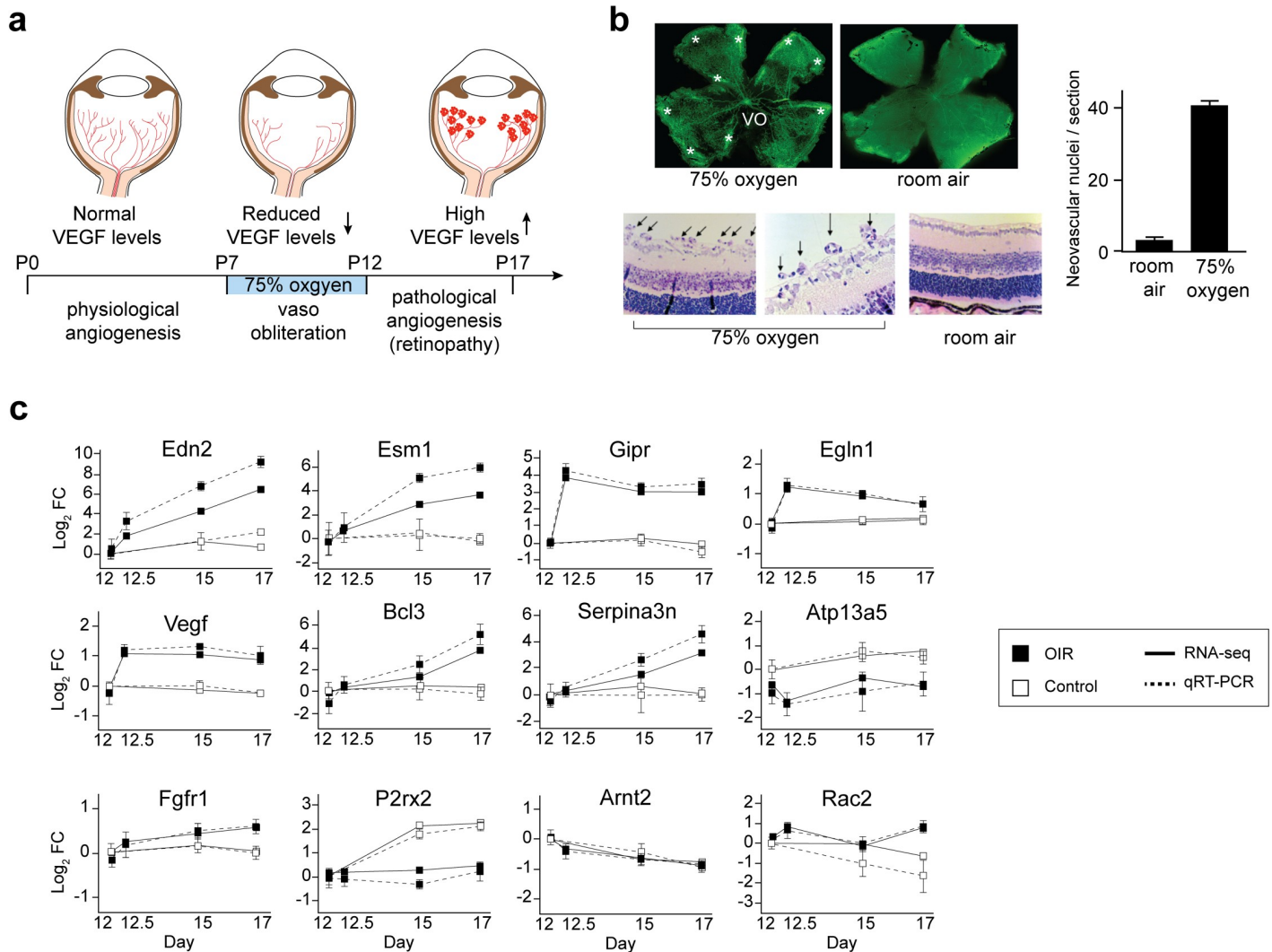


Fig 1. The OIR model and the transcriptome of the angiogenic retina. (a) Cartoon representation of the OIR model. Neonatal mice with their nursing mothers are exposed to 75% oxygen from day P7 to P12, which reduces VEGF production in the retina and induces vaso-regression and central area vaso-obliteration (VO). Upon return to room air, the now hypoxic retina increases VEGF levels and a pathological angiogenesis states ensues. (b) Confirmation of the pathological angiogenesis condition in OIR-mice used for the RNA-seq study, with central area VO, vascular tufts (*) and the presence of intravitreal vessels (arrows). (c) Expression profile of selected genes quantified by RNA-Seq and RT-PCR methods. Bars represent standard error of the mean from independent biological samples (N = 8). Fold-changes were calculated relative to P12 samples.

<https://doi.org/10.1371/journal.pgen.1008482.g001>

diseases, such as cellular movement, morphology and survival (apoptosis), cancer, cardiovascular development and organismal injury or abnormalities (Fig 2A). This is expected, and most of these pathways represent cellular processes ongoing in normal and pathological retinal development. It is also evidence of how challenging it is to analyze transcriptome data of complex tissues. In particular, the retina is a highly transcriptionally active tissue comprised of as many as 60 different types of neural cells, plus additional parenchymal, immune and vascular cells [23]. Nevertheless, it is reassuring to see that the top canonical pathway we identified (hepatic fibrosis/hepatic stellate cell activation) (Fig 2B) is driven by molecular factors that are known to play an important role in angiogenesis: VEGF, fibroblast growth factor (FGF), platelet derived growth factor (PDGF-BB), transforming growth factor (TGF- α and - β), insulin growth factor (IGF-1), and endothelin signaling pathways (Fig 2C). The next ranked canonical

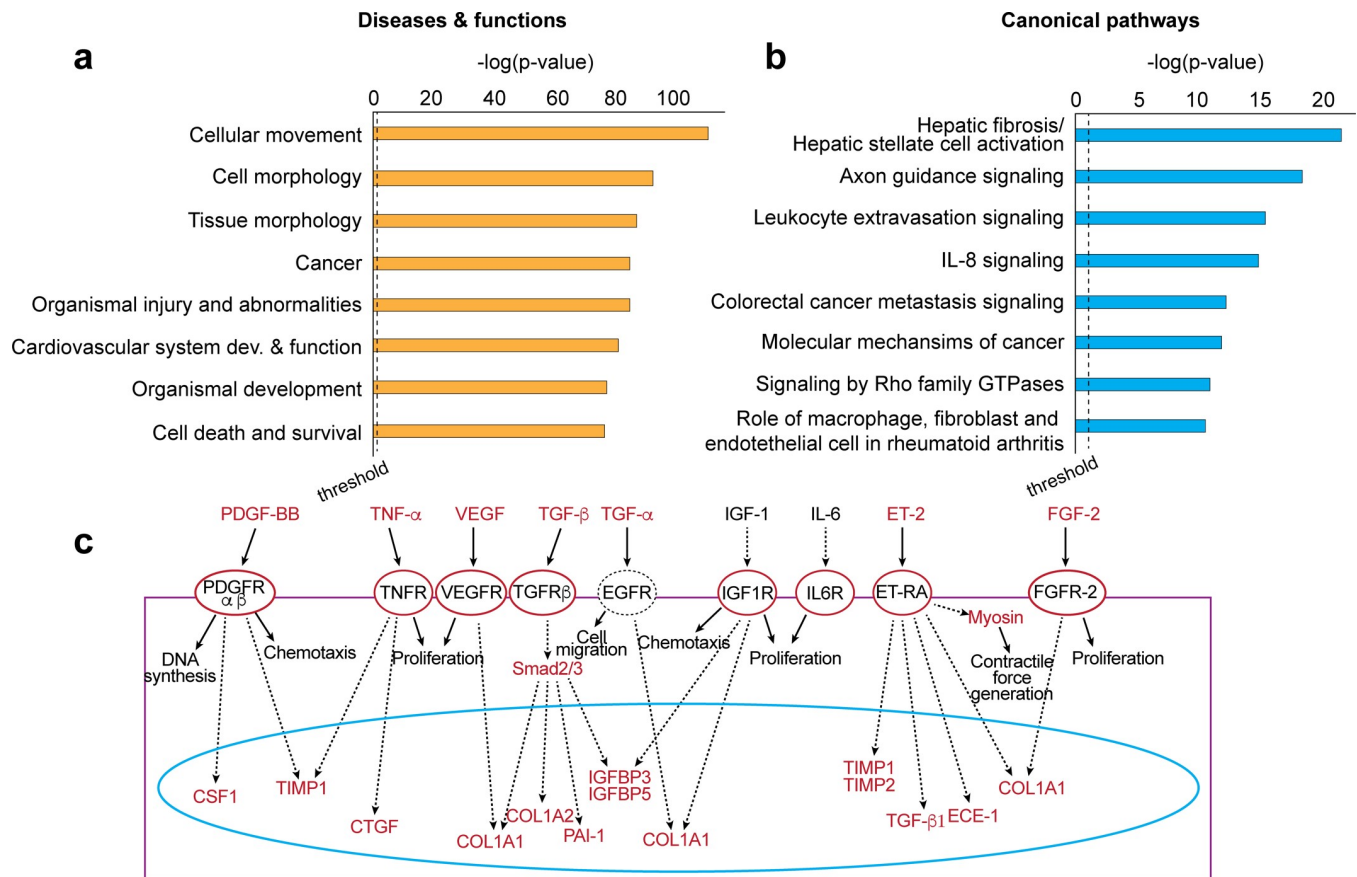


Fig 2. The retina transcriptome landscape. (a) Diseases, cellular functions and (b) canonical pathways associated with in OIR retinas, based on >1,800 differentially expressed genes (fold-change ≥ 1.5). (c) Most of the canonical pathways found in hepatic fibrosis/hepatic stellate cell activation are associated with angiogenesis.

<https://doi.org/10.1371/journal.pgen.1008482.g002>

pathway, axon guidance signaling, is also noteworthy. The developing retina, an extension of the central nervous system, is actively remodeling neurons and glial cells. However, VEGF is also a neurogenic factor and many of the molecules and cellular pathways associated with neuronal axon migration are also involved in angiogenesis [24,25]. In summary, the RNA-seq data represent an intricate mix of transcriptomes from all types of retinal cells, resulting in a pool of expressed genes from diverse pathways.

Genes associated with pathological angiogenesis

Given the complexity of our transcriptome, we chose a special approach to identify genes associated with pathological angiogenesis. First, we performed a principal component analysis (PCA) using gene expression (500 most variable genes), which revealed the expected segregation pattern for our model, with principal component (PC) 1 reflecting the developmental stage (in days) and PC2 representing the condition (OIR or normal retinal development) (Fig 3A). Next, to limit the number of genes, we decided to focus on differentially expressed genes between controls and the pathological condition (OIR) that had significant ($p < 0.05$) and substantial change in expression by adopting the threshold of 2-fold (\log_2) change in at least one comparison. These genes were then subjected to the null hypothesis test and only those with FDR (false discovery rate) < 0.05 were selected. The result was a list of 153 genes, most of

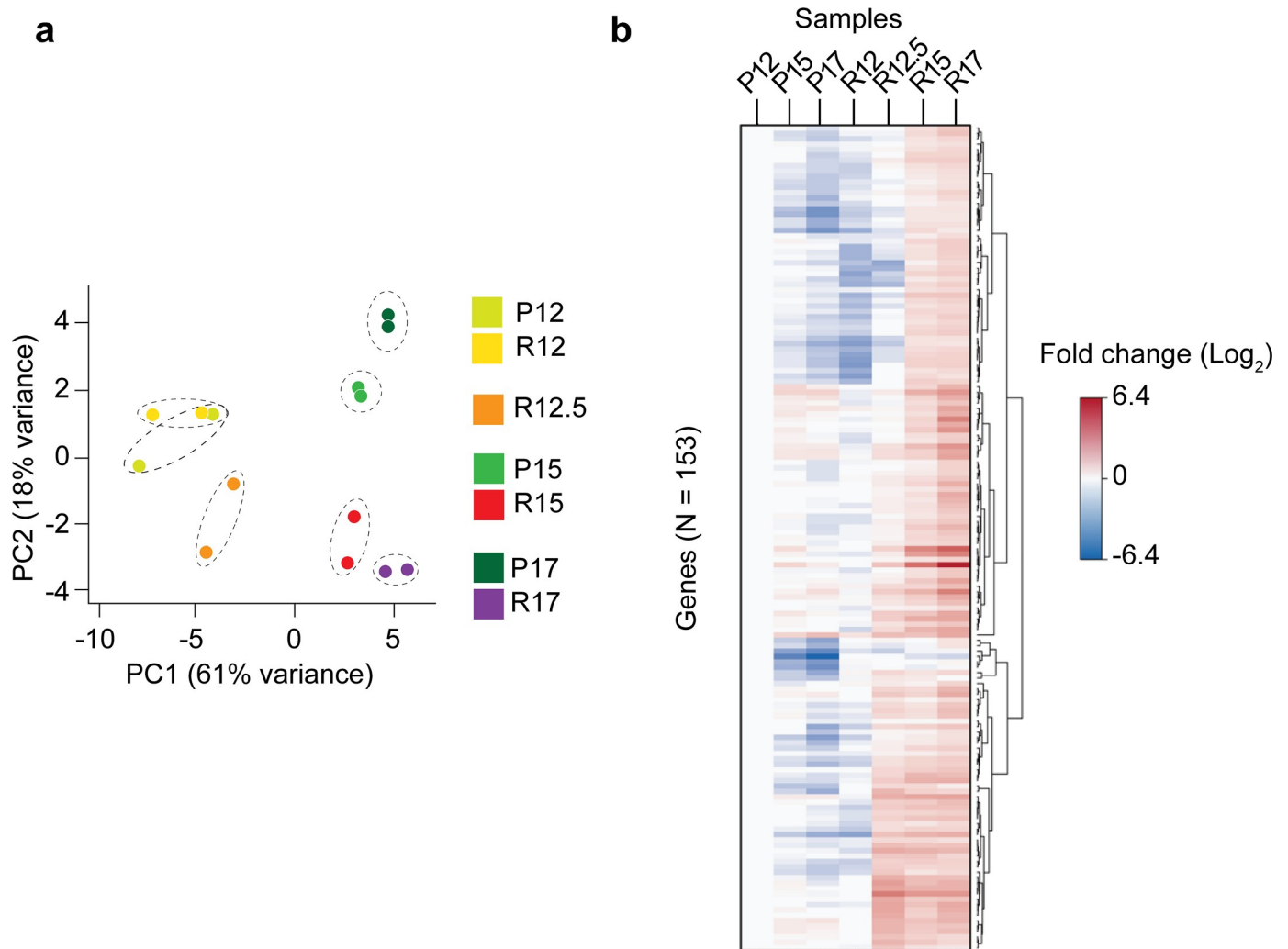


Fig 3. Angiogenic associated genes. (a) Principal component analysis using 500 genes with the highest variance in expression. PC1 is stage dependent, and PC2 is condition dependent (OIR or normal retina development); these components explain 61% and 18% of variance, respectively; filtered by genes with > 500 reads on all samples. (b) Heatmap and dendrogram illustrating the expression profile of the 153 differentially expressed genes across all retina samples (fold-change ≥ 2).

<https://doi.org/10.1371/journal.pgen.1008482.g003>

them up-regulated in pathological angiogenesis (R15 and R17) (Fig 3B; S2 Table). We next asked whether these genes would be representative of angiogenesis in other models and diseases.

Angiogenic and hypoxic gene signatures

To address this question, we hypothesized that our set of differentially expressed genes might comprise a signature of pathological angiogenesis. Several research groups, including ours, have long attempted to identify gene signatures with prognostic power, with mixed results [26,27]. First, we determined how the 153 genes that we identified in our transcriptome would compare with genes in these previously described signatures.

We performed a comprehensive evaluation of existing angiogenic signatures and found nine angiogenesis signatures in the literature (Table 1) [28–36] (S3 Table). Considering the underlying relationship between angiogenesis and hypoxia, we extended our analysis to

Table 1. Angiogenesis gene signatures.

Contributors	Reference	Cancer Type	Platform	Genes
Hu <i>et al.</i>	36	NSCLC	Microarray	62
Mendiola <i>et al.</i>	35	AOC	qRT-PCR	34
Bentink <i>et al.</i>	34	SOV	Illumina DASL, BeadArray	100
Masiero <i>et al.</i>	33	HNSCC, BC, CCRCC	Meta signature	43
Khong <i>et al.</i>	32	CC	RT Profiler, PCR array	9
Pinato <i>et al.</i>	31	GNT	Tissue microarray	2
Sanmartin <i>et al.</i>	30	NSCLC	qRT-PCR	3
Langlois <i>et al.</i>	29	Glioma, CC	Microarray	110
Stefansson <i>et al.</i>	28	AEC	Microarray	32

AEC = Aggressive Endometrial Cancer; AOC = Advanced Ovarian Carcinoma; BC = Breast Cancer; CC = Colorectal Cancer; CCRCC = Clear Cell Renal Cell Carcinoma; GNT = Gastrointestinal Neuroendocrine Tumours; HNSCC = Head and Neck Squamous Cell Carcinoma; NSCLC = Non-small-cell lung cancer; SOV = Serous Ovarian Cancer.

<https://doi.org/10.1371/journal.pgen.1008482.t001>

include eight hypoxia signatures [27,37–43] (S3 Table). Across the 1,457 genes comprising these 17 signatures, very few genes were present in multiple signatures (Fig 4A) and while some individual hypoxia and angiogenesis signatures share a small number of genes [27,29,30,34–36,38,40–42], others do not [28,33] (S4 Table). Overall, the signatures we investigated showed little correlation with each other, indicating a surprising disagreement (Fig 4B).

Amongst the 153 genes identified as differentially expressed in pathological angiogenesis, 143 have a homologous gene in humans, based on homology information retrieved from BioMart, resulting in 149 human homolog genes (3 mouse genes had multiple human homologs). Of those, 20 were present in hypoxia signatures and 36 in angiogenesis signatures (Fig 4C; S4 Table). Thus, the great majority (111 genes, 82%) of the 149 differentially expressed genes with human homologs that we identified in the retina transcriptome are not present in any of the previously described gene signatures.

Identification of a new angiogenic gene signature with prognostic power

To assess whether we had identified a *bona fide* signature of pathological angiogenesis, we used a machine-learning approach and the Molecular Taxonomy of Breast Cancer International Consortium (METABRIC) dataset [44] to evaluate the disease relevance of our angiogenic signature in these patients (Fig 5). METABRIC is a large collection with almost 2,000 tumor samples, including mRNA abundance profile and long-term clinical outcomes. All patients received similar chemotherapy regimen and none were treated with anti-HER2 drugs, which makes this dataset an excellent resource to use in the development of an angiogenesis gene signature (Table 2). The METABRIC dataset was initially assembled in two stages: an initial set of tumors used as the discovery group ($N = 996$) and a further set of tumors ($N = 992$) that was added later to the database, and used as validation cohort [44]. There is no patient overlap between the two groups.

Each of the angiogenesis signature genes also present in the METABRIC dataset was tested for its association with overall survival using Cox proportional hazards modeling. Feature-selection focused on genes with a significant association ($p < 0.05$). This resulted in 56 features (54 genes plus patient age and tumor stage), which were used to build a survival random forest model for patient classification (S5 Table). The algorithm starts by analyzing individual genes and their associations with the patient’s prognostic data using the discovery cohort ($N = 996$ patients). For this, features are ranked according to their p -values in the METABRIC dataset

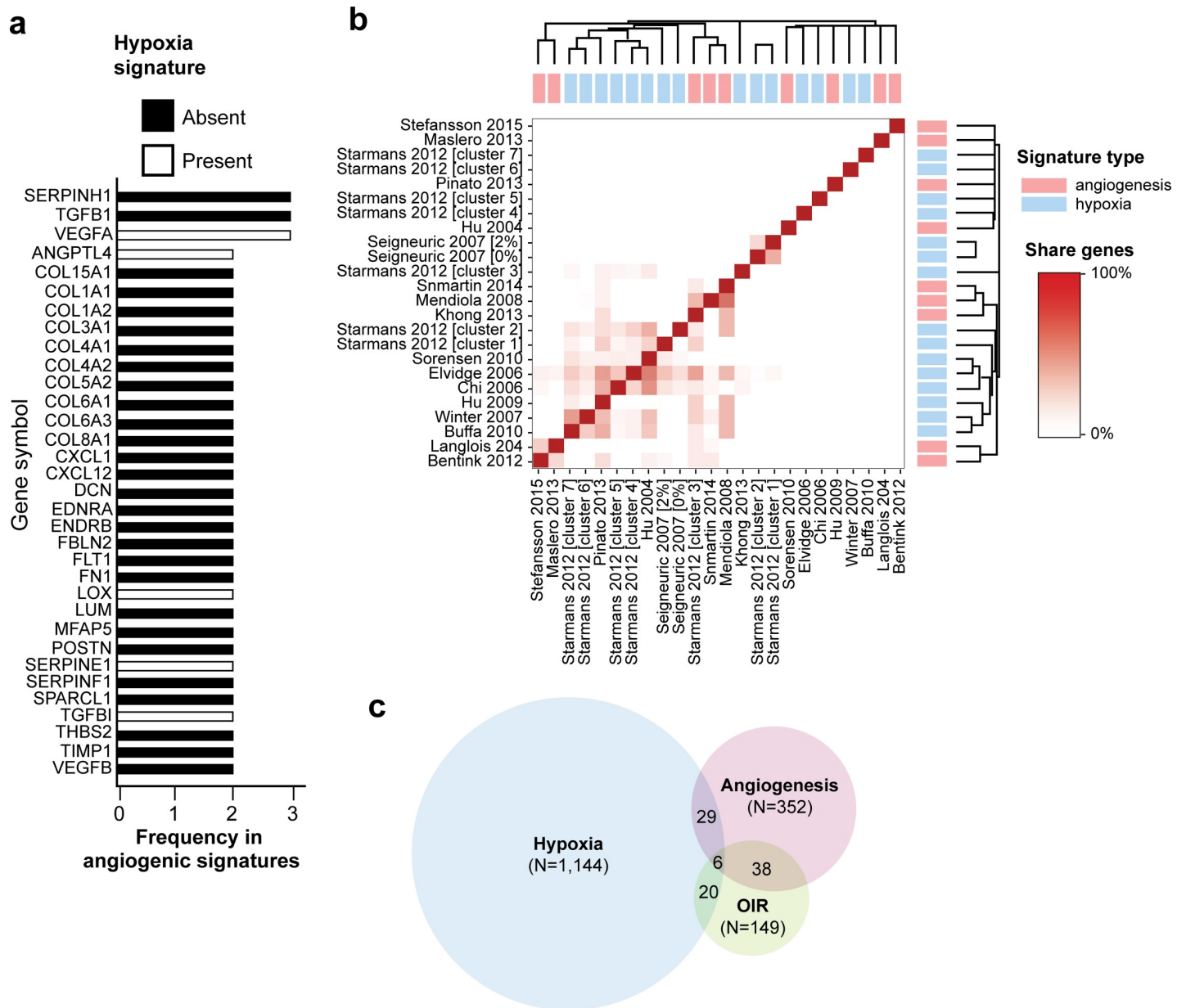


Fig 4. Meta-analysis of current available angiogenesis and hypoxia signatures. (a) List of genes present in at least two angiogenesis signatures sorted by their frequency and presence in hypoxia signatures. (b) Pearson correlation between each pair of signatures. Diana clustering highlight the most related signatures. (c) Venn-diagram showing the overlap between hypoxia, angiogenesis signatures and the 149 differentially expressed genes with human homologs identified in the retina transcriptome (fold-change ≥ 2).

<https://doi.org/10.1371/journal.pgen.1008482.g004>

and given a discretionary prediction value. The machine learning algorithm then incrementally feeds new attributes to generate all models that could best classify and group patients according to survival time, which are then tested against the validation cohort ($N = 992$ patients). The final gene signature is the model with the minimum error. Our final model contains 15 features: 11 differentially expressed genes (*VEGFA* and *PIEZO2* are used twice, as continuous and binary values) plus age and stage (Fig 6A). This model was next used to classify patients in the test cohort into groups according to their predicted time of survival: low-risk

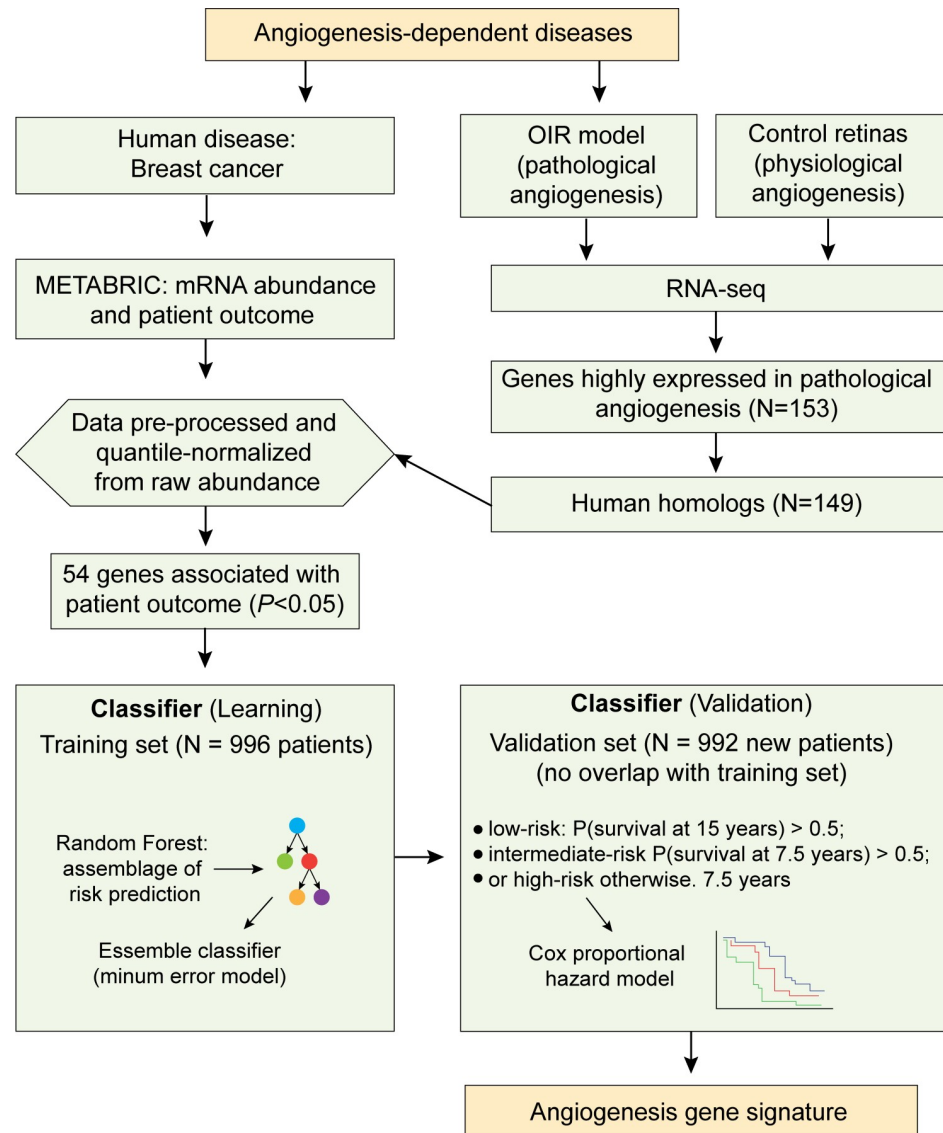


Fig 5. Diagram outlining the input and workflow of the machine-learning algorithm. Two angiogenesis-dependent diseases were selected for this study: breast cancer (pink boxes) and OIR (green boxes). For the OIR model, data was generated in the study; by comparing physiological and pathological retinas (OIR), 153 genes differentially expressed were identified. These genes have 149 human homologs that were then compared with publicly available data (METABRIC) for breast cancer patients. For that, mRNA abundance data were pre-processed and quantile-normalized for comparison with the RNA-seq data. The METABRIC dataset was divided into two cohorts (learning and validation). The machine-learning algorithm (blue boxes) uses the learning cohort to assemble the risk prediction models, which are then tested on the validation cohort. The angiogenesis gene signature is the model with the minimum error.

<https://doi.org/10.1371/journal.pgen.1008482.g005>

(more than 15 years), intermediate-risk (between 15 and 7.5 years) and high-risk (less than 7.5 years). A surprising predictive value was observed ($p = 2.56 \times 10^{-21}$; log-rank test) (Fig 6B).

Model fitness and contribution of OIR genes

To assess the performance of our model, we did two additional analyses. First, we evaluated the variation of the calculated error through the decision process to build our model (number

Table 2. Clinical characteristics of METABRIC cohort on Training and Validation sets.

	Training	Validation
Number of patients	996	992
Age at diagnosis (years)*	61.30 (51.13, 70.31)	62.66 (51.91, 70.91)
Overall survival (years)*	7.06 (3.94, 11.96)	7.32 (4.35, 11.90)
Tumour size*	23 (17, 30)	23 (17, 30)
Lymph nodes positive		
0	514	528
1	174	163
2	95	76
> = 3	213	219
NA	0	6
Stage		
0	1	12
1	315	187
2	533	299
3	71	46
4	9	1
NA	67	447
ER status		
Pos	798	719
Neg	198	273
PAM50 subtype		
Basal	118	212
HER2	86	152
Luminal A	466	255
Luminal B	268	223
Normal	58	144
NA	0	6

<https://doi.org/10.1371/journal.pgen.1008482.t002>

of trees run by the algorithm). We observed that after 500 trees the algorithm had already reached a plateau with error rate around 0.315, which corresponds to a performance of 68.5% (Fig 7A). We also evaluated the performance of our method relative to the null distribution of prognostic signatures [26,45]. A series of 290,000 random sets of n features (where $n = 2, 3, 4, \dots, 29, 30$; with 10,000 random sets per value of n) were generated and individually used to build a random forest classifier for each patient outcome using the exact same approach used in our model. The accuracy and p -value of our model were compared with this empirical estimate of the null distribution. We observed that while 156,282 random signatures were prognostic at $p < 0.05$ (53.89% of total), our model was superior to 99.92% of all signatures tested (Fig 7B). Together, these data provide strong evidence that our angiogenesis signature is already near its optimum prognostic power.

Because we used age and tumor stage, which are not strictly angiogenic features, we next analyzed the contribution of each individual feature to the final model. We observed that while age and tumor stage contribute to the model, as expected, the addition of the OIR genes increased substantially the prognostic power of our signature. Together, the OIR genes contributed to more than half (close to 60%) of the prognostic power in the final model (Fig 7C). Finally, to confirm that the 11 genes featured in the final model indeed participate in pathological angiogenesis, we performed real time PCR for the remaining 9 OIR genes selected by the

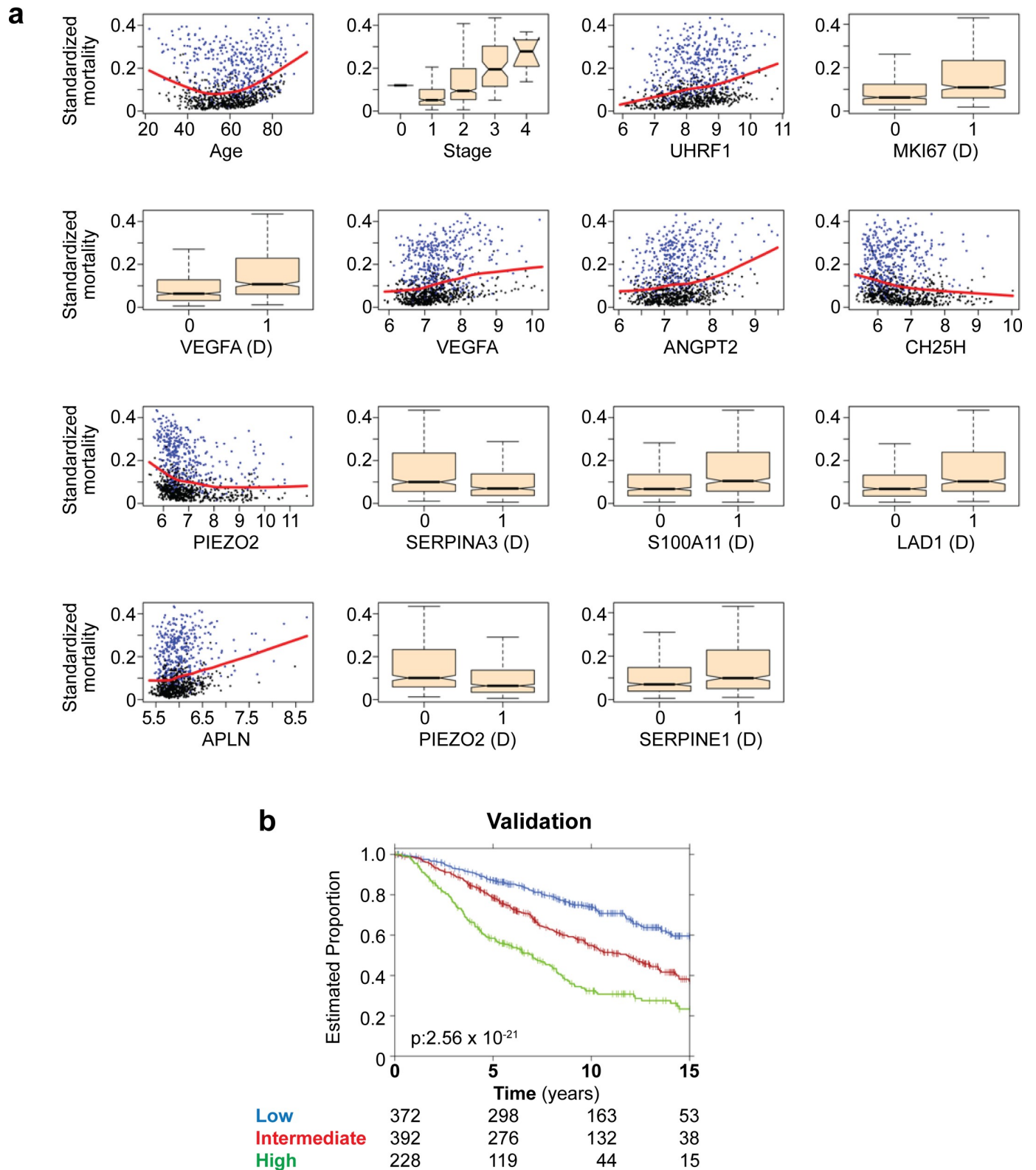


Fig 6. Machine learning and an angiogenesis signature with prognostic power. (a) Features used in gene signature. Patient's age, stage of cancer and 13 (11 genes) expression-based features were used with Random Forest to build a signature for prediction of breast cancer relapse with D representing discretized (binary) expression values. (b) RandomForestSRC algorithm was trained on a dataset of 56 features (54 angiogenesis-induced genes plus age and tumor stage)

using the METABRIC training cohort. The resulting classifier was applied on the validation cohort and was able to separate patients into three groups with significantly different outcomes. Low-risk (more than 15 years), intermediate-risk (between 15 and 7.5 years) and high-risk (less than 7.5 years).

<https://doi.org/10.1371/journal.pgen.1008482.g006>

random forest model (*VEGF* and *SERPINA3* had already been validated, Fig 1C). Again, the RT-PCR and RNA-seq data were in agreement and confirmed that all genes in the signature were up-regulated in pathological angiogenesis (S2A Fig) with a strong linear correlation between the abundance values obtained with each of the two technologies ($r_2 = 0.94$; $p_R = 4.47 \times 10^{-13}$; S2B Fig).

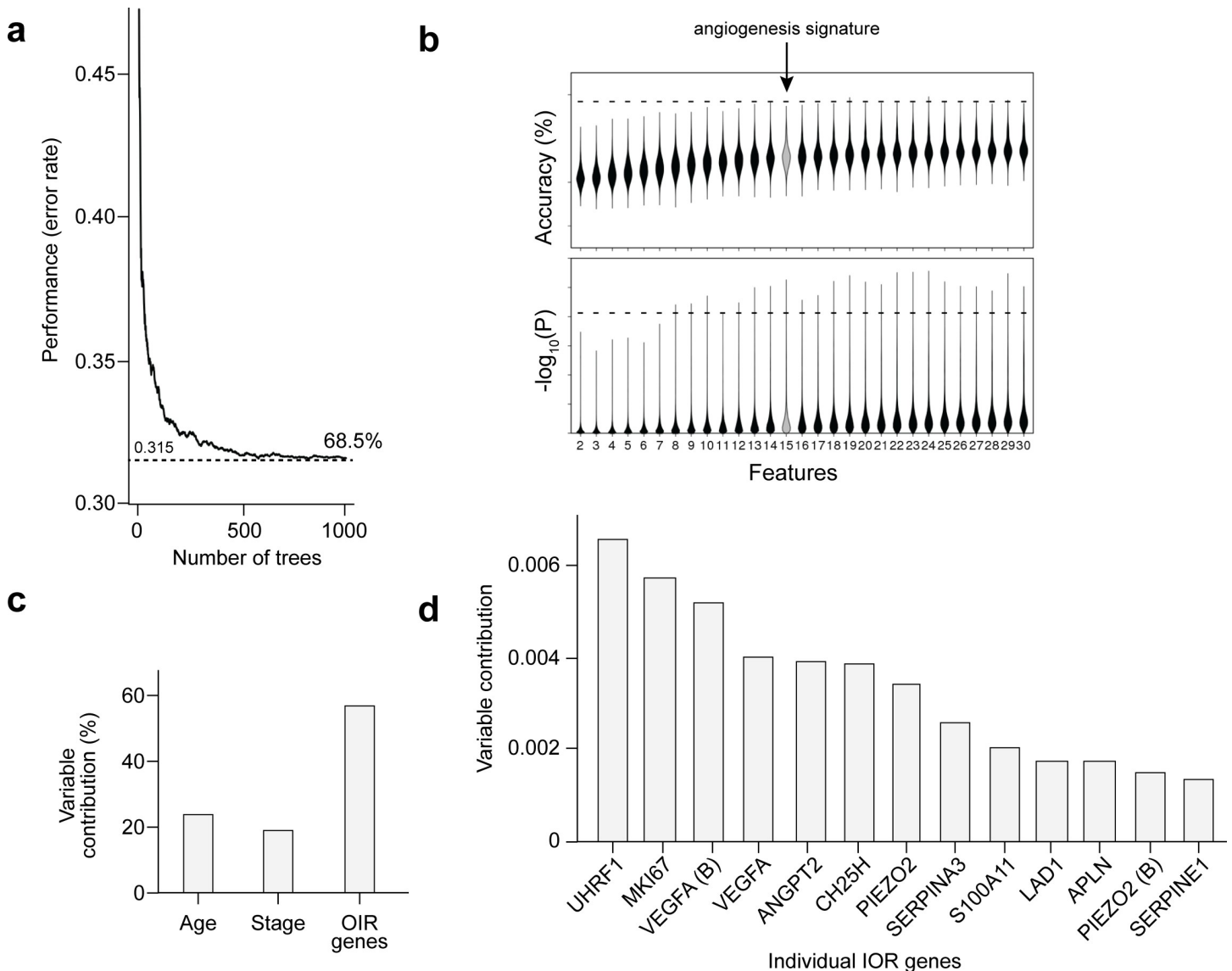


Fig 7. Machine learning performance and OIR gene contribution. (a) Performance (error rate) per number of tree generated by the random forest algorithm. (b) Resulting classifier was evaluated against a null distribution of classifiers. The y axis of top plot indicates the accuracy while the bottom plot highlights the $-\log_{10}(P)$. Larger values indicate a lower P-value and hence a more statistically significant separation of patient groups in the validation dataset. Dashed lines indicate performance of chosen model; Gray object highlight the number of features used on the chosen model; the same strategy of stratifying samples on low, intermediate and high-risk group was applied and evaluated using the log-rank test. (c and d) Contribution of each feature (age, stage or IOR genes) for the prognostic power of the algorithm.

<https://doi.org/10.1371/journal.pgen.1008482.g007>

Prognostic value according to tumor subtype

Breast cancer is a heterogeneous disease, with at least four molecular subtypes [46]. Given that patients from each subtype respond differently to therapy, we asked how well our angiogenesis signature would work in each molecular subtype. Patients with breast cancer molecular subtypes luminal A ($p = 9.15 \times 10^{-15}$; log-rank test), luminal B ($p = 8.47 \times 10^{-5}$; log-rank test) and basal ($p = 1.51 \times 10^{-4}$; log-rank test) were among those that could be best classified according to our gene signature. On the other hand, our model could not classify breast cancer patients in the HER2-positive ($p = 0.11$; log-rank test) (Fig 8A) or normal-like ($p = 0.58$; log-rank test) tumor subtypes (S3 Fig). It is noteworthy that none of the previously published angiogenesis gene signatures could predict patient survival with levels of accuracy as high as ours. We evaluated all nine earlier angiogenesis signatures and none were a robust biomarker in the METABRIC dataset (Fig 8B and 8C; S4 Fig).

Discussion

Angiogenesis is a hallmark of cancer and a necessary process to provide the growing tumors with nutrients and oxygen [1,9]. But pathological angiogenesis is not limited to neoplastic disorders and also participates in well-known angiogenesis-dependent diseases, which include retinopathy [2]. Thus, our angiogenesis gene signature is a welcome finding, and it is not entirely surprising that a mouse model for retinopathy could provide such a strong prognostic gene signature for a human disease, breast cancer. The concept that angiogenesis is an “organizing principle” has been proposed more than 10 year ago by Judah Folkman [2]. Indeed, all vertebrate metazoans use angiogenesis through conserved mechanisms (hypoxia, *HIF*, *VEGF* and other shared genes). Based on these premises, drugs that have been initially developed for treating oncologic patients have now been successfully translated for the treatment of a novel and completely unrelated set of diseases (ocular diseases). Therefore, it is not unexpected to identify a gene signature shared by these “seemingly” unrelated diseases, as presented in this study. In fact, the identification of an effective angiogenesis signature has so far eluded researchers, perhaps because of the challenges in identifying angiogenesis-associated genes. We reasoned that by performing RNA-seq in a well-suited animal model such as the OIR, we would identify a significant number of genes relevant to human angiogenesis-dependent diseases. Furthermore, by using a reliable isogenic animal model, we also avoided the genetic variability of human samples and other confounding factors present in most angiogenesis models (scaffolds, matrigel, viral vector or growth factor administration). In the OIR model, neovascularization is elegantly induced in mouse retinas by varying oxygen levels administered to the animals, closely recapitulating what happens with premature babies, therefore, already providing a model of a human disease (retinopathy of prematurity)[20,47]. Our results thus agree with angiogenesis being an organizing principle preserved in evolution and in health and disease, as proposed by the late Dr. Judah Folkman [2].

The final model of our gene signature included 13 gene-features (11 unique genes), most of them directly implicated in angiogenesis. *UHRF1*, also known as *ICBP90*, is an epigenetic regulator, a tumor marker for breast cancer [48], which also modulates epigenetically *VEGF* gene expression [49]. *VEGF*, *ANGPT2* and *APLN* are well known players in angiogenesis [5,6]. *PIEZO2* is a mechanosensitive ion-channel important in tumor angiogenesis and vascular permeability [50]. *SERPINE1* has also been implicated in angiogenesis and pharmacological blockage of serpine1 protein (PAI-1) inhibits tumor angiogenesis [51]. Finally, *LAD1* gene methylation is a potential biomarker for angiogenesis therapy in renal cancer [52]. Taken together, these data indicate that 9 out of 13 gene-features (70%) in our final model are directly implicated in tumor angiogenesis activity. However, none of the previously described

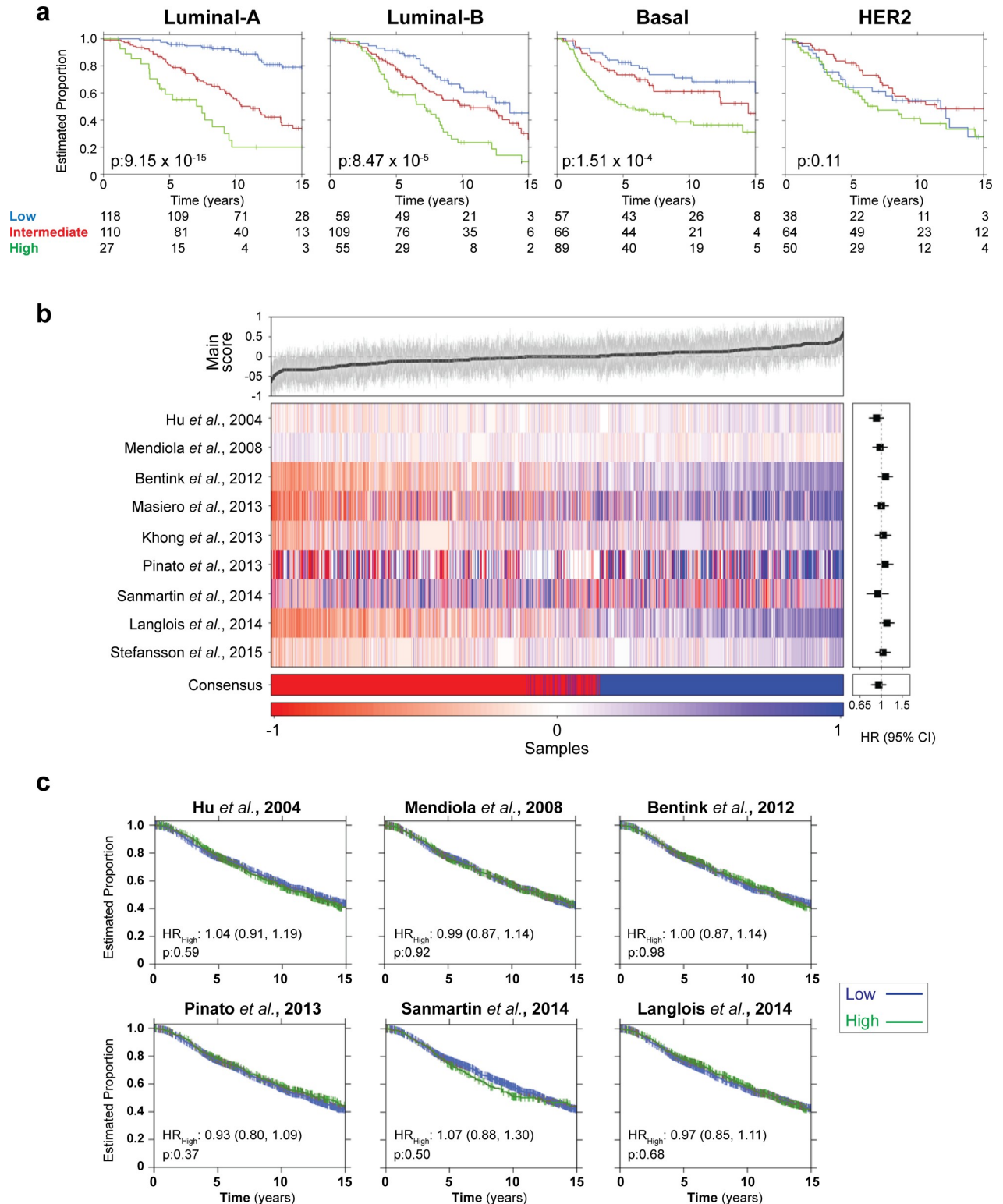


Fig 8. Breast cancer sub-types and comparison with other gene signatures. (a) Overall survival for each of the PAM50 subtypes was observed. Shown the Kaplan-Meier survival curves for Basal, Luminal-A, Luminal-B and Her2 subtypes. p-values were calculated using log-rank test. Six samples did not have a PAM50 class assigned and were excluded. Low-risk (more than 15 years), intermediate-risk (between 15 and 7.5 years) and high-risk (less than 7.5 years) (b) All nine previously published angiogenesis signature were assessed on METABRIC cohort. The heatmap shows the score between -1 and 1 for each sample (heatmap on center). Top plot depicts median score obtained from all nine signatures, gray lines highlight

standard deviation. Bottom depicts consensus call of all nine signatures combined. On right, forest plot shows hazard ratio, lines represent 95% confidence interval. (c) Survival curves for 6 representative angiogenesis signatures. Groups were dichotomized based on signature score: high-risk (score greater than the percentile of events) and a low-risk (score less than or equal to the percentile of events).

<https://doi.org/10.1371/journal.pgen.1008482.g008>

angiogenesis and hypoxia signatures used a similar combination or even a subset of these 11 genes. Only two previously described signatures combined at most two genes present in our model: *VEGF* and *SERPINE1* [41] or *SERPINE1* and *SERPINA3* [29]. Thus, our angiogenesis gene signature is unique. Of course, not all angiogenesis is the same. So, an interesting question that future studies may address is whether this same set of 11 genes or other combinations of genes derived from the OIR transcriptome will be prognostic for other types of tumors or angiogenesis dependent diseases.

It is significant that our gene signature showed such strong prognostic value in breast cancer considering the confounding benefits of anti-angiogenesis therapy for these patients [8,53,54]. In agreement with clinical data and the fact that the OIR model relies on hypoxia and VEGF to induce angiogenesis, our gene signature performs well for the subtypes of breast cancer tumors that respond to anti-VEGF therapy (basal, luminal A and B), while it has no prognostic value for patients with the HER2+ subtype for which anti-VEGF therapy has no effect [55]. HER2 is an orphan receptor with a very active intracellular domain, whose activation leads to the increased production of VEGF-A and HIF1A, regardless of hypoxia [56,57]. These different mechanisms of activation of angiogenic pathways may explain why our gene signature, which is derived by a model driven by hypoxia, did not perform well in a HER2-driven angiogenesis context [57]. Nevertheless, our results emphasize the contribution of hypoxia and VEGF-driven angiogenesis in specific subtypes of breast cancer. It may also provide a new blueprint for the development of gene signatures and discovery of biomarkers for human disease.

Materials and methods

Ethics statement

Animal study ethical approval was granted by the Animal Study Ethics Committee from the Institute of Chemistry (approval #10/2010).

Mouse model of ROP (OIR)

Mice (C57BL/6, Takoniks) were housed at the Animal Research Facility of the Chemistry Department, University of Sao Paulo. Newborn mice with their nursing mothers were kept on cages with food and water *ad libitum*. For the OIR model, the animals were exposed to 75% oxygen between P7 and 12, and then returned to room air (~20.8% O₂) until sample collection at the specified day and time [18].

RNA extraction, sequencing and analysis

Retinas from mice at four developmental stages (P12, P15 and P17; and at P12.5 – 12h after leaving the 75% oxygen chamber) were dissected in RNAlater (Qiagen) and total RNA was extracted using Qiagen RNeasy Mini Kit (Qiagen). Two OIR experiments were performed and then RNA from 4 animals (retinas N = 8) from each individual experiment were pooled to form the biological duplicates. Samples were treated with DNase (TURBO DNA-free, Thermo Fisher Scientific) following manufacturer's protocol and the absence of genomic DNA contamination was confirmed by RT-PCR and was found to be <3 pg/ml. Library preparation and sequencing was performed at the Next Generation Sequencing Core from Scripps

Research Institute (San Diego, CA). Strand-specific libraries were generated enriching for polyadenylated transcripts using the NEB Next Ultra Directional RNA Library Prep Kit for Illumina (New England BioLabs), following manufacturer's protocol. Purified libraries were quantitated using the Qubit quantitation platform (Invitrogen) and sized using RNA Nano Chip (Agilent). Single-read sequencing was performed on the Illumina HiSeq 2000 platform and demultiplexed based on index sequences. RNA-seq reads were mapped with STAR (version 2.5.1b) using 2-pass mapping with annotation procedure. *Mus musculus* GRCm38.p4 was used as reference genome and GRCm38.83 as reference annotation. Alignments were summarized by gene on counting tables using HTSeq-count (version 0.6.1p1); alignments with quality lower than 10 were discarded.

Gene expression analysis

Differential gene expression analysis was carried out with DESeq2 (version 1.14.1) and control samples were used as baselines. Genes with fold-change greater than 2 (\log_2) and adjusted p-values < 0.05 were considered as differentially expressed and used on further analysis. Benjamini-Hochberg procedure was used for multiple testing correction. For active genes evaluation, all genes with 10 or more reads on two or more samples were deemed as expressed. Additional gene annotation and homology information was retrieved using biomaRt package (version 2.30.0).

Real-time PCR validation assays

A custom TaqMan low-density array (TLDA) card (Thermo-Fisher Scientific) containing 384-well microfluidic cards with eight ports, each made up of 48 connected wells (42 targets + 6 endogenous controls), was designed. Experiments were carried out using the Applied Biosystems 7900HT real-time PCR platform. Samples were individually tested (no pooling). Technical duplicated for each sample was used and failed experiments were omitted. GeNorm was used to test the most stable normalizers; Tbp (Mm00446971_m1) and Sdha (Mm01352363_m1) were selected and used on following analysis. Relative quantification analysis was performed on Thermo Fisher Cloud system. P12 samples were used as baselines for relative quantification. Experiments with CT > 35 were discarded due to high variance observed. The remaining genes featured in the final model for the angiogenesis gene signature (*Angpt2*, *Apln*, *Ch25h*, *Lad1*, *Mki67*, *Piezo2*, *Serpine1*, *S100a10* and *Uhrf1*) were validated separately. In brief, 500 ng of total RNA from mouse retinas (OIR or normal retinas) were converted to cDNA using supercript III (Invitrogen Thermo Fisher Scientific) using random hexaprimers. Quantitative PCR was then performed using the SYBR green PCR master mix (Applied Biosystems Thermo Fisher Scientific) and the specific primers (S3C Fig) according to the manufacture recommendations in a QuantStudio 3 Real-Time PCR System (at the Center for Advanced Technologies in Genomic [CATG], Chemistry Institute, University of São Paulo, Brazil).

Pathway analyses

Enriched pathways, functions and disease annotations were computed using the IPA platform (Qiagen).

METABRIC data pre-processing

Raw METABRIC breast cancer dataset files [44] were downloaded from the European genome-phenome archive (Study ID: EGAS00000000083). Data was pre-processed,

summarized and quantile-normalized from raw abundance files generated via Illumina Bead-Studio (R packages: beadarray (v2.4.2) and illuminaHuman (v3.db_1.12.2)). Data files from one subject were not available and accordingly excluded, resulting in a total of 1988 subjects. This dataset was divided into a training cohort ($n = 996$) and a validation cohort ($n = 992$) for subsequent analysis. Survival data was truncated at 15 years follow-up time.

Evaluation of existing signatures on METABRIC dataset

Training and validation set from METABRIC were combined and each signature was used to score each sample. Features were weighted respecting the expression information provided: +1 for up-regulated genes and -1 for down-regulated ones. If a signature had no expression information, all weights were set to +1. Scores for each sample were normalized between -1 and +1 and samples dichotomized according the percentile of events in the dataset. This sample classification was used to fit a Cox proportional hazard model where hazard ratios were calculated [58]. Median and standard deviation of scores between angiogenesis signatures for each sample were calculated. Majority vote between all angiogenesis signatures was used to call the consensus signature.

Human homolog genes

Out of the 153 DE mouse genes, 10 genes did not have human homologs (*Fgf2os*, *Muc2*, *Gm15983*, *Gm12802*, *Gm43620*, *H2-Q2*, *H2-Q6*, *Gm35040*, *H2-T23*, *H2-K1*). For the remaining 143 genes, there were cases in which a single mouse gene mapped to multiple human genes (*H2-Ab1*, *H2-Q7*, *Ifitm3*), resulting in 149 human genes. This is the number that was used for comparison with previously published gene angiogenesis and hypoxia signatures (Fig 4C). For building the gene signature, 3 genes within the 149 human homologs were not arrayed on the platform used in the METABRIC study (*ADGRL4*, *HLA-DQB2*, *ITGA1*), thus yielding a total of 146 human genes used in the algorithm. For each of the 146 differentially expressed genes in angiogenesis, continuous and discrete expression information was used [58].

Survival analysis and signature creation

For discretization, expression values were median dichotomized across all samples in the dataset. We performed univariate analysis (Cox model) for each gene and only genes with a p -value < 0.05 were considered on further analysis. Age of diagnosis and tumor stage were supplied for each sample whenever available. We have used randomForestSRC package (v2.2.0) (Ref. [26,53]) to build the model. In summary, features were ranked by p -value and models were built by sequentially adding features (*i.e.* forward selection). The model with the minimum error was chosen as the final model. Model was applied on the validation samples (not used during training). Patient's predicted probability of survival was used to assign a class using the following sequential criteria: low-risk if $P(\text{survival at 15 years}) > 0.5$; intermediate-risk if $P(\text{survival at 7.5 years}) > 0.5$; high-risk otherwise. 7.5 years represents the half of the dataset follow-up time after truncation.

Permutation analysis

To evaluate model's performance against a null distribution, we have used the same strategy as described previously [26,58]. In summary, we restricted the analysis to the same 302 features used for the signature's creation (149 genes with continuous and discrete information, plus age and stage). We then generated 10 million permutations of 14 features (same number of predictors used in our signature) using METABRIC training for the model's training. We

calculated statistical significance for each model using a log-rank test on METABRIC validation dataset.

Data visualization

Data visualization was performed with the lattice (v0.20–33), latticeExtra (v0.6–28) and BPG (v 5.6.8) packages [59].

Supporting information

S1 Fig. Comparison of gene expression quantified by RNA-seq and RT-PCR. (a). Expression profile of 42 selected genes quantified by RNA-Seq and RT-PCR methods. Bars represent standard error of the mean from independent biological samples (N = 8). Fold-changes were calculated relative to P12 samples. (b) Correlation between expression values calculated by RNA-seq and RT-PCR.

(PDF)

S2 Fig. Expression of the remaining OIR genes featured in the final model by qRT-PCR and comparison with the RNA-seq data. (a) Expression profile of 9 selected genes quantified by RNA-Seq and qRT-PCR methods. Bars represent standard error of the mean from independent biological samples (N = 4). Fold-changes were calculated relative to P12 samples. (b) Correlation between expression values calculated by RNA-seq and RT-PCR. (c) Table listing the sequences of the oligonucleotides utilized for the qRT-PCR reactions. (The results for the remaining genes featured in the final model, Vegf and Serpina3n, are shown in Fig 1C in the main text of the manuscript.)

(PDF)

S3 Fig. Prognostic power of angiogenesis signature on Normal-like breast cancer tumor type. Our model could not distinguish breast cancer patients with normal-like (P = 0.58; log-rank test) tumor subtypes. It is important to note that this type of tumor had the smallest sample of all breast cancer tumor types in the METABRIC dataset.

(PDF)

S4 Fig. Prognostic power of existing angiogenesis signature. All nine previously published angiogenesis signature were assessed on METABRIC cohort. Survival curves of groups (low and high risk) determined by all 9 angiogenesis gene signatures.

(PDF)

S1 Table. RNA-seq sequencing summary.

(PDF)

S2 Table. List of 153 genes differentially regulated in pathological angiogenesis.

(PDF)

S3 Table. Gene used in previously described gene signatures for angiogenesis and hypoxia.

(PDF)

S4 Table. Genes shared by all gene signatures.

(PDF)

S5 Table. Remaining features after p-value (P<0.05) filtering (METABRIC).

(PDF)

S1 File. Rdata object containing the final model for the angiogenesis gene signature.

(ZIP)

Acknowledgments

We thank M. L. Baldini, C. L. Braga and C. Moraes for providing technical support, and Dr. M.H. Starman and V. Bhandari for assistance compiling hypoxia gene signatures.

Author Contributions

Conceptualization: Rodrigo Guarischi-Sousa, Jussara S. Michaloski, Jüri Reimand, Paul C. Boutros, João C. Setubal, Ricardo J. Giordano.

Data curation: Rodrigo Guarischi-Sousa, Jhonatas S. Monteiro, Lilian C. Alecrim, Jussara S. Michaloski, Laura B. Cardeal, Elisa N. Ferreira, Dirce M. Carraro, Diana N. Nunes, Emmanuel Dias-Neto, Jüri Reimand, Paul C. Boutros, João C. Setubal, Ricardo J. Giordano.

Formal analysis: Rodrigo Guarischi-Sousa, Jussara S. Michaloski, Laura B. Cardeal, Elisa N. Ferreira, Dirce M. Carraro, Diana N. Nunes, Emmanuel Dias-Neto, Jüri Reimand, Paul C. Boutros, João C. Setubal, Ricardo J. Giordano.

Funding acquisition: João C. Setubal, Ricardo J. Giordano.

Methodology: Rodrigo Guarischi-Sousa, Jhonatas S. Monteiro, Lilian C. Alecrim, Jussara S. Michaloski, Laura B. Cardeal, Elisa N. Ferreira, Dirce M. Carraro, Diana N. Nunes, Emmanuel Dias-Neto, Jüri Reimand, Paul C. Boutros, João C. Setubal, Ricardo J. Giordano.

Resources: Rodrigo Guarischi-Sousa, Jhonatas S. Monteiro, Jussara S. Michaloski, Emmanuel Dias-Neto, Jüri Reimand, Paul C. Boutros, João C. Setubal, Ricardo J. Giordano.

Supervision: Paul C. Boutros, João C. Setubal, Ricardo J. Giordano.

Validation: Jhonatas S. Monteiro, Lilian C. Alecrim.

Writing – original draft: Rodrigo Guarischi-Sousa, Jussara S. Michaloski, Laura B. Cardeal, Elisa N. Ferreira, Dirce M. Carraro, Diana N. Nunes, Emmanuel Dias-Neto, Jüri Reimand, Paul C. Boutros, João C. Setubal, Ricardo J. Giordano.

Writing – review & editing: Rodrigo Guarischi-Sousa, Jhonatas S. Monteiro, Lilian C. Alecrim, Jüri Reimand, Paul C. Boutros, João C. Setubal, Ricardo J. Giordano.

References

1. Folkman J. Tumor angiogenesis: therapeutic implications. *N Engl J Med.* 1971; 285:1182–6. <https://doi.org/10.1056/NEJM197111182852108> PMID: 4938153
2. Folkman J. Angiogenesis: an organizing principle for drug discovery? *Nat Rev Drug Discov.* 2007; 6:273–86. <https://doi.org/10.1038/nrd2115> PMID: 17396134
3. Cao Y, Arbiser J, D'Amato RJ, D'Amore PA, Ingber DE, Kerbel R, Klagsbrun M, Lim S, Moses MA, Zetter B, Dvorak H, Langer R. Forty-year journey of angiogenesis translational research. *Sci Transl Med.* 2011; 3:114rv3. <https://doi.org/10.1126/scitranslmed.3003149> PMID: 22190240
4. Ferrara N, Adamis AP. Ten years of anti-vascular endothelial growth factor therapy. *Nat Rev Drug Discov.* 2016; 15:385–403. <https://doi.org/10.1038/nrd.2015.17> PMID: 26775688
5. Jain RK. Antiangiogenesis strategies revisited: from starving tumors to alleviating hypoxia. *Cancer Cell.* 2014; 26:605–22. <https://doi.org/10.1016/j.ccell.2014.10.006> PMID: 25517747
6. Karaman S, Leppänen VM, Alitalo K. Vascular endothelial growth factor signaling in development and disease. *Development.* 2018; 145, pii:dev151019.
7. Bahrami B, Zhu M, Hong T, Chang A. Diabetic macular oedema: pathophysiology, management challenges and treatment resistance. *Diabetologia.* 2016; 59:1594–608. <https://doi.org/10.1007/s00125-016-3974-8> PMID: 27179659
8. Montero AJ, Escobar M, Lopes G, Glück S, Vogel C. Bevacizumab in the treatment of metastatic breast cancer: friend or foe? *Curr. Oncol. Rep.* 2012; 14:1–11. <https://doi.org/10.1007/s11912-011-0202-z> PMID: 22012632

9. Hanahan D, Weinberg RA. Hallmarks of cancer: the next generation. *Cell*. 2011; 144(5):646–74. <https://doi.org/10.1016/j.cell.2011.02.013> PMID: 21376230
10. Iida N, Dzutsev A, Stewart CA, Smith L, Bouladoux N, Weingarten RA, Molina DA, Salcedo R, Back T, Cramer S, Dai RM, Kiu H, Cardone M, Naik S, Patri AK, Wang E, Marincola FM, Frank KM, Belkaid Y, Trinchieri G, Goldszmid RS. Commensal bacteria control cancer response to therapy by modulating the tumor microenvironment. *Science*. 2013; 342:967–70. <https://doi.org/10.1126/science.1240527> PMID: 24264989
11. Mlecnik B, Bindea G, Kirilovsky A, Angell HK, Obenauf AC, Tosolini M, Church SE, Maby P, Vasaturo A, Angelova M, Fredriksen T, Mauger S, Waldner M, Berger A, Speicher MR, Pagès F, Valge-Archer V, Galon J. The tumor microenvironment and Immunoscore are critical determinants of dissemination to distant metastasis. *Sci Transl Med*. 8:327ra26 (2016). <https://doi.org/10.1126/scitranslmed.aad6352> PMID: 26912905
12. Espiritu SMG, Liu LY, Rubanova Y, Bhandari V, Holgersen EM, Szyca LM, Fox NS, Chua MLK, Yamaguchi TN, Heisler LE, Livingstone J, Wintersinger J, Yousif F, Lalonde E, Rouette A, Salcedo A, Houlihan KE, Li CH, Huang V, Fraser M, van der Kwast T, Morris QD, Bristow RG, Boutros PC. The evolutionary landscape of localized prostate cancers drives clinical aggression. *Cell* 2018; 173:1003–1013. <https://doi.org/10.1016/j.cell.2018.03.029> PMID: 29681457
13. Lahdenranta J, Pasqualini R, Schlingemann RO, Hagedorn M, Stallcup WB, Bucana CD, Sidman RL, Arap W. An anti-angiogenic state in mice and humans with retinal photoreceptor cell degeneration. *Proc Natl Acad Sci U. S. A.* 2001; 98:10368–73. <https://doi.org/10.1073/pnas.181329198> PMID: 11526242
14. Giordano RJ, Cardó-Vila M, Salameh A, Anobom CD, Zeitlin BD, Hawke DH, Valente AP, Almeida FC, Nör JE, Sidman RL, Pasqualini R, Arap W. From combinatorial peptide selection to drug prototype (I): targeting the vascular endothelial growth factor receptor pathway. *Proc Natl Acad Sci U. S. A.* 2010; 107:5112–7. <https://doi.org/10.1073/pnas.0915141107> PMID: 20190181
15. Cloutier F, Lawrence M, Goody R, Lamoureux S, Al-Mahmood S, Colin S, Ferry A, Conduzorgues JP, Hadri A, Cursiefen C, Udaondo P, Viaud E, Thorin E, Chemtob S. Antiangiogenic activity of aganirsén in nonhuman primate and rodent models of retinal neovascular disease after topical administration. *Invest Ophthalmol Vis Sci*. 2012; 53:1195–203. <https://doi.org/10.1167/iovs.11-9064> PMID: 22323484
16. Sidman RL, Li J, Lawrence M, Hu W, Musso GF, Giordano RJ, Cardó-Vila M, Pasqualini R, Arap W. The peptidomimetic Vasotide targets two retinal VEGF receptors and reduces pathological angiogenesis in murine and nonhuman primate models of retinal disease. *Sci Transl Med*. 2015; 7:309ra165. <https://doi.org/10.1126/scitranslmed.aac4882> PMID: 26468327
17. Nunes DN, Dias-Neto E, Cardó-Vila M, Edwards JK, Dobroff AS, Giordano RJ, Mandelin J, Brentani HP, Hasselgren C, Yao VJ, Marchiò S, Pereira CA, Passetti F, Calin GA, Sidman RL, Arap W, Pasqualini R. Synchronous down-modulation of miR-17 family members is an early causative event in the retinal angiogenic switch. *Proc Natl Acad Sci U. S. A.* 2015; 112:3770–5. <https://doi.org/10.1073/pnas.1500008112> PMID: 25775553
18. Michaloski JS, Redondo AR, Magalhães LS, Cambui CC, Giordano RJ. Discovery of pan-VEGF inhibitory peptides directed to the extracellular ligand-binding domains of the VEGF receptors. *Sci Adv*. 2016; 2:e1600611. <https://doi.org/10.1126/sciadv.1600611> PMID: 27819042
19. Smith LE, Wesolowski E, McLellan A, Kostyk SK, D'Amato R, Sullivan R, D'Amore PA. Oxygen-induced retinopathy in the mouse. *Invest. Ophthalmol. Vis. Sci.* 1994; 35:101–111. PMID: 7507904
20. Stahl A, Connor KM, Sapieha P, Chen J, Dennison RJ, Krahn NM, Seaward MR, Willett KL, Aderman CM, Guerin KI, Hua J, Löfquist C, Hellström A, Smith LE. The mouse retina as an angiogenesis model. *Invest Ophthalmol Vis Sci*. 2010; 51:2813–26. <https://doi.org/10.1167/iovs.10-5176> PMID: 20484600
21. Hellström A, Smith LE, Dammann O, Dammann O. Retinopathy of prematurity. *Lancet*. 2013; 382:1445–57. [https://doi.org/10.1016/S0140-6736\(13\)60178-6](https://doi.org/10.1016/S0140-6736(13)60178-6) PMID: 23782686
22. Scott A, Fruttiger M. Oxygen-induced retinopathy: a model for vascular pathology in the retina. *Eye (London)* 2010; 24:416–21.
23. Masland RH. The neuronal organization of the retina. *Neuron*. 2012; 76:266–80. <https://doi.org/10.1016/j.neuron.2012.10.002> PMID: 23083731
24. Carmeliet P. Blood vessels and nerves: common signals, pathways and diseases. 2003; *Nat Rev Genet*. 4:710–20. <https://doi.org/10.1038/nrg1158> PMID: 12951572
25. Licht T, Keshet E. Delineating multiple functions of VEGF-A in the adult brain. *Cell Mol. Life Sci*. 2013; 70:1727–37. <https://doi.org/10.1007/s00018-013-1280-x> PMID: 23475068
26. Boutros PC, Lau SK, Pintilie M, Liu N, Shepherd FA, Der SD, Tsao MS, Penn LZ, Jurisica I. Prognostic gene signatures for non-small-cell lung cancer. *Proc Natl Acad Sci U S A.* 2009; 106:2824–8. <https://doi.org/10.1073/pnas.0809444106> PMID: 19196983
27. Starmans MH, Chu KC, Haider S, Nguyen F, Seigneuric R, Magagnin MG, Koritzinsky M, Kasprzyk A, Boutros PC, Wouters BG, Lambin P. The prognostic value of temporal in vitro and in vivo derived

- hypoxia gene-expression signatures in breast cancer. *Radiother Oncol.* 2012; 102:436–43. <https://doi.org/10.1016/j.radonc.2012.02.002> PMID: 22356756
28. Stefansson IM, Raeder M, Wik E, Mannelqvist M, Kusonmano K, Knutsvik G, Haldorsen I, Trovik J, Øyan AM, Kalland KH, Staff AC, Salvesen HB, Akslen LA. Increased angiogenesis is associated with a 32-gene expression signature and 6p21 amplification in aggressive endometrial cancer. *Oncotarget.* 2015; 6:10634–45. <https://doi.org/10.18632/oncotarget.3521> PMID: 25860936
 29. Langlois B, Saupe F, Rupp T, Arnold C, van der Heyden M, Orend G, Hussenet T. AngioMatrix, a signature of the tumor angiogenic switch-specific matrisome, correlates with poor prognosis for glioma and colorectal cancer patients. *Oncotarget.* 2014; 5:10529–45. <https://doi.org/10.18632/oncotarget.2470> PMID: 25301723
 30. Sanmartín E, Sirera R, Usó M, Blasco A, Gallach S, Figueroa S, Martínez N, Hernando C, Honguero A, Martorell M, Guijarro R, Rosell R, Jantus-Lewintre E, Camps C. A gene signature combining the tissue expression of three angiogenic factors is a prognostic marker in early-stage non-small cell lung cancer. *Ann Surg Oncol.* 2014; 21:612–20. <https://doi.org/10.1245/s10434-013-3330-x> PMID: 24145997
 31. Pinato DJ, Tan TM, Toussi ST, Ramachandran R, Martin N, Meeran K, Ngo N, Dina R, Sharma R. An expression signature of the angiogenic response in gastrointestinal neuroendocrine tumours: correlation with tumour phenotype and survival outcomes. *Br J Cancer* 2014; 110:115–122. <https://doi.org/10.1038/bjc.2013.682> PMID: 24231952
 32. Khong TL, Thairu N, Larsen H, Dawson PM, Kiriakidis S, Paleolog EM. Identification of the angiogenic gene signature induced by EGF and hypoxia in colorectal cancer. *BMC Cancer.* 2013; 13:518. <https://doi.org/10.1186/1471-2407-13-518> PMID: 24180698
 33. Masiero M, Simões FC, Han HD, Snell C, Peterkin T, Bridges E, Mangala LS, Wu SY, Pradeep S, Li D, Han C, Dalton H, Lopez-Berestein G, Tuynman JB, Mortensen N, Li JL, Patient R, Sood AK, Banham AH, Harris AL, Buffa FM. A core human primary tumor angiogenesis signature identifies the endothelial orphan receptor ELTD1 as a key regulator of angiogenesis. *Cancer Cell.* 2013; 24:229–41. <https://doi.org/10.1016/j.ccr.2013.06.004> PMID: 23871637
 34. Bentink S, Haibe-Kains B, Risch T, Fan JB, Hirsch MS, Holton K, Rubio R, April C, Chen J, Wickham-Garcia E, Liu J, Culhane A, Drapkin R, Quackenbush J, Matulonis UA. Angiogenic mRNA and micro-RNA gene expression signature predicts a novel subtype of serous ovarian cancer. *PLoS One.* 2012; 7:e30269. <https://doi.org/10.1371/journal.pone.0030269> PMID: 22348002
 35. Mendiola M, Barriuso J, Redondo A, Mariño-Enríquez A, Madero R, Espinosa E, Vara JA, Sánchez-Navarro I, Hernández-Cortés G, Zamora P, Pérez-Fernández E, Miguel-Martín M, Suárez A, Palacios J, González-Barón M, Hardisson D. Angiogenesis-related gene expression profile with independent prognostic value in advanced ovarian carcinoma. *PLoS One.* 2008; 3:e4051. <https://doi.org/10.1371/journal.pone.0004051> PMID: 19112514
 36. Hu J, Bianchi F, Ferguson M, Cesario A, Margaritora S, Granone P, Goldstraw P, Tetlow M, Ratcliffe C, Nicholson AG, Harris A, Gatter K, Pezzella F. Gene expression signature for angiogenic and nonangiogenic non-small-cell lung cancer. *Oncogene.* 2005; 24:1212–9. <https://doi.org/10.1038/sj.onc.1208242> PMID: 15592519
 37. Sørensen BS, Toustrup K, Horsman MR, Overgaard J, Alsner J. Identifying pH independent hypoxia induced genes in human squamous cell carcinomas in vitro. *Acta Oncol.* 2010; 49(7):895–905. <https://doi.org/10.3109/02841861003614343> PMID: 20429727
 38. Buffa FM, Harris AL, West CM, Miller CJ. Large meta-analysis of multiple cancers reveals a common, compact and highly prognostic hypoxia metagene. *Br J Cancer.* 2010; 102:428–35. <https://doi.org/10.1038/sj.bjc.6605450> PMID: 20087356
 39. Seigneuric R, Starmans MH, Fung G, Krishnapuram B, Nuyten DS, van Erk A, Magagnin MG, Rouschop KM, Krishnan S, Rao RB, Evelo CT, Begg AC, Wouters BG, Lambin P. Impact of supervised gene signatures of early hypoxia on patient survival. *Radiother Oncol.* 2007; 83:374–82. <https://doi.org/10.1016/j.radonc.2007.05.002> PMID: 17532074
 40. Winter SC, Buffa FM, Silva P, Miller C, Valentine HR, Turley H, Shah KA, Cox GJ, Corbridge RJ, Homer JJ, Musgrove B, Slevin N, Sloan P, Price P, West CM, Harris AL. Relation of a hypoxia metagene derived from head and neck cancer to prognosis of multiple cancers. *Cancer Res.* 2007; 67:3441–9. <https://doi.org/10.1158/0008-5472.CAN-06-3322> PMID: 17409455
 41. Elvidge GP, Glennly L, Appelhoff RJ, Ratcliffe PJ, Ragoussis J, Gleadle JM. Concordant regulation of gene expression by hypoxia and 2-oxoglutarate-dependent dioxygenase inhibition: the role of HIF-1alpha, HIF-2alpha, and other pathways. *J. Biol. Chem.* 2006; 281:15215–26. <https://doi.org/10.1074/jbc.M511408200> PMID: 16565084
 42. Chi JT, Wang Z, Nuyten DS, Rodríguez EH, Schaner ME, Salim A, Wang Y, Kristensen GB, Helland A, Børresen-Dale AL, Giaccia A, Longaker MT, Hastie T, Yang GP, van de Vijver MJ, Brown PO. Gene expression programs in response to hypoxia: cell type specificity and prognostic significance in human cancers. *PLoS Med.* 2006; 3:e47. <https://doi.org/10.1371/journal.pmed.0030047> PMID: 16417408

43. Hu Z, Fan C, Livasy C, He X, Oh DS, Ewend MG, Carey LA, Subramanian S, West R, Ikpat F, Olopade OI, van de Rijn M, Perou CM. A compact VEGF signature associated with distant metastases and poor outcomes. *BMC Med.* 2009; 7:9. <https://doi.org/10.1186/1741-7015-7-9> PMID: 19291283
44. Curtis C, Shah SP, Chin SF, Turashvili G, Rueda OM, Dunning MJ, Speed D, Lynch AG, Samarajiwa S, Yuan Y, Gräf S, Ha G, Haffari G, Bashashati A, Russell R, McKinney S; METABRIC Group, Langerød A, Green A, Provenzano E, Wishart G, Pinder S, Watson P, Markowitz F, Murphy L, Ellis I, Purushotham A, Børresen-Dale AL, Brenton JD, Tavaré S, Caldas C, Aparicio S. The genomic and transcriptomic architecture of 2,000 breast tumours reveals novel subgroups. *Nature.* 2012; 486:346–52. <https://doi.org/10.1038/nature10983> PMID: 22522925
45. Venet D, Dumont JE, Detours V. Most random gene expression signatures are significantly associated with breast cancer outcome. *PLoS Comput Biol.* 2011; 7:e1002240. <https://doi.org/10.1371/journal.pcbi.1002240> PMID: 22028643
46. Perou CM, Sørlie T, Eisen MB, van de Rijn M, Jeffrey SS, Rees CA, Pollack JR, Ross DT, Johnsen H, Akslen LA, Fluge O, Pergamenschikov A, Williams C, Zhu SX, Lønning PE, Børresen-Dale AL, Brown PO, Botstein D. Molecular portraits of human breast tumours. *Nature.* 2000; 406:747–52. <https://doi.org/10.1038/35021093> PMID: 10963602
47. Nowak-Sliwinska P, Alitalo K, Allen E, Anisimov A, Aplin AC, Auerbach R, Augustin HG, Bates DO, van Beijnum JR, Bender RHF, Bergers G, Bikfalvi A, Bischoff J, Böck BC, Brooks PC, Bussolino F, Cakir B, Carmeliet P, Castranova D, Cimpean AM, Cleaver O, Coukos G, Davis GE, De Palma M, Dimberg A, Dings RPM, Djonov V, Dudley AC, Dufton NP, Fendt SM, Ferrara N, Fruttiger M, Fukumura D, Ghesquière B, Gong Y, Griffin RJ, Harris AL, Hughes CCW, Hultgren NW, Iruela-Arispe ML, Irving M, Jain RK, Kalluri R, Kalucka J, Kerbel RS, Kitajewski J, Klaassen I, Kleinmann HK, Koolwijk P, Kuczyński E, Kwak BR, Marien K, Melero-Martin JM, Munn LL, Nicosia RF, Noel A, Nurro J, Olsson AK, Petrova TV, Pietras K, Pili R, Pollard JW, Post MJ, Quax PHA, Rabinovich GA, Raica M, Randi AM, Ribatti D, Ruegg C, Schlingemann RO, Schulte-Merker S, Smith LEH, Song JW, Stacker SA, Stalin J, Stratman AN, Van de Velde M, van Hinsbergh VWM, Vermeulen PB, Waltenberger J, Weinstein BM, Xin H, Yetkin-Arik B, Yla-Herttuala S, Yoder MC, Griffioen AW. Consensus guidelines for the use and interpretation of angiogenesis assays. *Angiogenesis.* 2018; <https://doi.org/10.1007/s10456-018-9613-x> [Epub ahead of print] PMID: 29766399
48. Gao SP, Sun HF, Li LD, Fu WY, Jin W. UHRF1 promotes breast cancer progression by suppressing KLF17 expression by hypermethylating its promoter. *Am J Cancer Res.* 2017 Jul 1; 7(7):1554–1565. eCollection 2017. PMID: 28744404
49. Achour M, Jacq X, Rondé P, Alhosin M, Charlot C, Chataigneau T, Jeanblanc M, Macaluso M, Giordano A, Hughes AD, Schini-Kerth VB, Bronner C. The interaction of the SRA domain of ICBP90 with a novel domain of DNMT1 is involved in the regulation of VEGF gene expression. *Oncogene.* 2008 Apr 3; 27(15):2187–97. Epub 2007 Oct 15. <https://doi.org/10.1038/sj.onc.1210855> PMID: 17934516
50. Yang H, Liu C, Zhou RM, Yao J, Li XM, Shen Y, Cheng H, Yuan J, Yan B, Jiang Q. Piezo2 protein: A novel regulator of tumor angiogenesis and hyperpermeability. *Oncotarget.* 2016 Jul 12; 7(28):44630–44643. <https://doi.org/10.18632/oncotarget.10134> PMID: 27329839
51. Takayama Y, Hattori N, Hamada H, Masuda T, Omori K, Akita S, Iwamoto H, Fujitaka K, Kohno N. Inhibition of PAI-1 Limits Tumor Angiogenesis Regardless of Angiogenic Stimuli in Malignant Pleural Mesothelioma. *Cancer Res.* 2016 Jun 1; 76(11):3285–94. <https://doi.org/10.1158/0008-5472.CAN-15-1796> Epub 2016 Apr 13. PMID: 27197170
52. Peters I, Dubrowskaja N, Abbas M, Seidel C, Kogosov M, Scherer R, Gebauer K, Merseburger AS, Kuczyk MA, Grünwald V, Serth J. DNA methylation biomarkers predict progression-free and overall survival of metastatic renal cell cancer (mRCC) treated with antiangiogenic therapies. *PLoS One.* 2014 Mar 14; 9(3):e91440. <https://doi.org/10.1371/journal.pone.0091440> eCollection 2014. PMID: 24633192
53. Schwartzberg LS, Tauer KW, Hermann RC, Makari-Judson G, Isaacs C, Beck JT, Kaklamani V, Stephens EJ, Rugo HS, Wang W, Bell-McGuinn K, Kirshner JJ, Eisenberg P, Emanuelson R, Keaton M, Levine E, Medgyesy DC, Qamar R, Starr A, Ro SK, Lokker NA, Hudis CA. Sorafenib or placebo with either gemcitabine or capecitabine in patients with HER-2-negative advanced breast cancer that progressed during or after bevacizumab. *Clin. Can. Res.* 2013; 19: 2745–54.
54. Dirix LY, Reynolds AR. Bevacizumab beyond progression in breast cancer. *Lancet Oncol.* 2014; 15:1190–1. [https://doi.org/10.1016/S1470-2045\(14\)70454-1](https://doi.org/10.1016/S1470-2045(14)70454-1) PMID: 25273341
55. Gianni L, Romieu GH, Lichinitser M, Serrano SV, Mansutti M, Pivot X, Mariani P, Andre F, Chan A, Lipatov O, Chan S, Wardley A, Greil R, Moore N, Prot S, Pallaud C, Semiglazov V. AVEREL: a randomized phase III Trial evaluating bevacizumab in combination with docetaxel and trastuzumab as first-line therapy for HER2-positive locally recurrent/metastatic breast cancer. *J. Clin. Oncol.* 2013; 31:1719–25. <https://doi.org/10.1200/JCO.2012.44.7912> PMID: 23569311
56. Laughner E, Taghavi P, Chiles K, Mahon PC, Semenza GL. HER2 (neu) signaling increases the rate of hypoxia-inducible factor 1alpha (HIF-1alpha) synthesis: novel mechanism for HIF-1-mediated vascular

endothelial growth factor expression. *Mol Cell Biol.* 2001; 21(12):3995–4004. <https://doi.org/10.1128/MCB.21.12.3995-4004.2001> PMID: 11359907

57. Alameddine RS, Otrrock ZK, Awada A, Shamseddine A. Crosstalk between HER2 signaling and angiogenesis in breast cancer: molecular basis, clinical applications and challenges. *Curr Opin Oncol.* 2013; 25(3):313–24. <https://doi.org/10.1097/CCO.0b013e32835ff362> PMID: 23518595
58. Bhandari V, Boutros PC. Comparing continuous and discrete analyses of breast cancer survival information. *Genomics.* 2016; 108:78–83. <https://doi.org/10.1016/j.ygeno.2016.06.002> PMID: 27311755
59. P'ng C., Green J., Chong L.C., Waggott D., Prokopec S.D., Shamsi M., Nguyen F., Mak D.Y.F., Lam F., Albuquerque M.A., Wu Y., Jung E.H., Starmans M.H.W., Chan-Seng-Yue M.A., Yao C.Q., Liang B., Lalonde E., Haider S., Simone N.A., Sendorek D., Chu K.C., Moon N.C., Fox N.S., Grzadkowski M.R., Harding N.J., Fung C., Murdoch A.R., Houlahan K.E., Wang J., Garcia D.R., Borja R., Sun R.X., Lin X., Chen G.M., Lu A., Shiah Y., Zia A., Kearns R., Boutros P. BPG: Seamless, Automated and Interactive Visualization of Scientific Data. <https://doi.org/10.1186/s12859-019-2610-2> PMID: 30665349

4. CAPÍTULO 2

Capítulo descrito na forma de manuscrito (submetido).

Oxygen-induced pathological angiogenesis promotes intense lipid synthesis and remodeling in the retina

Abstract

The retina is a notable tissue with high metabolic needs which relies on specialized vascular networks to protect the neural retina while maintaining constant supplies of oxygen, nutrients and dietary essential fatty acids. Here we analyzed the lipidomic of the mouse retina under healthy and pathological angiogenesis using the oxygen-induced retinopathy model. By matching lipid profiles to changes in mRNA transcriptome, we identified a lipid signature showing that pathological angiogenesis leads to intense lipid remodeling favoring pathways for neutral lipid synthesis, cholesterol import/export and lipid droplet formation. Noteworthy, it also shows profound changes in pathways for long-chain fatty acids production, vital for retina homeostasis. The net result is accumulation of large quantities of mead acid, a marker of essential fatty acid deficiency, and a novel potential marker for retinopathy severity. Thus, our lipid signature might contribute to better understand diseases of the retina that lead to vision impairment or blindness.

Oxygen-induced pathological angiogenesis promotes intense lipid synthesis and remodeling in the retina

Alex Inague¹, Lilian Costa Alecrim¹, Jhonatas Sirino Monteiro, Marcos Yukio Yoshinaga, João Carlos Setubal, Sayuri Miyamoto*, Ricardo José Giordano^{2,*}

Biochemistry Department, Institute of Chemistry, University of Sao Paulo, Sao Paulo, SP, 05508-000, Brazil

¹These authors contributed equally and ²Lead contact

*Correspondence:

Ricardo José Giordano Telephone: +55 (11) 3091-1767 E-mail: giordano@iq.usp.br

Sayuri Miyamoto Telephone: +55 (11) 3091-9113 E-mail: miyamoto@iq.usp.br

Address: Av. Prof. Lineu Prestes, 748, São Paulo, SP. Postal code: 05508-000 Brazil.

1. Summary

The retina is a notable tissue with high metabolic needs which relies on specialized vascular networks to protect the neural retina while maintaining constant supplies of oxygen, nutrients and dietary essential fatty acids. Here we analyzed the lipidomic of the mouse retina under healthy and pathological angiogenesis using the oxygen-induced retinopathy model. By matching lipid profiles to changes in mRNA transcriptome, we identified a lipid signature showing that pathological angiogenesis leads to intense lipid remodeling favoring pathways for neutral lipid synthesis, cholesterol import/export and lipid droplet formation. Noteworthy, it also shows profound changes in pathways for long-chain fatty acids production, vital for retina homeostasis. The net result is accumulation of large quantities of mead acid, a marker of essential fatty acid deficiency, and a novel potential marker for retinopathy severity. Thus, our lipid signature might contribute to better understand diseases of the retina that lead to vision impairment or blindness.

Keywords: Oxygen-induced pathological angiogenesis, lipidomics, transcriptomics, lipid metabolism, neutral lipids, reverse cholesterol transport, lipid desaturation, n-9 fatty acid synthesis pathway.

2. Introduction

Lipid metabolism plays a central role in retina health and disease. For proper biological functioning, the retina depends upon a series of specialized dietary lipids, such as retinol and the highly unsaturated fatty acids (HUFA), docosahexaenoic (DHA, 22:6) and arachidonic acids (ARA, 20:4). And, similarly to tissues with high metabolic demands such as the heart and skeletal muscle, the retina also relies on glucose and fatty acid β -oxidation in order to supply the energetic needs of the highly demanding photoreceptor cells ¹. The vascular network is another notable feature of the retina which, as part of the central nervous system, is protected by specialized barriers: the outer and the inner-blood-retina barriers ². The latter provides nutrients and oxygen to the neural inner retina, while the former feeds the retinal-pigmented epithelial (RPE) layer, which protects the inner retina and nourishes the photoreceptor cells. Thus, it is not surprising that changes that affect retinal lipid metabolism and/or its delicate vascular network, have profound implications in tissue homeostasis and have been implicated as underlying mechanisms for many eye diseases ^{1,3-6}. Together, these diseases lead to different degrees of vision impairment and blindness, and affect people of all ages, from premature babies to adults with important impact in our society and the health system.

To better understand how changes in the vasculature of the eye affect retinal lipid metabolism and, therefore, retinal health, we studied a well-accepted animal model of retinal pathological angiogenesis using state-of-the-art lipidomic methods. The oxygen-induced retinopathy (OIR) mouse model reproduces many of the clinical features observed in premature babies suffering from retinopathy of prematurity (ROP), and to a lesser extent, diabetic retinopathy and other eye diseases ^{7,8}. For instance, the alterations in the vasculature induced by varying retinal oxygen levels in the OIR model causes the loss of astrocytes and microglia ⁹, reduce neuronal function of the photoreceptor cells (rods and cones) ¹⁰ and increase neuroinflammation ¹¹⁻¹³. Here we show that these changes are coupled with intense lipid remodeling in the whole retina. Not surprising, these changes affect cholesterol metabolism, which is essential for neuronal growth and survival since they need cholesterol to repair and build more membranes ^{14,15} as well as the metabolism of very long chain fatty acids, whose oxygenated derivatives (elovanoids) modulate the viability and function of photoreceptor cells and RPE undergoing uncompensated oxidative stress ^{16,17}.

Angiogenesis participates in several diseases, collectively known as angiogenesis-dependent diseases ¹⁸. Indeed, inhibitors of angiogenesis are already in the clinic and have been effective to treat patients with illnesses as dis-

parate as cancers and ophthalmic disorders, because they share in common the abnormal growth of new blood vessels (pathological angiogenesis). Thus, the OIR model is ideal to study not only retinopathy of prematurity, but human angiogenesis-dependent diseases as a whole ^{7,19}. Furthermore, the OIR model has many advantages to study pathological angiogenesis. It relays on isogenic animals (reducing genetic variability) and neovascularization is induced without direct manipulation of the retinas, which allows for good reproducibility while minimizing artifactual and undesired side effects (i.e., caused by the addition of exogenous recombinant growth factors or scaffolds necessary to induce angiogenesis in other mouse models). Additionally, in previous work, we performed a time course comparative transcriptomic analysis of the developmental (healthy) and diseased retinas (OIR model) to show that genes differentially expressed between the physiological and pathological conditions could be used as a new gene signature with high prognostic power for breast cancer, another angiogenesis-dependent disease ¹⁹. These data reinforce the notion that the retina and the OIR model are excellent tools to study human angiogenesis-dependent diseases.

Although the OIR model has been the subject of broad molecular characterization by transcriptomic ¹⁹⁻²³, proteomic ²⁴⁻²⁶, and metabolomic ²⁷ analyses, to the best of our knowledge, to date no detailed lipidomic study has been performed using this mouse model. Here, we performed a global time course lipidomic analysis of pathological (OIR) and healthy retinas. The lipidomic profile of the retinopathic and healthy retinas was then compared with their respective transcriptome to unveil molecular pathways and lipid metabolites that were affected by pathological angiogenesis. Given that angiogenesis is also a hallmark for two of the major eye diseases that lead to blindness, diabetic retinopathy and age-related macular degeneration, we trust this integrated analysis may provide valuable insights on lipid pathways that could be used as targets for future therapeutic approaches for retinopathy and other retinal diseases dependent on pathological angiogenesis.

3. Results

OIR promotes intense lipid remodeling in angiogenic retinas. To induce pathological angiogenesis in mice, we used the OIR model as previously described ^{19,28}. In brief, seven-day-old mice (postnatal day 7, P7) with their nursing mothers were submitted to 75% oxygen for 5 days. The high oxygen levels prevent physiological angiogenesis by inhibiting vascular endothelial growth factor (VEGF) production during a crucial time in retinal development (**Figure 1A**). When mice return to atmospheric oxygen levels, now on P12, the poorly vascularized retina experiences a strong hypoxic condition, which dramatically increases *Vegf* expression beyond physiolog-

ical levels. The net result is abnormal growth of blood vessels with the formation of neovascular tufts in the peripheral retina along with a central area of vaso-obliteration (**Figure 1B**). To compare the global lipid expression and remodeling in the retina under physiological and the OIR pathological angiogenesis, we performed advanced non-targeted high-resolution lipidomic analysis using retinas from normally developing and OIR mice.

We identified and quantified a total of 300 lipid species in both physiological (P) and pathological (R) conditions, which were distributed in 20 lipid classes belonging to five different categories: sphingolipids (SP), glycerophospholipids (GP), neutral lipids (NL), free fatty acids (FFA), and coenzyme Q (CoQ) (**Figure 1C**). Significant lipid remodeling was observed in physiological and pathological retinas with changes in 277 lipids (92% of total) (one-way ANOVA followed by Tukey's test, FDR-adjusted p -value < 0.05). Principal Component Analysis (PCA) showed that there was a good agreement in the lipid profile of our replicas and that changes in retinal lipidome occurs mainly according to time (Principal Component 1, PC1) and the condition of the retina (physiological or pathological) (PC2) (**Figure 1D**). In sum, the physiological development of newborn mice retinas promotes, by itself, changes in their lipid profile, which is further affected by retinopathy.

A more detailed analysis was carried out to highlight the main changes induced by retinopathy, or pathological angiogenesis. Lipid alterations are clearly visible during the peak of neovascularization, at postnatal days 15 and 17 (independent of the condition, OIR or physiological retinas). Considering the 50 most significantly altered lipid species, all samples could be correctly grouped according to their lipid composition in time and condition of the retina (**Figure 1E**). The notable exceptions were the OIR samples at postnatal days 12 and 12.5 (R12 and R12.5), which were all grouped together. This suggests that the first 12 hours of relative hypoxia do not induce major changes in retinal lipidome.

Interestingly, the most significantly altered lipid species correspond to neutral lipids, such as cholesteryl esters (CE) and triacylglycerols (TG), in addition to glycerophospholipids esterified to HUFA, for instance DHA (22:6) and ARA (20:4), and very long chain fatty acids (VLCFA) with more than 30 carbons (**Figure 1E**). Other main differences: (i) P12, R12 and R12.5 are specially enriched in phosphatidylcholine species linked to saturated and monounsaturated fatty acids (SFA and MUFA, respectively), besides CE molecular species. Concentrations of these species then decrease as time progresses, being especially low in the P17 group (physiological condition); (ii) in general, higher concentrations of TG are observed at days 15 and 17 (P15, R15, P17 and R17), and these

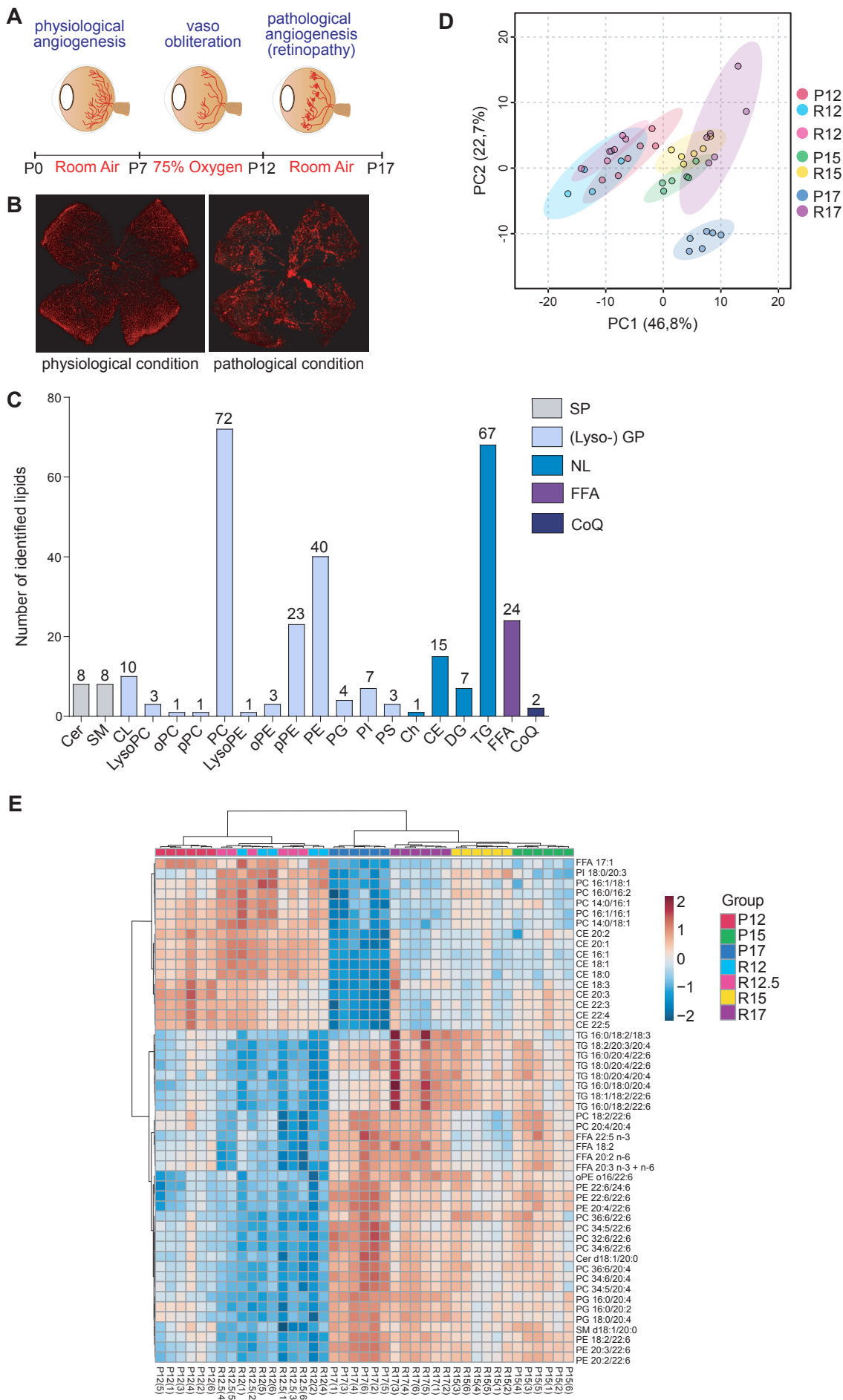


Figure 1. OIR promotes intense lipid remodeling in angiogenic retinas. **A.** Cartoon schematic of the OIR model. **B.** Healthy and OIR mice retinas showing central area vaso-obliteration and vascular tufts. **C.** Number of individual lipid molecular species and their respective lipid classes. **D.** Principal component analysis using the most abundant 300 lipid species. **E.** Heatmap of the top 50 significantly altered lipid molecular species (one-way ANOVA followed by Tukey's post-hoc analysis, FDR-adjusted p -value ≤ 0.05). Each horizontal row represents a molecular lipid; each vertical column represents a sample. Euclidean distance and Ward cluster algorithm were applied to build the heatmap. The colour code bar indicates the log of the fold change of the mean concentration for a given lipid. See also Figure S1.

Abbreviations for lipid categories. SP, sphingolipids; GP, glycerophospholipids; NL, neutral lipids; FFA, free fatty acids; CoQ, coenzyme Q. Lipid classes: Cer, ceramide; SM, sphingomyelin; CL, cardiolipin; LysoPC, lysophosphatidylcholine; PC, phosphatidylcholine; LysoPE, lysophosphatidylethanolamine; PE, phosphatidylethanolamine; PG, phosphatidylglycerol; PI, phosphatidylinositol; PS, phosphatidylserine; Ch, free cholesterol; CE, cholesteryl ester; DG, diacylglycerol; TG, triacylglycerol; FFA, free fatty acid; o- and p- before lipid class mean plasmanyl- and plasmeyl-phospholipids, respectively.

molecular lipid species are specially enriched in retinopathy (R17), particularly those linked to DHA and ARA. Finally, (iii) glycerophospholipids esterified to HUFA and VLCFA are enriched at postnatal days 15 and 17, the majority of them in the physiological condition (P15 and P17).

These findings were confirmed by pairwise comparisons (**Figure S1**). We observed that, at all postnatal days, the pathological condition induced a decrease in the concentration of phospholipids linked to HUFA, including phosphatidylcholines esterified to highly unsaturated VLCFA, with the exception of P15 versus R15, in which no significant change was observed for many of these lipid species (fold change ≥ 1.5 with FDR adjusted p -value ≤ 0.05). In OIR, decreased concentrations were also observed for TG species linked to polyunsaturated fatty acids (PUFA, with 2 or 3 unsaturations) and highly unsaturated fatty acids (HUFA, with more than 3 unsaturations) (P12 x R12; P12 x R12.5), in addition to poly- and highly unsaturated CE species (P12 x R12; P12 x R12.5; and P15 x R15). In contrast, a massive increase in the concentration of TG lipid species was detected at postnatal days 15 and mainly 17 in OIR retinas. A similar increase occurred to CE molecular species in OIR retinas at postnatal day 17 (P17 x R17).

Substantial increase in neutral lipid concentration is linked to the formation of lipid droplets and occurrence of reverse cholesterol transport in pathological retinas. OIR clearly drives a substantial increase in total neutral lipid levels, particularly total CE at postnatal day 17, and total TG at postnatal days 15 and 17 (**Figure 2A**). All 15 CE molecular species were increased in the pathological condition at postnatal day 17 (R17 group), regardless of the degree of unsaturation (**Figure 2B**). Of these 15 species, 14 were significantly augmented in pathological retinas when compared to healthy retinas (fold change ≥ 1.5 , FDR adjusted p -value ≤ 0.05) (**Figure 2C**). The same pattern of increased concentration in retinopathy was observed for all 67 TG species at postnatal day 17 (**Figure S2A**). In total, 55 TG species had significant increased concentrations due to the disease, regardless of the degree of unsaturation (**Figure S2B**).

Integration of lipidomic with transcriptomic data allowed to better delineate the neutral lipid synthesis pathways that are altered in OIR (**Figure 2D** and **2E**). For the lipidomic-transcriptomic comparison analyses, we employed two criteria: (a) key regulatory genes whose expression levels were significantly changed, considering $\log_2(\text{fold change}) > 1.5$ or $\log_2(\text{fold change}) < 0.5$, and p -value < 0.05 ; these individual genes are cited in the text and figures. We also considered another situation (b), when the overall expression (regardless of the fold change value)

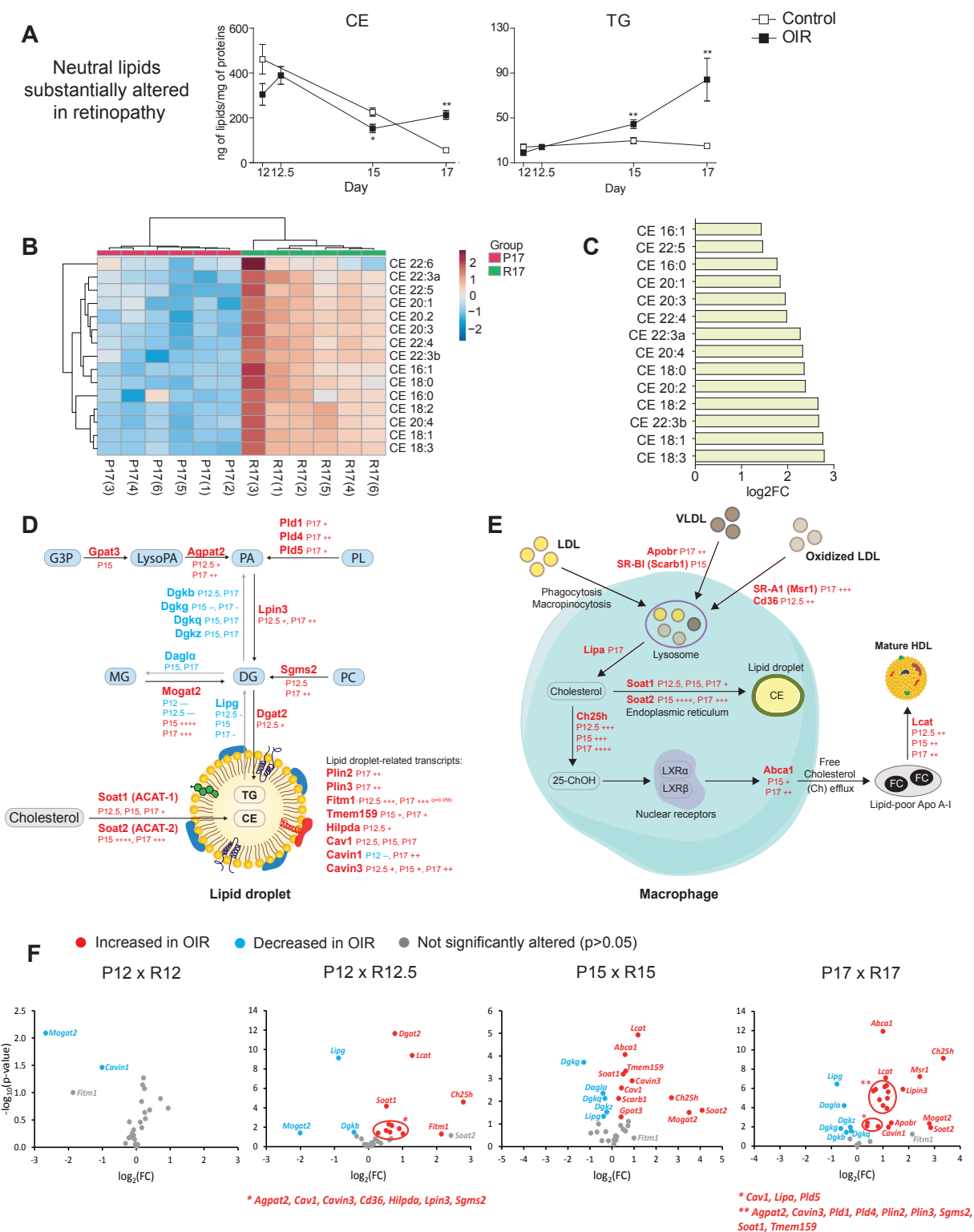


Figure 2. Increased neutral lipid synthesis and lipid droplets formation in pathological retinas. **A.** Normalized mass values (ng of lipids/mg of proteins) for neutral lipid classes in control and OIR retinas. Data are represented as mean \pm SEM (Mann-Whitney-Wilcoxon test, $*p \leq 0.05$, $**p \leq 0.01$, $***p \leq 0.001$). **B.** Heatmap with all 15 CE lipid species at postnatal day 17. The color code bar indicates the log of the fold change of the mean concentration for each given CE. **C.** Pairwise comparisons of CE mass alterations promoted by OIR at postnatal day 17. X-axis corresponds to log₂(fold change) observed for each CE lipid species. Fold change was set to ≥ 1.5 ; FDR adjusted p -value ≤ 0.05 was used for significance. **D.** Schematic showing the synthesis pathways of TG and CE, neutral lipids stored in lipid droplets. **E.** Schematic showing the formation of CE in the extracellular medium, after efflux of cholesterol and action of LCAT in (apo)lipoproteins. In both diagrams, genes that are differentially expressed (p -value ≤ 0.05) in pathological retinas are highlighted in red (increased expression) or blue (decreased expression) colors. Legend: (+ or -) $0.6 \leq \log_2(\text{fold change}) < 1.0$; (++) $1.0 \leq \log_2(\text{fold change}) < 2.0$; (+++) $2.0 \leq \log_2(\text{fold change}) < 3.0$; (++++) $3.0 \leq \log_2(\text{fold change})$. **F.** Volcano plots with genes whose expression is increased (red) or decreased (blue) in OIR at postnatal days 12, 12.5, 15 and 17. Only genes mentioned in Figure 2D and 2E are shown. See also Figure S2 and Transcriptomics Spreadsheet.

Abbreviations. G3P, glycerol 3-phosphate; LysoPA, lysophosphatidic acid; PA, phosphatidic acid; PL, phospholipid; MG, monoacylglycerol; LXR, liver X receptor.

of multiple genes in a given pathway was significantly altered (p -value < 0.05) in retinopathy (**Transcriptomics Spreadsheet**) (**Figure 2D, 2E and 2F**). These altered pathways are indicated in the text and figures as well.

Glycerol-3-phosphate acyltransferase 3 (*Gpat3*), which converts glycerol-3-phosphate (G3P) to lysophosphatidic acid (LysoPA), is increased in OIR retinas at P15. Increases were also observed for 1-acylglycerol-3-phosphate O-acyltransferase 2 (*Agpat2*) and phospholipase D1 (*Pld1*); both lead to the production of phosphatidic acid (PA). Interestingly, phospholipase D family members 4 (*Pld4*) and 5 (*Pld5*) are also increased in the disease, although no phospholipase activity has been demonstrated for these isoenzymes^{29,30} (**Figure 2D**).

Next, different diacylglycerol (DG)-producing pathways were considerably up-regulated in the pathological condition: a) from PA to DG, through the catalysis by lipin 3 (*Lpin3*). The reverse reaction even seems down-regulated, since a series of diacylglycerol kinases (*Dgkb*, *Dgkg*, *Dgkq* and *Dgkz*) are moderately reduced in the disease; b) from monoacylglycerol (MG) to DG, with a strong increase in monoacylglycerol O-acyltransferase 2 (*Mogat2*) gene expression at postnatal days 15 and 17, and a slight decrease in diacylglycerol lipase alpha (*Dagla*) expression at the same times; c) from phosphatidylcholine (PC), through the action of sphingomyelin synthase 2 (*Sgms2*), leading to the formation of sphingomyelin (SM), and of DG as by-product (**Figure 2D**).

In the final step, DG is converted to TG through catalysis by diacylglycerol acyltransferase (DGAT) enzymes. Both *Dgat1* and *Dgat2* mRNAs were present and quantified in normal and OIR retinas, although only the expression of *Dgat2* was slightly increased at postnatal day 12.5. Endothelial lipase (*Lipg*), which can act as a TG lipase, was significantly reduced in retinopathy, corroborating the TG accumulation observed in the lipidomic data. In addition to TG molecular species, the detected increase in CE may be linked to higher expression of the genes sterol O-acyltransferase 1 (*Soat1*) and especially sterol O-acyltransferase 2 (*Soat2*), the latter showing high fold change values in the pathological retinas at postnatal days 15 and 17. Indeed, molecular species of TG and CE are stored intracellularly in lipid droplets, and a number of structural markers of lipid droplets presented increased gene expression in retinopathy, including: perilipin 2 (*Plin2*), perilipin 3 (*Plin3*), fat storage-inducing transmembrane protein 1 (*Fitm1*), transmembrane protein 159 (*Tmem159/Ldaf1*), hypoxia inducible lipid droplet associated (*Hilpda*), caveolin 1, caveolae protein (*Cav1*), caveolae associated 1 (*Cavin1*) and caveolae associated 3 (*Cavin3*) (**Figure 2D**). Collectively, the transcriptomic and lipidomic data suggest that lipid-droplet production in the retina is substantially augmented in the pathological retina.

Transcriptomic analysis also showed that cholesterol import/export through the high-density lipoprotein (HDL) pathway is activated. The expression of the lecithin cholesterol acyltransferase (*Lcat*) gene is considerably increased in retinopathy at postnatal days 12.5, 15 and 17 (\log_2 fold change = 1.28, 1.17 and 1.10, respectively), pointing to an increase in the production/maturation of HDL (**Figure 2E**). The LCAT enzyme esterifies free cholesterol (Ch) on nascent lipoproteins that mediate intraretinal cholesterol transport^{31,32}. In pre- β -HDL, LCAT catalyses esterification and production of CE, leading to the formation of mature spherical HDL particles³³. Major protein components of HDL³⁴ are also up-regulated in retinopathy according to expression data for the following genes: *Lcat*, alpha-2-macroglobulin (*A2m*), amylase 1 (*Amy1*), complement component 3 (*C3*), complement component 4B (*C4b*), clusterin (*Clu*), glutathione peroxidase 3 (*Gpx3*), granulins (*Grn*), hemopexin (*Hpx*), paraoxonase 1 (*Pon1*), paraoxonase 3 (*Pon3*), retinol binding protein 1 (*Rbp1*) and 4 (*Rbp4*), transferrin (*Trf*), transthyretin (*Ttr*), and wingless-type MMTV integration site family members (*Wnt*), including member 2 (*Wnt2*), 5A (*Wnt5a*), 9A (*Wnt9a*), 11 (*Wnt11*) and 16 (*Wnt16*) (**Transcriptomics Spreadsheet**). These data are also in agreement with the overall increase in the expression of other genes related to cholesterol import/export into cells, such as apolipoprotein B receptor (*ApoB*), scavenger receptor class B, member 1 (*Scarb1/SR-B1*), macrophage scavenger receptor 1 (*Msr1/SR-A1*) and CD36 molecule (*Cd36*). These indicated receptors, in addition to low-density lipoprotein (LDL) ingestion via phagocytosis and macropinocytosis, are essential for lipoprotein internalization. Lipoproteins are then degraded in lysosomes, releasing cholesterol into the intracellular environment (**Figure 2E**).

Cholesterol metabolism also relies on a series of esterases to produce more soluble metabolites which are, therefore, easier to be eliminated. So, it is worth noting the unusual high expression of cholesterol 25-hydroxylase (*Ch25h*) in retinopathy (\log_2 fold change = 2.78, 2.70 and 3.35 at postnatal days 12.5, 15 and 17, respectively). Ch25h catalyses the formation of 25-hydroxycholesterol (25-ChOH), an agonist of nuclear receptors liver X receptors (LXRs)^{35,36}. LXRs regulate gene expression of ATP-binding cassette sub-family A member 1 (*Abca1*), which increased in OIR retinas at postnatal days 15 and 17, and promotes cholesterol efflux from cells *via* lipid-poor apoA-I (pre- β -HDL)³⁷ (**Figure 2E**). Interestingly, 25-ChOH also restricts activation of SREBP2, a sterol-sensing transcription factor that regulates cholesterol biosynthesis³⁸. This is in agreement with expression data of 23 genes whose products belong to the cholesterol biosynthesis pathway³⁹ and which are down-regulated in retinopathy (**Transcriptomics Spreadsheet**).

Lipid saturation degree is markedly altered by OIR towards the production of MUFA and PUFA with up to 3 unsaturations. Total SFA, MUFA, PUFA and HUFA (examples in **Figure 3A**) were quantified considering all detected lipid classes in lipidomic analysis. In our analysis, we considered PUFA all fatty acids with two or three unsaturations, and HUFA all those with more than three unsaturations, including, for instance, DHA and ARA. In general, OIR retinas showed an increase in MUFA concentrations compared to healthy retinas at postnatal days 12, 12.5 and 17 (**Figure 3B**). In contrast, PUFA concentration was decreased at P12.5, but subsequently recovered at P15 and increased at P17, while HUFA concentration was generally decreased in OIR retinas at all different time points.

When we consider the lipid classes that are mostly enriched with HUFA – cholesteryl esters (CE), phosphatidylethanolamines (PE), PE plasmalogens (pPE) and phosphatidylinositols (PI) – in addition to triacylglycerols (TG), this pattern is even more apparent (**Figure 3C**). All these lipid classes showed higher concentrations of MUFA and lower concentrations of HUFA in OIR. In terms of fatty acids with two or three unsaturations, CE and TG molecular species linked to PUFA showed a tendency to increase in retinopathy, and a similar trend was observed for PE and PI.

Next, we used the Venn diagram to screen for common lipid features associated with OIR (fold change ≥ 1.5 , FDR adjusted p -value ≤ 0.05) (**Figure S3A**). Among the five lipid species that were found altered at all postnatal days, four species - FFA 20:3 (n-9), PI 18:0/20:3, PC 16:0/22:3 e CE 20:3 – were increased in OIR, while only one of them, specifically a plasmalogen esterified to HUFA (pPE p18:2/22:6), was decreased. Notably, in agreement with the unsaturation data, all increased lipid species were linked to fatty acyl chains containing three double bonds (20:3 or 22:3) (**Figure S3B**).

The concentration of phosphatidylcholines (PC) linked to VLCFA is decreased in OIR retinas. Very long chain highly unsaturated fatty acids (VLC-HUFA) are found mainly in retina, brain, testis and spermatozoa ⁴⁰. We identified and quantified 15 PC lipid species esterified to VLC-HUFA with at least 32 carbons of length in all collected samples. Among these phospholipids, PC (34:6/22:6) and PC (36:6/22:6) were the most abundant in retinas, with the VLC-HUFA esterified to the sn-1 position of the glycerol-phosphocholine backbone (**Figure 4A**). No VLC-HUFA bound to other types of phospholipids were identified; all of them are linked to PC. Retinopathy drove a significant decrease in total mass values of these PC species, which is seen at postnatal days 12, 12.5 and 17 (**Figure 4B**). The same trend is clearly seen in 11 of the 15 individual species of PC linked to VLC-HUFA that we could identify in lipidomic analysis (**Figure 4C**).

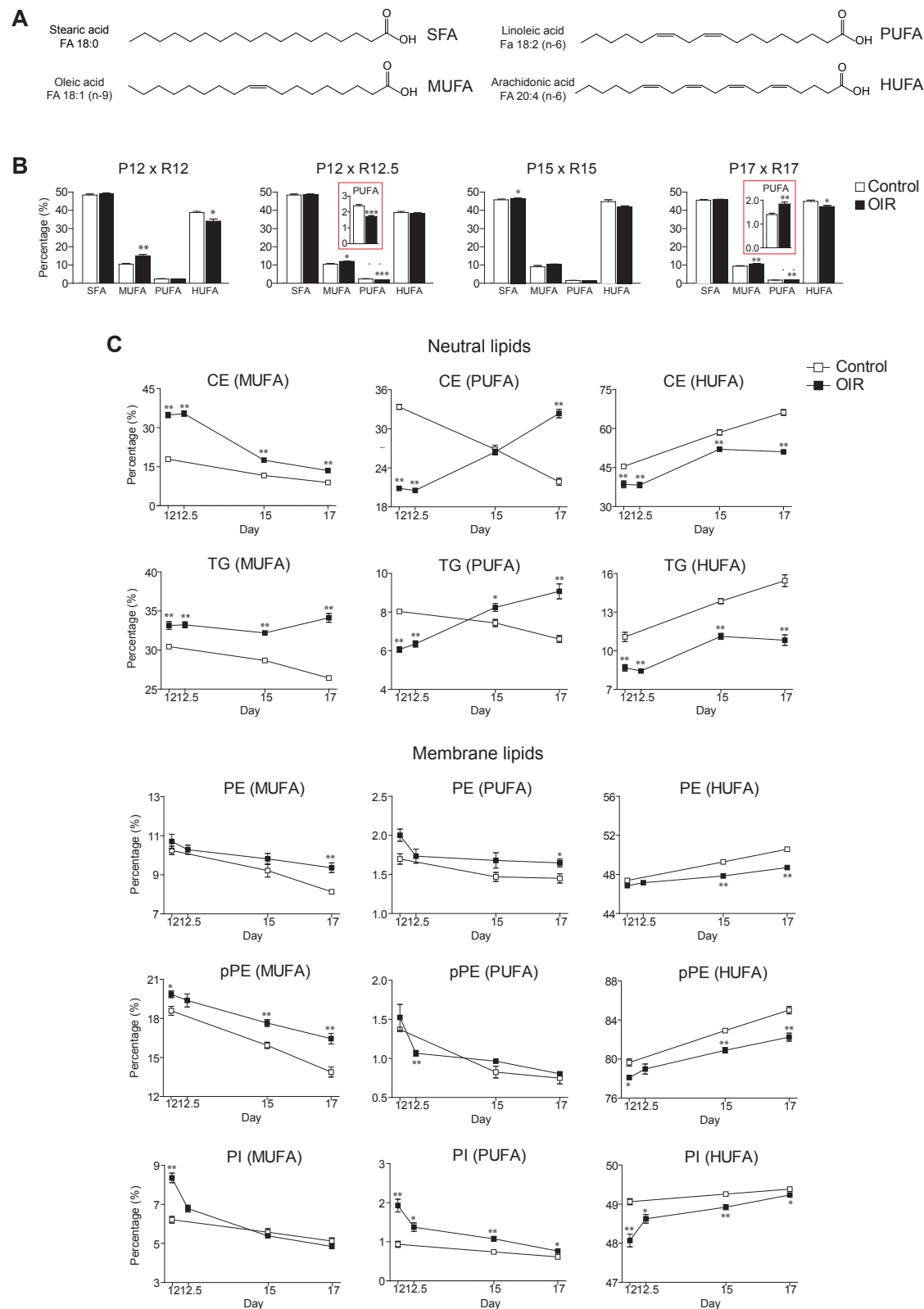


Figure 3. Lipid saturation is altered in OIR favoring the production of MUFA and PUFA with up to 3 unsaturations. **A.** Examples of SFA, MUFA, PUFA and HUFA found in OIR retinas. **B.** Percentage of SFA, MUFA, PUFA and HUFA in physiological (controls, N=6) and pathological (OIR, N=6) retinas at postnatal days 12, 12.5, 15 and 17. Data are represented as mean \pm SEM (Student's t-test, * $p \leq 0.05$, ** $p \leq 0.01$, *** $p \leq 0.001$). **C.** Percentage of MUFA, PUFA and HUFA in specific lipid classes, including neutral (CE and TG) and membrane (PE, pPE and PI) lipid species. Data are represented as mean \pm SEM (Mann-Whitney-Wilcoxon test; * $p \leq 0.05$, ** $p \leq 0.01$, *** $p \leq 0.001$). See also Figure S3 and Supplemental Material - Venn diagram.

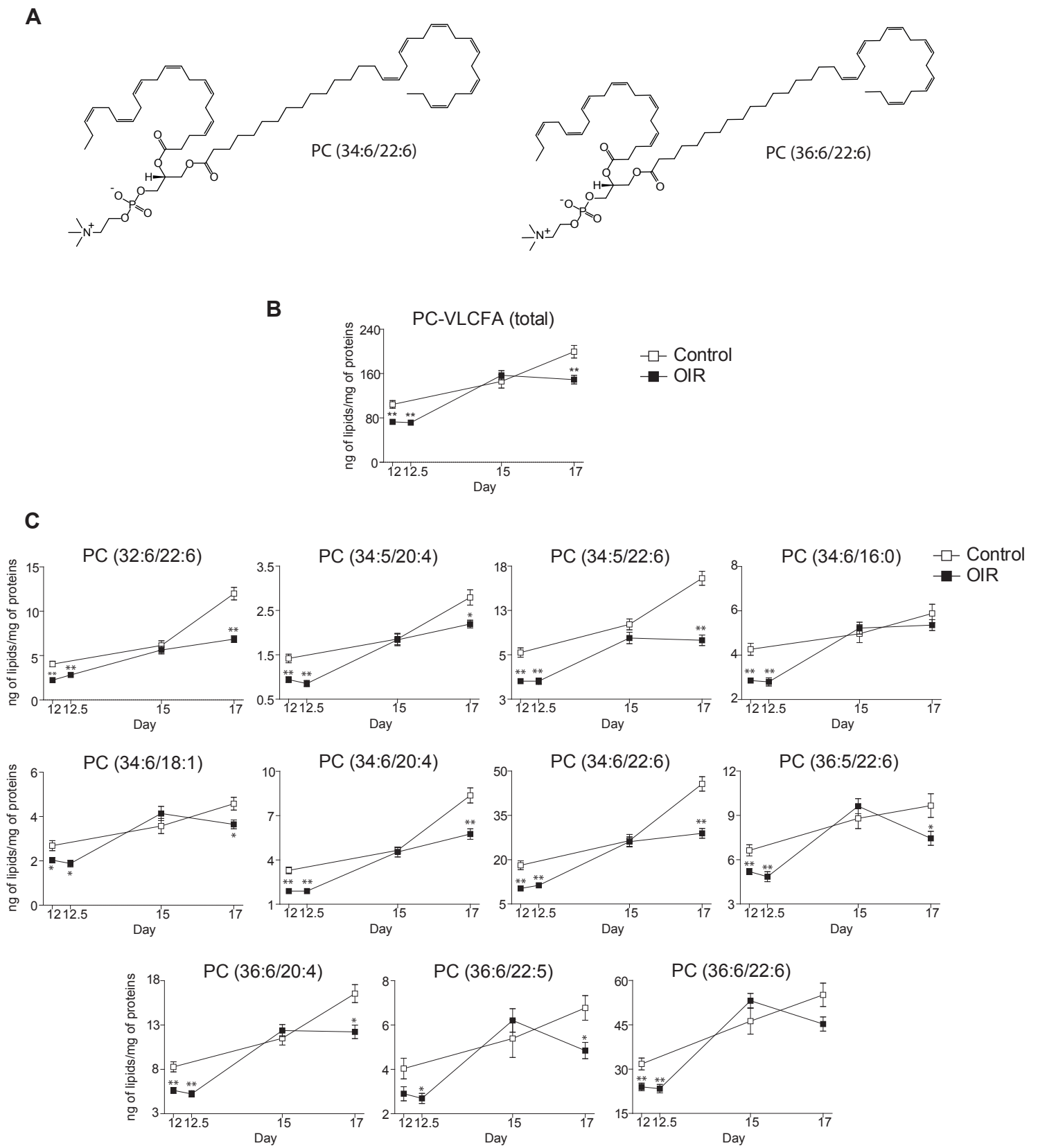


Figure 4. *Phosphatidylcholines (PC) linked to VLCFA in OIR retinas.* **A.** Representative structures of the two most abundant PC-VLCFA found in normal and OIR retinas. **B.** Normalized mass values (ng of lipids/mg of proteins) for total PC-VLCFA. **C.** Normalized mass values (ng of lipids/mg of proteins) for individual PC-VLCFA species. PC-VLCFA species were identified and quantified in all physiological (control, N=6 replicates) and pathological (OIR, N=6 replicates) retinas collected at postnatal days 12, 12.5, 15 and 17. Only PC species linked to at least one fatty acid with 32 or more carbons were considered. Data are represented as mean \pm SEM (Mann-Whitney-Wilcoxon test; * $p \leq 0.05$, ** $p \leq 0.01$, *** $p \leq 0.001$).

OIR retinas present decreased synthesis of n-3 and n-6 fatty acids and up-regulation of the n-9 alternative pathway of fatty acid desaturation. The pattern of decreased HUFA, such as DHA (22:6, n-3) and ARA (20:4, n-6), as well as VLC-HUFA (n-3 or n-6), led us to investigate how different fatty acid synthesis pathways behave in retinopathy. Both the n-3 (or ω -3) and n-6 (or ω -6) fatty acid pathways comprise a series of products derived biosynthetically from essential fatty acids, ingested in the diet. In our lipidomic analysis, we were able to differentiate specific FFA isomers through their retention time in the column used in high-performance liquid chromatography (HPLC). These isomers present the same molecular mass, but different positions of double bonds, i.e., different “n” values. In general, considering two isomers, the FFA with a higher “n” value had a longer retention time in our method (**Figure S4A**). This is shown in detail for FFA 20:3, whose *m/z* value generated two peaks in our analysis, one corresponding to FFA 20:3 n-3 and n-6, and the other to FFA 20:3 n-9, the latter with a longer retention time (**Figure S4B**).

Derived from the α -linolenic acid (18:3, n-3), n-3 family includes fatty acids such as eicosapentaenoic acid (EPA, 20:5, n-3), docosapentaenoic acid (DPA, 22:5, n-3) and DHA (22:6, n-3). All of them are significantly decreased in retinopathy (**Figure 5A**). Similarly, the n-6 family of fatty acids, derived from linoleic acid (18:2, n-6), also shows up in lower concentrations in OIR retinas. This is clearly seen for several intermediates of the n-6 pathway, including eicosadienoic acid (20:2, n-6), dihomo- γ -linolenic acid (DGLA, 20:3, n-6), ARA (20:4, n-6) and adrenic acid (AdA, 22:4, n-6) (**Figure 5B**). This indicates a chronic deficiency of n-3 and n-6 precursor from the early stages of the retinopathic process affecting the synthesis of all subsequent derived long chain fatty acids. Indeed, the n-3 and n-6 synthesis pathways are the precursors of VLC-HUFA. Their down-regulation helps to explain, for example, the decreased concentration of phosphatidylcholine species linked to VLC-HUFA in the pathological condition (**Figure 4**). This also explains the overall decrease in the number of unsaturations in most of the lipid classes analyzed in this study (**Figure 3**).

On the other hand, as seen earlier, retinopathy induces increased concentration of MUFA and PUFA with up to 3 unsaturations. This finding correlates with up-regulation of *de novo* fatty acid synthesis, generating products with 1, 2 or 3 unsaturations. In a situation of essential fatty acid deficiency (EFAD), there is possibly an accumulation of MUFA and PUFA belonging to families other than n-3 and n-6. This includes, for example, the n-9 (or ω -9) family. We were able to detect and quantify four products from the n-9 fatty acid family: eicosenoic acid (20:1, n-9), eicosadienoic acid (20:2, n-9), mead acid (20:3, n-9) and docosatrienoic acid (22:3, n-9), all of them showing an increasing trend in the OIR retinas (**Figure 5C**).

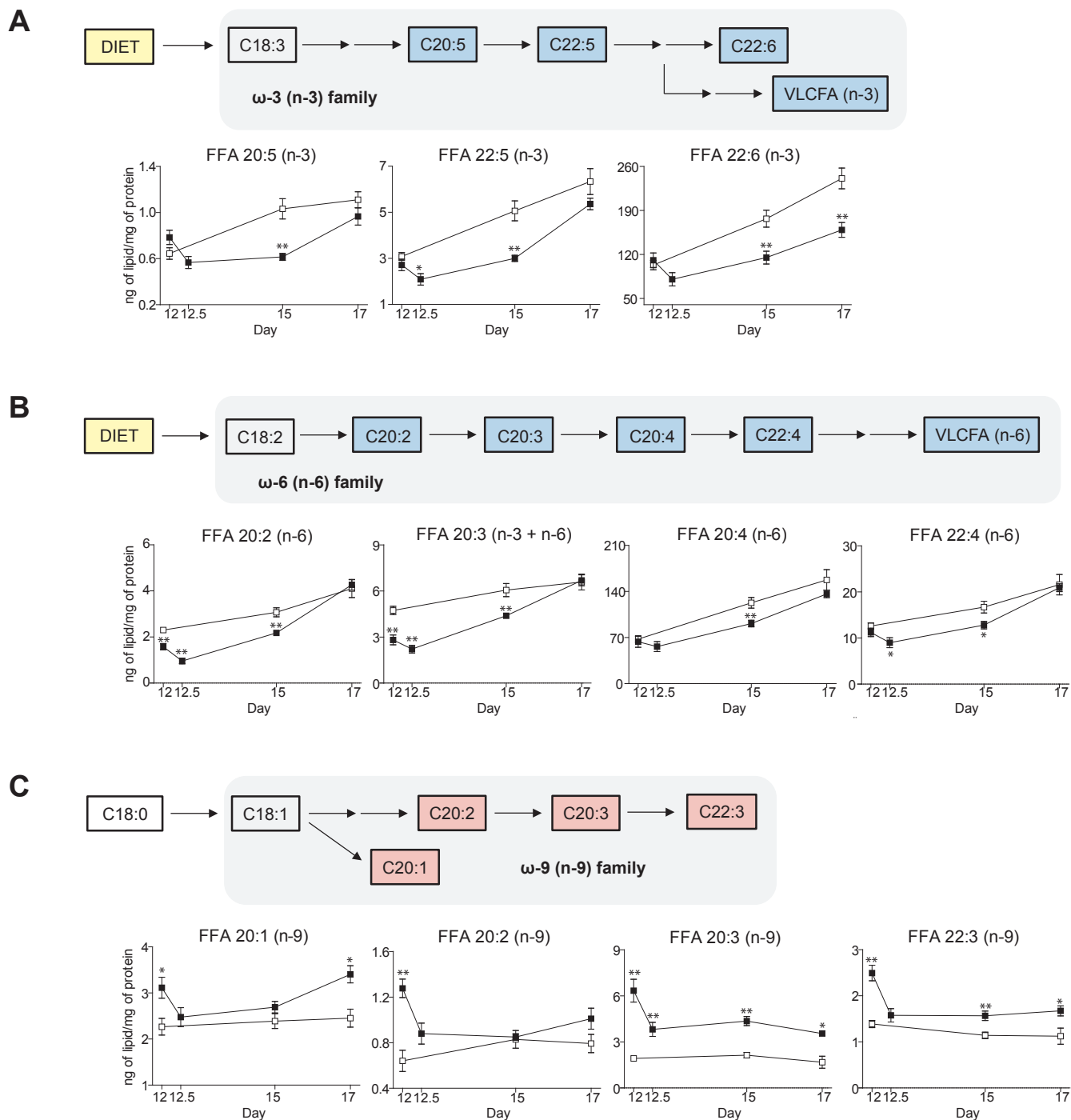


Figure 5. OIR retinas decreased synthesis of *n*-3 and *n*-6 fatty acids and up-regulation of the *n*-9 alternative pathway of fatty acid desaturation. Schemes showing intermediates of the *n*-3 (A), *n*-6 (B) and *n*-9 (C) fatty acid synthesis pathways which are significantly altered in the retinas of OIR mice. Normalized mass values (ng of lipids/mg of proteins) are presented for each of these intermediates in physiological (control, N=6 replicates) and pathological (OIR, N=6 replicates) retinas at postnatal days 12, 12.5, 15 and 17. Data are represented as mean \pm SEM (Mann-Whitney-Wilcoxon test; * $p \leq 0.05$, ** $p \leq 0.01$, *** $p \leq 0.001$). See also Figure S4.

4. Discussion

By carefully identifying and quantifying the lipid composition of the retina and mapping them to their respective metabolic pathways (for which we had information regarding mRNA expression for their enzymes and proteins), we have identified a lipid signature for the pathological angiogenesis of the OIR model. This signature points to a prominent role for cholesterol esterification, lipid droplet formation, reverse cholesterol transport, and increased n-9 fatty acid synthesis (for example, mead acid) in the retina.

At first glance, the most striking result is the increase in the concentration of neutral lipids (mostly CE and TG species) in the retinopathic retinas. In agreement with the lipidomics, transcriptomic data indicate TG formation, since the pathways leading to its synthesis are in general significantly augmented. The same is observed for the expression of genes leading to CE synthesis (*Soat1* and, particularly, *Soat2*), as well as structural proteins for lipid droplet production (*Plin2*, *Plin3*, *Fitm1*, *Tmem159/Ldaf1*, *Hilpda*, *Cav1*, *Cavin1*, *Cavin3*). Lipid droplets are important organelles for fat storage, which are composed mainly of CE and TG within their lipid core, enclosed by a monolayer of phospholipids and proteins. This is in agreement with the recent observation that the retina relies on a steady supply of fatty acids in order to provide the energetic needs of the photoreceptor cells. These cells express high levels of the very low-density lipoprotein (VLDL) receptor, enabling the uptake of TG to be metabolized by β -oxidation ¹.

But the role of lipid droplets in the retina is still not fully understood. For instance, reactive oxygen species (ROS) production is increased in the OIR model and in retinopathies in general, as well as in many other eye diseases ^{41,42}. So, besides the role of lipid droplets in energy storage, they may also act to buffer the concentration of toxic lipid species ⁴³ and have a prominent role in limiting the levels of ROS in cells by capturing PUFA from cellular membranes and thus preventing lipid peroxidation ⁴⁴. Another interesting observation is that RPE cells contain organelles named retinosomes, which are retinyl ester-containing lipid droplets important to keep a proper supply of the visual chromophore 11-cis-retinal to the photoreceptor cells ⁴⁵. Changes in the formation of these lipid droplets (retinosomes) have been associated with pathological conditions in the retina of drosophila and rat ^{46,47}, in addition to patients suffering from age-related macular degeneration (AMD) ⁴⁸. Although in our lipidomic analysis we did not look specifically at retinyl esters, it is noteworthy the increase in expression of lecithin-retinol acyltransferase (*Lrat*), which encodes the enzyme responsible for the esterification of trans-retinal, producing trans-retinyl esters. *Lrat* is substantially augmented in retinopathic retinas (\log_2 fold change = 2.24 at postnatal day 17, compared to

the physiological condition).

Alongside *Lrat*, and *Soat1* and *Soat2*, which are responsible for the intracellular esterification of lipids stored in lipid droplets, we also observed in OIR a significant increase in gene expression of *Lcat* (\log_2 fold change = 1.28, 1.17 and 1.11 at postnatal days 12.5, 15 and 17, respectively). The LCAT enzyme is responsible for the production of extracellular CE, converting cholesterol and phosphatidylcholines to CE and lysophosphatidylcholine (LysoPC). LCAT has a defined role in the growth and maturation of HDL particles³³ and cholesterol efflux from macrophages via ABCA1. LCAT deficiency is characterized by two different phenotypes with distinct levels of LCAT activity: familial LCAT deficiency (FLD) and fish eye disease (FED), both leading to low HDL cholesterol levels and corneal opacification⁴⁹. This is also in agreement with our lipid signature, which shows a prominent role of the cholesterol import/export pathway in retinopathy.

The retina differs from the central nervous system with regard to cholesterol metabolism, a key factor in retinal pathological conditions as mentioned above. While the brain synthesizes all cholesterol it uses, the retina can both synthesize it and uptake cholesterol from circulation^{14,15}. Thus, it is interesting that under retinopathic condition, several genes associated with cholesterol esterification and transport (*Soat1*, *Soat2*, *Lcat*, *Abca1*, besides lipoprotein receptors such as *Apobpr*, *Scarb1*, *Msr1* and *Cd36*) are up-regulated, indicating an increase in the import/export of cholesterol (i.e., from circulation to the RPE, then, from the RPE to the photoreceptor cells and the neural retina). At the same time, 23 genes related to cholesterol biosynthesis are reasonably decreased in OIR (**Transcriptomics Spreadsheet**), suggesting that intraretinal cholesterol synthesis is not the main factor behind the increase in CE levels.

One limitation of our study, however, is that we cannot discriminate which cell is responsible for CE synthesis and export, such as glial or tissue macrophages. Considering that large epidemiologic studies point to a strong correlation between circulating lipoprotein species, such as HDL, and the severity of retinopathy and other eye diseases, one cannot rule out the contribution of infiltrating macrophages as the source of accumulation of cholesterol in the retina. In this context, lipid-lowering treatments with statin and fibrate have been shown to improve diabetic retinopathy-related conditions⁵⁰⁻⁵². Similarly to what occurs in atherosclerosis, we observed that key pathways for reverse cholesterol transport showed significant increased expression in OIR retinas, as well as multiple markers for tissue macrophages (*Itgam/Cd11b*, *Cd14*, *Fcgr3/Cd16*, *Fcgr1/Cd64*, *Cd68*, *Ccr5*, *Adgre1*) and glial macro-

phages (*Trem2*, *Tyrobp*, *Cd33*, *Tlr1*, *Tlr2*, *Tlr3*, *Tlr4*, *Tlr7*, *Tlr12*, *Tlr13*), in addition to markers for HDL particles (*A2m*, *Amy1*, *C3*, *C4b*, *Clu*, *Gpx3*, *Grn*, *Hpx*, *Lcat*, *Pon1*, *Pon3*, *Rbp1*, *Rbp4*, *Trf*, *Ttr*, *Wnt2*, *Wnt5a*, *Wnt9a*, *Wnt11*, *Wnt16*). Therefore, new potential targets for drugs are provided, in particular those directed to neutral lipid (CE and TG) synthesis pathways, reverse cholesterol transport and the inflammatory status of pathological retinas.

For instance, *Ch25h* expression is also substantially increased by OIR¹⁹. CH25H catalyzes the conversion of cholesterol to 25-hydroxycholesterol (25-ChOH), a product which can act as activator of LXR receptors and then also promote cholesterol efflux to (apo)lipoproteins via ABCA1. CH25H was previously shown to contribute to a pathological angiogenesis gene signature able to predict breast cancer patient survival¹⁹. Besides being a LXR activator, its product, 25-ChOH, presents anticancer⁵³ and antiviral⁵⁴ activities in mammalian cells, working against viruses such as HIV, EboV, Influenza and others by affecting their entry and replication in the cell. The role of CH25H and 25-ChOH in retinopathy and other eye disease is still unknown.

In addition to neutral lipid increase and aspects related to the ‘inflammatory environment’ of OIR retinas, we detected changes in lipid desaturation pathways as another hallmark of pathological angiogenesis. OIR retinas present high concentrations of MUFA and PUFA with up to three unsaturations. Nevertheless, n-3 and n-6 HUFA species (with more than three unsaturations) were considerably decreased in the pathological condition. The same happened to phosphatidylcholine molecular species linked to VLC-HUFA, unusual lipid species found in retina and a few other vertebrate tissues, such as brain and testis. In retinas, they seem to play a crucial role in maintaining membrane fluidity, which is essential to the long-term survival and function of photoreceptor outer segments^{55,56}. In AMD and diabetic donor eyes, for instance, there is a significant decrease in the concentration of these long-chain and highly unsaturated lipid species^{40,57,58}.

The sharp decrease in highly unsaturated species led us to investigate different pathways of fatty acid synthesis in healthy and OIR retinas. The decrease in n-3 and n-6 FFA, for example EPA, DPA and DHA (n-3 family) and eicosadienoic acid, DGLA, ARA e AdA (n-6 family), are in agreement with previously published data showing that premature infants have lower blood concentrations of DHA and ARA, a condition of essential fatty acid deficiency (EFAD) that correlates with ROP progression⁵⁹⁻⁶². EFAD is tightly associated to changes in lipid desaturation profiles and the promotion of alternative fatty acid desaturation pathways, which in turn affects, for instance, the fatty acid profile of cells in culture, augmenting the concentration of MUFA instead of PUFA/HUFA⁶³. Lipid

metabolism plasticity is also observed in some cancer cell lines. Some of them exploit an unusual pathway that desaturates palmitate to sapienate, a monounsaturated fatty acid of the n-10 family that supports membrane formation and proliferation ⁶⁴.

It is noteworthy that the deficiency in n-3 and n-6 essential fatty acids in the OIR retinas promotes an alternative lipid synthesis pathway that leads to the production of n-9 fatty acids, such as mead acid (20:3, n-9). Mead acid is an indicator of EFAD ⁶⁵ and, interestingly, it is substantially increased at all postnatal days in the pathological condition but not in the physiological retinas. To the best of our knowledge, this has not been reported before and it is a clear indication that EFAD might be an early event in ROP. Indeed, postnatal n-3 and n-6 serum levels have been associated with ROP and its severity ⁶⁶. Hence, our data is in agreement with the notion that n-3 and n-6 essential fatty acids supplementation might be beneficial for prevention of ROP. Nevertheless, several clinical studies failed to confirm positive effects of lipid supplementation on ROP outcome ^{67,68}. One possible explanation for this conundrum is that the activation of *de novo* fatty acid synthesis via the n-9 fatty acid synthesis pathway could hinder the effects of lipid supplementation by outcompeting with the dietary n-3 and n-6 essential fatty acids. Corroborating this idea is the fact that mead acid may be used as a substitute for other PUFA and HUFA in biological membranes ⁶⁵. Indeed, mead acid production could explain the increase in PUFA with three unsaturations observed in retinopathy. In general, the desaturation profile in the lipidomic data suggest that HUFA are being replaced by mono- and polyunsaturated fatty acids (MUFA and PUFA, respectively) with up to three unsaturations in pathological angiogenesis, which reflects *de novo* fatty acid synthesis via the n-9 fatty acid synthesis pathway. Finally, considering that mead acid concentration in blood could be used to identify patients with EFAD, conceivably, it could also be a potential biomarker for ROP. Further studies are necessary to answer these questions regarding mead acid, and n-3 and n-6 supplementation in ROP.

In sum, these are important findings, which might have implications for the diagnosis, treatment and prevention of ROP, a condition for which the OIR mouse model recapitulates several hallmarks of the human diseases ⁸. Changes in lipid metabolism have also been described for diabetic retinopathy ^{50-52,69}, glaucoma ⁷⁰ and age related macular degeneration ^{71,72}. Therefore, it is possible that our integrated lipidomic/transcriptomic study may reflect changes in lipid metabolism associated with different eye diseases. A better understanding of lipid metabolism in the retina may translate into novel and improved therapeutic and diagnostic alternatives for the treatment and prevention of many eye diseases.

5. Limitations of the study

The OIR model is a robust and reliable method to study retinal angiogenesis *in vivo*, and the use of isogenic animals minimizes genetic background variability and allows for reproducible and quantifiable results. Nevertheless, exposure to high oxygen levels (75%) can be detrimental to the animals, reducing postnatal weight gain and aggravating the retinopathic state. To minimize these effects and reduce vessel loss and variability in neovascularization, we avoided large litter sizes (8 or less pups) to improve postnatal weight gain, and animals with less than 5 grams at P17 were excluded from the study, as recommended^{73,74}. Another aspect that merits comments is the difficulty in assigning specific lipid synthesis pathways and transcript expression to precise cells in the retina. Therefore, we used bona fide molecular marker along with data from the literature in order to suggest and indicate the most likely cell types candidates responsible for some of the changes in lipid metabolism that we observed in our study. Nevertheless, one should be cautious and understand that other cell types may also be involved in these processes. Further studies are necessary to better delineated these associations. Finally, for the lipidomic analysis, we used the LC-MS untargeted measurement and standards that did not take into consideration more specific types of lipids, such as oxylipins and oxysterols.

6. Author contributions

Conceptualization, R.J.G. and S.M. with support of all co-authors; Methodology, R.J.G., S.M., A.I., and L.C.A.; Formal Analysis, A.I. and J.S.M.; Investigation, A.I. and L.C.A.; Resources, R.J.G., S.M., and J.C.S.; Data Curation, A.I., L.C.A., and M.Y.Y.; Writing – Original Draft, R.J.G., S.M., A.I., and L.C.A.; Writing – Review & Editing, all authors and co-authors; Visualization, R.J.G., S.M., A.I., and L.C.A.; Supervision, R.J.G., S.M., and J.C.S.; Funding Acquisition, R.J.G. and S.M.

7. Acknowledgments

This work was supported by research grants from São Paulo Research Foundation (FAPESP; www.fapesp.br) (grants 2019/25828-8 to RJG, CEPID-Redoxoma 2013/07937-8 to SM and fellowship 2017/13804-1 to AI), the National Council for Scientific and Technological Development (CNPq; www.cnpq.br) (grants 310485/2021-5 to RJG and 313926/2021-2 to SM) and research fellowships. This study was also financed in part by the Coordenação de Aperfeiçoamento de Pessoal de Nível Superior (CAPES; www.capes.gov.br), Finance Code 001. The funders had no role in study design, data collection and analysis, decision to publish, or preparation of the manuscript.

8. Declaration of interests

The authors declare no competing interests.

9. Inclusion and diversity

We support inclusive, diverse, and equitable conduct of research.

10. Figure titles and legends

See individual figures embedded in the text.

11. STAR Methods

RESOURCE AVAILABILITY

Lead contact

Further information and requests for resources and reagents should be directed to and will be fulfilled by the lead contact, R.J.G. (giordano@iq.usp.br).

Materials availability

This study did not generate new unique reagents.

Data and code availability

- As previously reported¹⁹, sequencing metadata for the RNA-seq data used in the manuscript have been deposited at the Sequence Read Archive (SRA) under accession number BioProject PRJNA483866. RNA-seq data is available under accession number SRP155931. Lipidomics raw files have been deposited at MetaboLights⁷⁵ under the unique identifier MTBLS6965. Lipid quantification data are available at Mendeley Data (DOI: 10.17632/sn5hz3s992.1). They are publicly available as of the date of publication. Accession numbers are also listed in the key resources table.
- This paper does not report original code.
- Any additional information required to reanalyze the data reported in this paper is available from the lead contact upon request.

EXPERIMENTAL MODEL

Study approval. All experimental procedures were approved by the Animal Study Ethics Committee from the Institute of Chemistry (protocol number 73/2017). C57BL/6j mice (RRID:IMSR_JAX:000664) were maintained at the animal facility of the Chemistry Institute and Pharmacy School of the University of São Paulo.

Murine model of OIR. In the OIR model, pathological angiogenesis is induced in mice through their exposure to variable oxygen levels. Thus, mouse pups with their nursing mothers were kept at 75% O₂ from postnatal day 7 (P7) until day 12 (P12). Mice were then returned to ambient air (~20.8% O₂) and retinas (*N*=6) were collected at different time points (P12, P12.5, P15 and P17) for lipid extraction. Retinas from mouse pups under physiological development were also collected.

METHOD DETAILS

Lipid extraction. Lipid extraction was performed according to a method adapted from Bligh and Dyer (1959)⁷⁶. Retinas were initially lysed in 600 µL of 50 mM phosphate buffer (pH 7.4) containing 100 µM deferoxamine mesylate (Cat# D9533, Sigma-Aldrich), with zirconia beads and a Mixer Mill MM 301 homogenizer (Retsch GmbH, Haan, Germany). Lysis was performed with a cycle of 1 min at a frequency of 30 s⁻¹. 10 µL aliquots of the prepared homogenates were used to quantify proteins with Pierce™ BCA Protein Assay Kit (Cat# 23227, Thermo Fisher Scientific). 500 µL aliquots were then used in the lipid extraction procedure. These aliquots were mixed with 400 µL of ice-cold methanol containing 100 µM butylated hydroxytoluene (Cat# W218405, Sigma-Aldrich), and 100 µL of lipid internal standards (**Table S1**), which are necessary for semi-quantification of lipid molecular species. 2.0 mL of chloroform: ethyl acetate (4:1) were added to each mixture, followed by vortexing during 30 s. After centrifugation at 1,500 x *g* for 2 min at 4 °C, the lower phase containing the total lipid extracts (TLE) was transferred to new tubes and dried under N₂ gas. Dried TLE were dissolved in 100 µL of isopropanol and the HPLC injection volume was set at 1 µL.

Lipidomic analysis. Non-targeted lipidomic analysis of major lipids was performed by reverse-phase liquid chromatography coupled to mass spectrometry (RPLC-MS)^{77,78}. In detail, TLE were analyzed by electrospray ionization time-of-flight mass spectrometry (ESI-TOFMS, Triple TOF 6600, Sciex, Concord, USA) interfaced with ultra high-performance liquid chromatography (UHPLC Nexera, Shimadzu, Kyoto, Japan). The samples were loaded into a C18 column (1.6 µm, 2.1 mm i.d. x 100 mm, CORTECS®, Waters Corporation, Milford, USA) with

a flow rate of 0.2 mL/min and an oven temperature maintained at 35°C. For the liquid chromatography, mobile phase A consisted of water: acetonitrile (60:40), while mobile phase B was composed of isopropanol: acetonitrile: water (88:10:2). Mobile phases A and B were supplemented with ammonium acetate or ammonium formate (at a final concentration of 10 mM) for experiments performed in negative or positive ionization modes, respectively. The linear gradient used in RPLC was 40% to 100% B over the first 10 min and held at 100% B for additional 2 min, decreased from 100 to 40% B during the next 1 min, and held at 40% B for the remaining 7 min, totalizing a 20 min run. The MS was operated in both positive and negative ionization modes, and the scan range set at a mass-to-charge ratio of 200-2000 Da. Data for lipid molecular species identification and quantification were obtained by Information Dependent Acquisition (IDA®). Data acquisition was performed with a period cycle time of 1.05 s with 100 ms acquisition time for MS1 scan and 25 ms acquisition time to obtain the top 36 precursor ions. Data acquisition was performed using Analyst®TF 1.7.1 (RRID:SCR_015785) with an ion spray voltage of -4.5 kV and 5.5 kV for negative and positive modes, respectively, and the cone voltage at +/- 80 V. The curtain gas was set at 25 psi, nebulizer and heater gases at 45 psi and interface heater at 450 °C. The MS/MS data was analyzed with PeakView® 2.2 (RRID:SCR_015786), and lipid molecular species were manually identified with the help of an in-house manufactured Excel-based macro. The lipid quantification was performed with MultiQuant® 3.0.3, in which peak areas of precursor ions were normalized to those of the internal standards. Final data were expressed as mass of lipid species per mass of total proteins, and graphs were constructed with GraphPad Prism 8.4.3 (RRID:SCR_002798).

Transcriptomic analysis. Transcriptomic data described by Guarischi-Sousa et al.¹⁹ were re-analyzed in order to allow their integration with lipidomic data presented here. Gene expression was analyzed in pairs covering the pathological and physiological conditions at a same time point, that is, R12 x P12, R15 x P15 and R17 x P17, in addition to R12.5 x P12. Log₂(fold change) values were obtained for the expression of 32,569 genes, using DESeq2 R package (RRID:SCR_015687)⁷⁹, from which differentially expressed lipid metabolism-related genes (p-value < 0.05 or FDR-adjusted p-value < 0.05) were annotated manually and with the aid of KEGG (RRID:SCR_012773)⁸⁰, LIPID MAPS (RRID:SCR_006579)⁸¹, Reactome (RRID:SCR_003485)⁸² and WikiPathways (RRID:SCR_002134)⁸³ databases for *Mus musculus*.

QUANTIFICATION AND STATISTICAL ANALYSIS

Statistical analysis for lipidomic data was performed with MetaboAnalyst 5.0 (RRID:SCR_015539)⁸⁴ and R. We used MetaboAnalyst to build heatmaps and PCA graphs, and also to obtain ‘fold change’ values, following Xia

and Wishart's protocols⁸⁵. Data were log transformed (base 10) prior to statistical analysis. All groups were compared by one-way ANOVA followed by Tukey's HSD post-hoc test (FDR-adjusted p -value ≤ 0.05). For pairwise comparisons, bar graphs were constructed with \log_2 (fold change) values of lipid species whose variation was significant (Student's t -test, FDR-adjusted p -value ≤ 0.05 , and fold change set to ≥ 1.5). In the case of Figures 2A, 3B, 3C, 4B, 4C, 5A-C, and Figure S1 (graphs: \log_2 of normalized mass values), Shapiro-Wilk normality test⁸⁶ was conducted to check if the data followed a normal distribution. Also, Levene's test⁸⁷ was performed to verify the homoscedasticity of the data. Both tests demonstrated that the data did not meet the assumption for parametric tests. Thus, Mann-Whitney-Wilcoxon test (also known as Mann-Whitney U test or Wilcoxon Rank Sum Test) was used to verify if the differences observed between normal and OIR retinas were significant. Only data presented in Figures 3B and Figure S1 followed a normal distribution and were homoscedastic. In these cases, Student's t -tests were performed. In lipidomics, data for sample R12 (#3) was of poor quality (total ion chromatogram with very low intensity), probably due to problems with lipid extraction or sample injection. Thus, data from this sample was excluded from the final analysis. More statistical details can be found in the figure legends. For transcriptomics, the distribution and homoscedasticity of data were also verified before statistical analysis. All data were obtained from independent samples. Data with normal distribution and homoscedastic were tested using Student's t -test (two group comparisons) or ANOVA followed by Tukey's post-hoc test with Benjamin-Hochberg p -value adjustment (three or more group comparisons). Data with non-normal distribution and/or heteroscedastic were tested using the Mann-Whitney-Wilcoxon Test (two group comparisons), or Kruskal-Wallis test followed by Dunn's post-hoc test with Benjamin-Hochberg p -value adjustment⁸⁸ (three or more group comparisons).

12. References

1. Joyal, J.S., Sun, Y., Gantner, M.L., Shao, Z., Evans, L.P., Saba, N., Fredrick, T., Burnim, S., Kim, J.S., Patel, G., et al. (2016). Retinal lipid and glucose metabolism dictates angiogenesis through the lipid sensor Ffar1. *Nat Med* 22, 439-445. 10.1038/nm.4059.
2. Diaz-Coranguéz, M., Ramos, C., and Antonetti, D.A. (2017). The inner blood-retinal barrier: Cellular basis and development. *Vision Res* 139, 123-137. 10.1016/j.visres.2017.05.009.
3. Campochiaro, P.A. (2015). Molecular pathogenesis of retinal and choroidal vascular diseases. *Prog Retin Eye Res* 49, 67-81. 10.1016/j.preteyeres.2015.06.002.
4. Fliesler, S.J. (2021). Introduction to the Thematic Review Series: Seeing 2020: lipids and lipid-soluble molecules in the eye. *J Lipid Res* 62, 100007. 10.1016/j.jlr.2020.100007.
5. Lahdenranta, J., Pasqualini, R., Schlingemann, R.O., Hagedorn, M., Stallcup, W.B., Bucana, C.D., Sidman, R.L., and Arap, W. (2001). An anti-angiogenic state in mice and humans with retinal photoreceptor cell degeneration. *Proc Natl Acad Sci U S A* 98, 10368-10373. 10.1073/pnas.181329198.

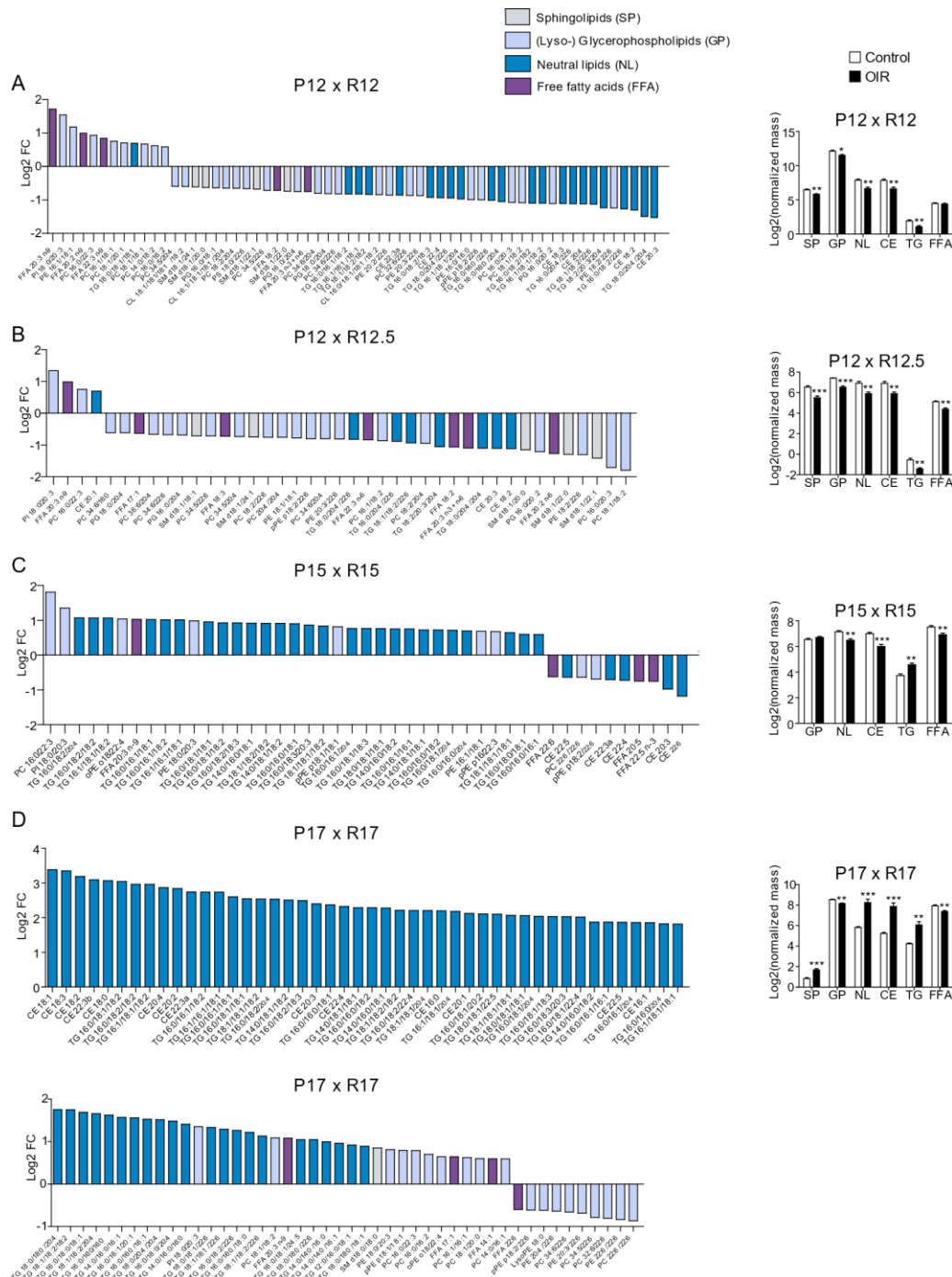
6. Fu, Z., Kern, T.S., Hellstrom, A., and Smith, L.E.H. (2021). Fatty acid oxidation and photoreceptor metabolic needs. *J Lipid Res* 62, 100035. 10.1194/jlr.TR120000618.
7. Smith, L.E., Wesolowski, E., McLellan, A., Kostyk, S.K., D'Amato, R., Sullivan, R., and D'Amore, P.A. (1994). Oxygen-induced retinopathy in the mouse. *Invest Ophthalmol Vis Sci* 35, 101-111.
8. Kim, C.B., D'Amore, P.A., and Connor, K.M. (2016). Revisiting the mouse model of oxygen-induced retinopathy. *Eye Brain* 8, 67-79. 10.2147/EB.S94447.
9. Dorrell, M.I., Aguilar, E., Jacobson, R., Trauger, S.A., Friedlander, J., Siuzdak, G., and Friedlander, M. (2010). Maintaining retinal astrocytes normalizes revascularization and prevents vascular pathology associated with oxygen-induced retinopathy. *Glia* 58, 43-54. 10.1002/glia.20900.
10. Vessey, K.A., Wilkinson-Berka, J.L., and Fletcher, E.L. (2011). Characterization of retinal function and glial cell response in a mouse model of oxygen-induced retinopathy. *J Comp Neurol* 519, 506-527. 10.1002/cne.22530.
11. Saito, Y., Geisen, P., Uppal, A., and Hartnett, M.E. (2007). Inhibition of NAD(P)H oxidase reduces apoptosis and avascular retina in an animal model of retinopathy of prematurity. *Mol Vis* 13, 840-853.
12. Liu, X., Wang, D., Liu, Y., Luo, Y., Ma, W., Xiao, W., and Yu, Q. (2010). Neuronal-driven angiogenesis: role of NGF in retinal neovascularization in an oxygen-induced retinopathy model. *Invest Ophthalmol Vis Sci* 51, 3749-3757. 10.1167/iovs.09-4226.
13. Wilkinson-Berka, J.L., Deliyanti, D., Rana, I., Miller, A.G., Agrotis, A., Armani, R., Szyndralewicz, C., Wingerler, K., Touyz, R.M., Cooper, M.E., et al. (2014). NADPH oxidase, NOX1, mediates vascular injury in ischemic retinopathy. *Antioxid Redox Signal* 20, 2726-2740. 10.1089/ars.2013.5357.
14. Dietschy, J.M., and Turley, S.D. (2004). Thematic review series: brain lipids. Cholesterol metabolism in the central nervous system during early development and in the mature animal. *J Lipid Res* 45, 1375-1397. 10.1194/jlr.R400004-JLR200.
15. Fliesler, S.J., and Bretillon, L. (2010). The ins and outs of cholesterol in the vertebrate retina. *J Lipid Res* 51, 3399-3413. 10.1194/jlr.R010538.
16. Jun, B., Mukherjee, P.K., Asatryan, A., Kautzmann, M.A., Heap, J., Gordon, W.C., Bhattacharjee, S., Yang, R., Petasis, N.A., and Bazan, N.G. (2017). Elovans are novel cell-specific lipid mediators necessary for neuroprotective signaling for photoreceptor cell integrity. *Sci Rep* 7, 5279. 10.1038/s41598-017-05433-7.
17. Bazan, N.G. (2021). Overview of how N32 and N34 elovans sustain sight by protecting retinal pigment epithelial cells and photoreceptors. *J Lipid Res* 62, 100058. 10.1194/jlr.TR120001137.
18. Folkman, J. (2007). Angiogenesis: an organizing principle for drug discovery? *Nat Rev Drug Discov* 6, 273-286. 10.1038/nrd2115.
19. Guarischi-Sousa, R., Monteiro, J.S., Alecrim, L.C., Michaloski, J.S., Cardeal, L.B., Ferreira, E.N., Carraro, D.M., Nunes, D.N., Dias-Neto, E., Reimand, J., et al. (2019). A transcriptome-based signature of pathological angiogenesis predicts breast cancer patient survival. *PLoS Genet* 15, e1008482. 10.1371/journal.pgen.1008482.
20. Ishikawa, K., Yoshida, S., Kadota, K., Nakamura, T., Niiro, H., Arakawa, S., Yoshida, A., Akashi, K., and Ishibashi, T. (2010). Gene expression profile of hyperoxic and hypoxic retinas in a mouse model of oxygen-induced retinopathy. *Invest Ophthalmol Vis Sci* 51, 4307-4319. 10.1167/iovs.09-4605.
21. Bartakova, A., Weiner, G., Oldham, M., Ferrara, N., Daneman, R., and Nudleman, E. (2018). Endothelial cell specific gene expression changes in Oxygen Induced Retinopathy (OIR). *Investigative Ophthalmology & Visual Science* 59, 5470-5470.
22. Zhou, H., Song, H., Wu, Y., Liu, X., Li, J., Zhao, H., Tang, M., Ji, X., Zhang, L., Su, Y., et al. (2019). Oxygen-induced circRNA profiles and coregulatory networks in a retinopathy of prematurity mouse model. *Exp Ther Med* 18, 2037-2050. 10.3892/etm.2019.7819.
23. Zasada, M., Madetko-Talowska, A., Revhaug, C., Rognlien, A.G.W., Baumbusch, L.O., Ksiazek, T., Szewczyk, K., Grabowska, A., Bik-Multanowski, M., Jozef Pietrzyk, J., et al. (2020). Short- and long-term impact of hyperoxia on the blood and retinal cells' transcriptome in a mouse model of oxygen-induced retinopathy. *Pediatr Res* 87, 485-493. 10.1038/s41390-019-0598-y.
24. Kim, S.J., Jin, J., Kim, Y.J., Kim, Y., and Yu, H.G. (2012). Retinal proteome analysis in a mouse model of ox-

- xygen-induced retinopathy. *J Proteome Res* 11, 5186-5203. 10.1021/pr300389r.
25. Tu, C., Beharry, K.D., Shen, X., Li, J., Wang, L., Aranda, J.V., and Qu, J. (2015). Proteomic profiling of the retinas in a neonatal rat model of oxygen-induced retinopathy with a reproducible ion-current-based MS1 approach. *J Proteome Res* 14, 2109-2120. 10.1021/pr501238m.
 26. Vahatupa, M., Nattinen, J., Jylha, A., Aapola, U., Kataja, M., Koobi, P., Jarvinen, T.A.H., Uusitalo, H., and Uusitalo-Jarvinen, H. (2018). SWATH-MS Proteomic Analysis of Oxygen-Induced Retinopathy Reveals Novel Potential Therapeutic Targets. *Invest Ophthalmol Vis Sci* 59, 3294-3306. 10.1167/iovs.18-23831.
 27. Zhou, Y., Tan, W., Zou, J., Cao, J., Huang, Q., Jiang, B., Yoshida, S., and Li, Y. (2021). Metabolomics Analyses of Mouse Retinas in Oxygen-Induced Retinopathy. *Invest Ophthalmol Vis Sci* 62, 9. 10.1167/iovs.62.10.9.
 28. Michaloski, J.S., Redondo, A.R., Magalhaes, L.S., Cambui, C.C., and Giordano, R.J. (2016). Discovery of pan-VEGF inhibitory peptides directed to the extracellular ligand-binding domains of the VEGF receptors. *Sci Adv* 2, e1600611. 10.1126/sciadv.1600611.
 29. Frohman, M.A. (2015). The phospholipase D superfamily as therapeutic targets. *Trends Pharmacol Sci* 36, 137-144. 10.1016/j.tips.2015.01.001.
 30. Egea-Jimenez, A.L., and Zimmermann, P. (2018). Phospholipase D and phosphatidic acid in the biogenesis and cargo loading of extracellular vesicles. *J Lipid Res* 59, 1554-1560. 10.1194/jlr.R083964.
 31. Tserentsoodol, N., Gordiyenko, N.V., Pascual, I., Lee, J.W., Fliesler, S.J., and Rodriguez, I.R. (2006). Intraretinal lipid transport is dependent on high density lipoprotein-like particles and class B scavenger receptors. *Mol Vis* 12, 1319-1333.
 32. Saadane, A., Mast, N., Dao, T., Ahmad, B., and Pikuleva, I.A. (2016). Retinal Hypercholesterolemia Triggers Cholesterol Accumulation and Esterification in Photoreceptor Cells. *J Biol Chem* 291, 20427-20439. 10.1074/jbc.M116.744656.
 33. Shih, A.Y., Sligar, S.G., and Schulten, K. (2009). Maturation of high-density lipoproteins. *J R Soc Interface* 6, 863-871. 10.1098/rsif.2009.0173.
 34. Kontush, A., and Chapman, M.J. (2011). High-density lipoproteins: structure, metabolism, function and therapeutics (John Wiley & Sons).
 35. Komati, R., Spadoni, D., Zheng, S., Sridhar, J., Riley, K.E., and Wang, G. (2017). Ligands of Therapeutic Utility for the Liver X Receptors. *Molecules* 22. 10.3390/molecules22010088.
 36. Liu, Y., Wei, Z., Ma, X., Yang, X., Chen, Y., Sun, L., Ma, C., Miao, Q.R., Hajjar, D.P., Han, J., and Duan, Y. (2018). 25-Hydroxycholesterol activates the expression of cholesterol 25-hydroxylase in an LXR-dependent mechanism. *J Lipid Res* 59, 439-451. 10.1194/jlr.M080440.
 37. Cuchel, M., and Rader, D.J. (2006). Macrophage reverse cholesterol transport: key to the regression of atherosclerosis? *Circulation* 113, 2548-2555. 10.1161/CIRCULATIONAHA.104.475715.
 38. Raghow, R., Yellaturu, C., Deng, X., Park, E.A., and Elam, M.B. (2008). SREBPs: the crossroads of physiological and pathological lipid homeostasis. *Trends Endocrinol Metab* 19, 65-73. 10.1016/j.tem.2007.10.009.
 39. WikiPathways (2022). Cholesterol metabolism with Bloch and Kandutsch-Russell pathways (Mus musculus). http://www.wikipathways.org/instance/WP4346_r123453.
 40. Agbaga, M.P., Mandal, M.N., and Anderson, R.E. (2010). Retinal very long-chain PUFAs: new insights from studies on ELOVL4 protein. *J Lipid Res* 51, 1624-1642. 10.1194/jlr.R005025.
 41. Deliyanti, D., Lee, J.Y., Petratos, S., Meyer, C.J., Ward, K.W., Wilkinson-Berka, J.L., and de Haan, J.B. (2016). A potent Nrf2 activator, dh404, bolsters antioxidant capacity in glial cells and attenuates ischaemic retinopathy. *Clin Sci (Lond)* 130, 1375-1387. 10.1042/CS20160068.
 42. Shi, X., Li, P., Liu, H., and Prokosch, V. (2022). Oxidative Stress, Vascular Endothelium, and the Pathology of Neurodegeneration in Retina. *Antioxidants (Basel)* 11. 10.3390/antiox11030543.
 43. Olzmann, J.A., and Carvalho, P. (2019). Dynamics and functions of lipid droplets. *Nat Rev Mol Cell Biol* 20, 137-155. 10.1038/s41580-018-0085-z.
 44. Bailey, A.P., Koster, G., Guillermier, C., Hirst, E.M., MacRae, J.I., Lechene, C.P., Postle, A.D., and Gould, A.P. (2015). Antioxidant Role for Lipid Droplets in a Stem Cell Niche of Drosophila. *Cell* 163, 340-353. 10.1016/j.cell.2015.09.020.
 45. Orban, T., Palczewska, G., and Palczewski, K. (2011). Retinyl ester storage particles (retinosomes) from

- the retinal pigmented epithelium resemble lipid droplets in other tissues. *J Biol Chem* 286, 17248-17258. 10.1074/jbc.M110.195198.
46. Van Den Brink, D.M., Cubizolle, A., Chatelain, G., Davoust, N., Girard, V., Johansen, S., Napoletano, F., Dourlen, P., Guillou, L., Angebault-Prouteau, C., et al. (2018). Physiological and pathological roles of FATP-mediated lipid droplets in *Drosophila* and mice retina. *PLoS Genet* 14, e1007627. 10.1371/journal.pgen.1007627.
 47. Yako, T., Otsu, W., Nakamura, S., Shimazawa, M., and Hara, H. (2022). Lipid Droplet Accumulation Promotes RPE Dysfunction. *Int J Mol Sci* 23. 10.3390/ijms23031790.
 48. Apte, R.S. (2016). Targeting Tissue Lipids in Age-related Macular Degeneration. *EBioMedicine* 5, 26-27. 10.1016/j.ebiom.2016.02.003.
 49. Mehta, R., Elias-Lopez, D., Martagon, A.J., Perez-Mendez, O.A., Sanchez, M.L.O., Segura, Y., Tusie, M.T., and Aguilar-Salinas, C.A. (2021). LCAT deficiency: a systematic review with the clinical and genetic description of Mexican kindred. *Lipids Health Dis* 20, 70. 10.1186/s12944-021-01498-6.
 50. Modjtahedi, B.S., Bose, N., Papakostas, T.D., Morse, L., Vavvas, D.G., and Kishan, A.U. (2016). Lipids and Diabetic Retinopathy. *Semin Ophthalmol* 31, 10-18. 10.3109/08820538.2015.1114869.
 51. Chou, Y., Ma, J., Su, X., and Zhong, Y. (2020). Emerging insights into the relationship between hyperlipidemia and the risk of diabetic retinopathy. *Lipids Health Dis* 19, 241. 10.1186/s12944-020-01415-3.
 52. Busik, J.V. (2021). Lipid metabolism dysregulation in diabetic retinopathy. *J Lipid Res* 62, 100017. 10.1194/jlr.TR120000981.
 53. Ortiz, A., Gui, J., Zahedi, F., Yu, P., Cho, C., Bhattacharya, S., Carbone, C.J., Yu, Q., Katlinski, K.V., Katlinskaya, Y.V., et al. (2019). An Interferon-Driven Oxysterol-Based Defense against Tumor-Derived Extracellular Vesicles. *Cancer Cell* 35, 33-45 e36. 10.1016/j.ccell.2018.12.001.
 54. Lembo, D., Cagno, V., Civra, A., and Poli, G. (2016). Oxysterols: An emerging class of broad spectrum antiviral effectors. *Mol Aspects Med* 49, 23-30. 10.1016/j.mam.2016.04.003.
 55. Bennett, L.D., Hopiavuori, B.R., Brush, R.S., Chan, M., Van Hook, M.J., Thoreson, W.B., and Anderson, R.E. (2014). Examination of VLC-PUFA-deficient photoreceptor terminals. *Invest Ophthalmol Vis Sci* 55, 4063-4072. 10.1167/iovs.14-13997.
 56. Hopiavuori, B.R., Anderson, R.E., and Agbaga, M.P. (2019). ELOVL4: Very long-chain fatty acids serve an eclectic role in mammalian health and function. *Prog Retin Eye Res* 69, 137-158. 10.1016/j.preteyeres.2018.10.004.
 57. Gorusupudi, A., Liu, A., Hageman, G.S., and Bernstein, P.S. (2016). Associations of human retinal very long-chain polyunsaturated fatty acids with dietary lipid biomarkers. *J Lipid Res* 57, 499-508. 10.1194/jlr.P065540.
 58. Gorusupudi, A., Rallabandi, R., Li, B., Arunkumar, R., Blount, J.D., Rognon, G.T., Chang, F.Y., Wade, A., Lucas, S., Conboy, J.C., et al. (2021). Retinal bioavailability and functional effects of a synthetic very-long-chain polyunsaturated fatty acid in mice. *Proc Natl Acad Sci U S A* 118. 10.1073/pnas.2017739118.
 59. Lapillonne, A., dit Trolli, S.E., and Kermorvant-Duchemin, E. (2010). Postnatal docosahexaenoic acid deficiency is an inevitable consequence of current recommendations and practice in preterm infants. *Neonatology* 98, 397-403.
 60. Fu, Z., Lofqvist, C.A., Shao, Z., Sun, Y., Joyal, J.-S., Hurst, C.G., Cui, R.Z., Evans, L.P., Tian, K., and SanGiovanni, J.P. (2015). Dietary ω -3 polyunsaturated fatty acids decrease retinal neovascularization by adipose-endoplasmic reticulum stress reduction to increase adiponectin. *The American journal of clinical nutrition* 101, 879-888.
 61. Lofqvist, C., Najm, S., and Hellgren, G. (2018). Association of Retinopathy of Prematurity With Low Levels of Arachidonic Acid: A Secondary Analysis of a Randomized Clinical Trial (vol 136, pg 271, 2018). *JAMA OPHTHALMOLOGY* 136, 1078-1078.
 62. Tomita, Y., Usui-Ouchi, A., Nilsson, A.K., Yang, J., Ko, M., Hellstrom, A., and Fu, Z. (2021). Metabolism in Retinopathy of Prematurity. *Life (Basel)* 11. 10.3390/life11111119.
 63. Else, P.L. (2020). The highly unnatural fatty acid profile of cells in culture. *Prog Lipid Res* 77, 101017. 10.1016/j.plipres.2019.101017.

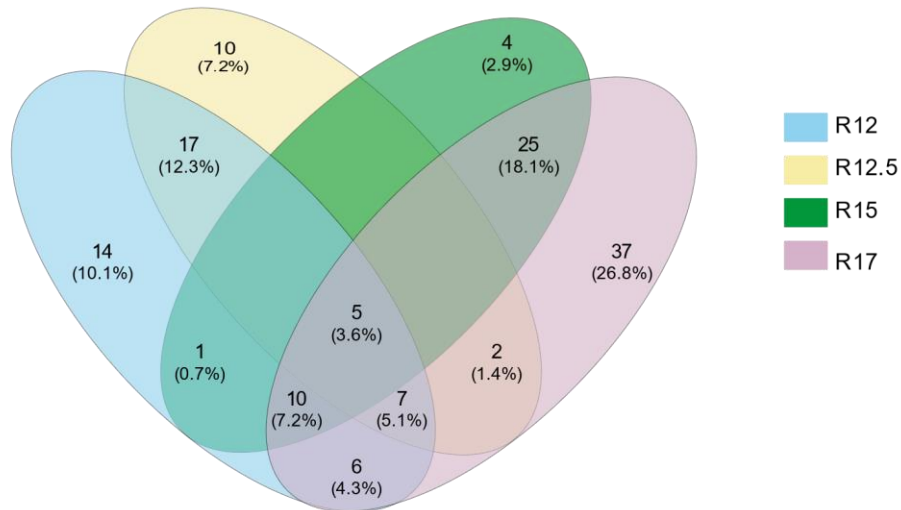
64. Vriens, K., Christen, S., Parik, S., Broekaert, D., Yoshinaga, K., Talebi, A., Dehairs, J., Escalona-Noguero, C., Schmieder, R., Cornfield, T., et al. (2019). Evidence for an alternative fatty acid desaturation pathway increasing cancer plasticity. *Nature* 566, 403-406. 10.1038/s41586-019-0904-1.
65. Ichi, I., Kono, N., Arita, Y., Haga, S., Arisawa, K., Yamano, M., Nagase, M., Fujiwara, Y., and Arai, H. (2014). Identification of genes and pathways involved in the synthesis of Mead acid (20:3n-9), an indicator of essential fatty acid deficiency. *Biochim Biophys Acta* 1841, 204-213. 10.1016/j.bbaliip.2013.10.013.
66. Löfqvist, C.A., Najm, S., Hellgren, G., Engström, E., Sävman, K., Nilsson, A.K., Andersson, M.X., Hård, A.-L., Smith, L.E.H., and Hellström, A. (2018). Association of Retinopathy of Prematurity With Low Levels of Arachidonic Acid: A Secondary Analysis of a Randomized Clinical Trial. *JAMA Ophthalmology* 136, 271-277. 10.1001/jamaophthalmol.2017.6658.
67. Beken, S., Dilli, D., Fettah, N.D., Kabatas, E.U., Zenciroglu, A., and Okumus, N. (2014). The influence of fish-oil lipid emulsions on retinopathy of prematurity in very low birth weight infants: a randomized controlled trial. *Early Hum Dev* 90, 27-31. 10.1016/j.earlhumdev.2013.11.002.
68. Najm, S., Löfqvist, C., Hellgren, G., Engström, E., Lundgren, P., Hård, A.L., Lapillonne, A., Sävman, K., Nilsson, A.K., Andersson, M.X., et al. (2017). Effects of a lipid emulsion containing fish oil on polyunsaturated fatty acid profiles, growth and morbidities in extremely premature infants: A randomized controlled trial. *Clin Nutr ESPEN* 20, 17-23. 10.1016/j.clnesp.2017.04.004.
69. Tikhonenko, M., Lydic, T.A., Wang, Y., Chen, W., Opreanu, M., Sochacki, A., McSorley, K.M., Renis, R.L., Kern, T., Jump, D.B., et al. (2010). Remodeling of retinal Fatty acids in an animal model of diabetes: a decrease in long-chain polyunsaturated fatty acids is associated with a decrease in fatty acid elongases Elovl2 and Elovl4. *Diabetes* 59, 219-227. 10.2337/db09-0728.
70. Leger-Charnay, E., Gambert, S., Martine, L., Dubus, E., Maire, M.A., Buteau, B., Morala, T., Gigot, V., Bron, A.M., Bretilon, L., and Masson, E.A.Y. (2022). Retinal cholesterol metabolism is perturbed in response to experimental glaucoma in the rat. *PLoS One* 17, e0264787. 10.1371/journal.pone.0264787.
71. van Leeuwen, E.M., Emri, E., Merle, B.M.J., Colijn, J.M., Kersten, E., Cougnard-Gregoire, A., Dammeier, S., Meester-Smoor, M., Pool, F.M., de Jong, E.K., et al. (2018). A new perspective on lipid research in age-related macular degeneration. *Prog Retin Eye Res* 67, 56-86. 10.1016/j.preteyeres.2018.04.006.
72. Park, S.J., and Park, D.H. (2020). REvisiting Lipids in RETinal Diseases: A Focused Review on Age-related Macular Degeneration and Diabetic Retinopathy. *J Lipid Atheroscler* 9, 406-418. 10.12997/jla.2020.9.3.406.
73. Ashton, N., Ward, B., and Serpell, G. (1954). Effect of oxygen on developing retinal vessels with particular reference to the problem of retrolental fibroplasia. *Br J Ophthalmol* 38, 397-432. 10.1136/bjo.38.7.397.
74. Liu, C.H., Wang, Z., Sun, Y., and Chen, J. (2017). Animal models of ocular angiogenesis: from development to pathologies. *FASEB J* 31, 4665-4681. 10.1096/fj.201700336R.
75. Haug, K., Cochrane, K., Nainala, V.C., Williams, M., Chang, J., Jayaseelan, K.V., and O'Donovan, C. (2020). MetaboLights: a resource evolving in response to the needs of its scientific community. *Nucleic Acids Res* 48, D440-D444. 10.1093/nar/gkz1019.
76. Bligh, E.G., and Dyer, W.J. (1959). A rapid method of total lipid extraction and purification. *Can J Biochem Physiol* 37, 911-917. 10.1139/o59-099.
77. Chaves-Filho, A.B., Pinto, I.F.D., Dantas, L.S., Xavier, A.M., Inague, A., Faria, R.L., Medeiros, M.H.G., Glezer, I., Yoshinaga, M.Y., and Miyamoto, S. (2019). Alterations in lipid metabolism of spinal cord linked to amyotrophic lateral sclerosis. *Sci Rep* 9, 11642. 10.1038/s41598-019-48059-7.
78. Macedo, F., Martins, G.L., Luevano-Martinez, L.A., Viana, G.M., Riske, K.A., Inague, A., Yoshinaga, M.Y., Aguilaniu, H., Miyamoto, S., Glezer, I., and da Cunha, F.M. (2020). Lipase-like 5 enzyme controls mitochondrial activity in response to starvation in *Caenorhabditis elegans*. *Biochim Biophys Acta Mol Cell Biol Lipids* 1865, 158539. 10.1016/j.bbaliip.2019.158539.
79. Love, M.I., Huber, W., and Anders, S. (2014). Moderated estimation of fold change and dispersion for RNA-seq data with DESeq2. *Genome Biol* 15, 550. 10.1186/s13059-014-0550-8.
80. Kanehisa, M. (1997). A database for post-genome analysis. *Trends Genet* 13, 375-376. 10.1016/s0168-9525(97)01223-7.
81. Fahy, E., Subramaniam, S., Brown, H.A., Glass, C.K., Merrill, A.H., Jr., Murphy, R.C., Raetz, C.R., Russell,

- D.W., Seyama, Y., Shaw, W., et al. (2005). A comprehensive classification system for lipids. *J Lipid Res* 46, 839-861. 10.1194/jlr.E400004-JLR200.
82. Fabregat, A., Sidiropoulos, K., Garapati, P., Gillespie, M., Hausmann, K., Haw, R., Jassal, B., Jupe, S., Korninger, F., McKay, S., et al. (2016). The Reactome pathway Knowledgebase. *Nucleic Acids Res* 44, D481-487. 10.1093/nar/gkv1351.
83. Pico, A.R., Kelder, T., van Iersel, M.P., Hanspers, K., Conklin, B.R., and Evelo, C. (2008). WikiPathways: pathway editing for the people. *PLoS Biol* 6, e184. 10.1371/journal.pbio.0060184.
84. Xia, J., Psychogios, N., Young, N., and Wishart, D.S. (2009). MetaboAnalyst: a web server for metabolomic data analysis and interpretation. *Nucleic Acids Res* 37, W652-660. 10.1093/nar/gkp356.
85. Xia, J., and Wishart, D.S. (2016). Using MetaboAnalyst 3.0 for Comprehensive Metabolomics Data Analysis. *Curr Protoc Bioinformatics* 55, 14 10 11-14 10 91. 10.1002/cpbi.11.
86. SHAPIRO, S.S., and WILK, M.B. (1965). An analysis of variance test for normality (complete samples)†. *Biometrika* 52, 591-611. 10.1093/biomet/52.3-4.591.
87. Olkin, I. (1960). Contributions to probability and statistics; essays in honor of Harold Hotelling (Stanford University Press).
88. Benjamini, Y., and Hochberg, Y. (1995). Controlling the false discovery rate: a practical and powerful approach to multiple testing. *Journal of the Royal statistical society: series B (Methodological)* 57, 289-300.

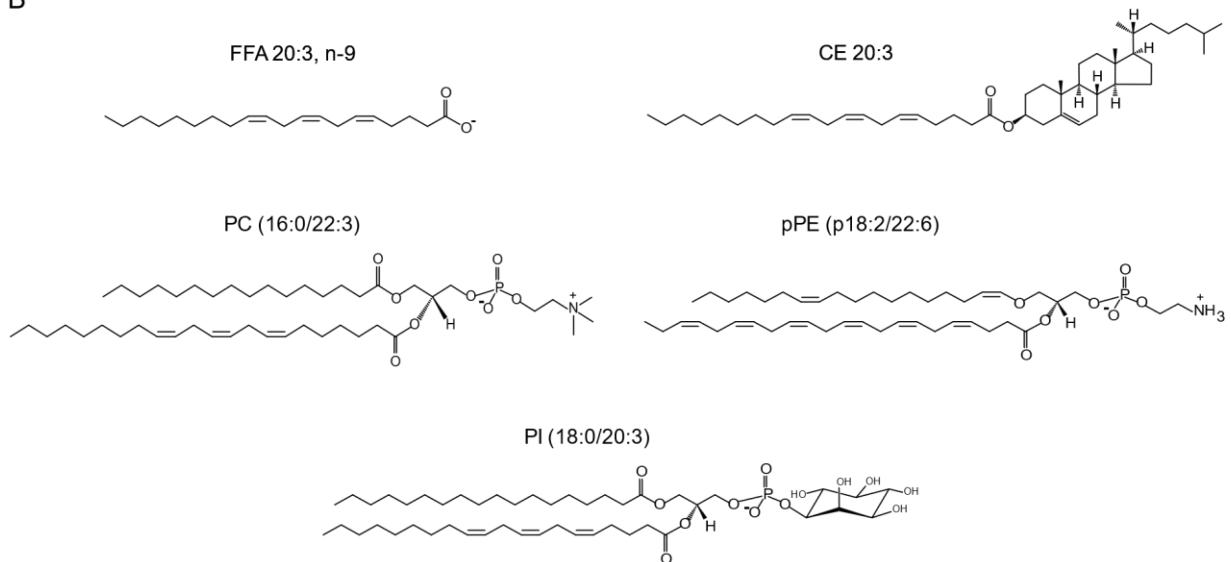


Supplemental Figure 1. *OIR promotes substantial lipid remodelling.* Pairwise comparisons showing major lipid alterations promoted by OIR at different postnatal days: day 12 (**A**), day 12.5 (**B**), day 15 (**C**) and day 17 (**D**). Y-axis corresponds to \log_2 (fold change) observed for each lipid molecular species. Fold change was set to ≥ 1.5 ; FDR adjusted p -value ≤ 0.05 was used for significance. Considering the species highlighted in the pairwise comparisons (P12 x R12, P12 x R12.5, P15 x R15 and P17 x R17), that is, those with FDR-adjusted p -value ≤ 0.05 and fold change ≥ 1.5 , bar graphs were made using the \log_2 of their normalized mass values. These species were grouped into different lipid categories (SP, GP, NL and FFA). In the bar graphs, lipid classes of CE and TG are also shown individually. Statistics: Student's t -test (* $p \leq 0.05$, ** $p \leq 0.01$, *** $p \leq 0.001$).

A



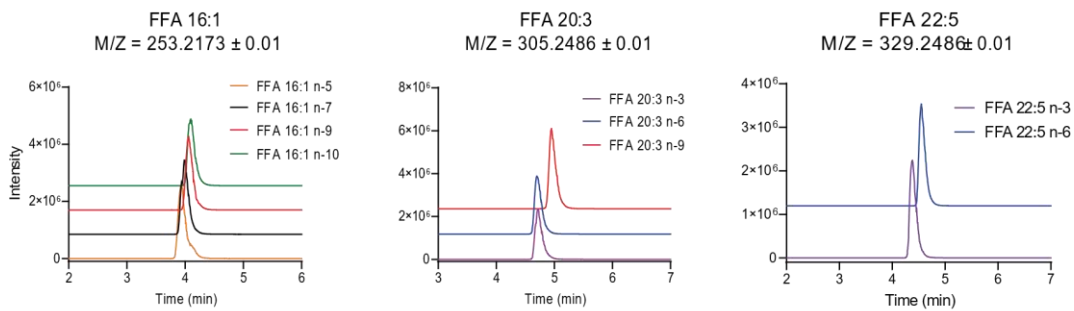
B



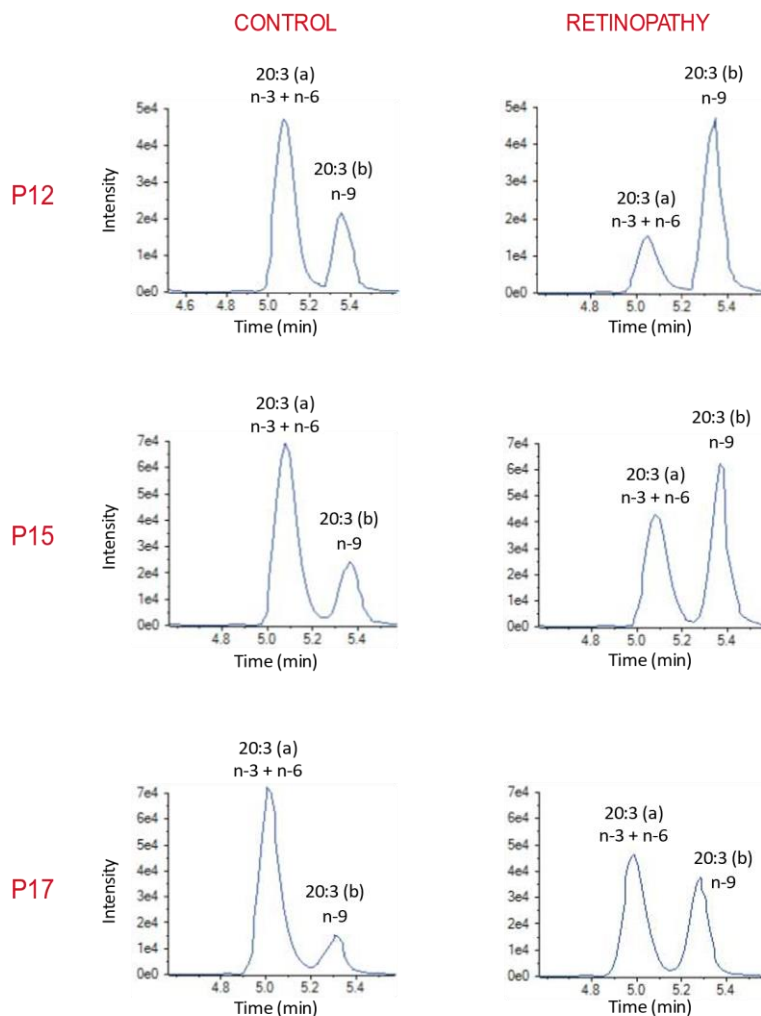
Supplemental Figure 3. Overview of altered lipid species in pathological retinas. **A.** Venn-diagram of significantly altered lipids (T-student test, FDR adjusted p -value ≤ 0.05 , fold change ≥ 1.5) in the pathological (OIR) condition at postnatal days 12, 12.5, 15 and 17. All species listed in the Venn-diagram are properly named in the supplemental file “**Supplemental material - Venn diagram**” (below). **B.** Representative structure of the 5 lipid molecular species that are altered at all analyzed postnatal days.

A

The higher the value of "n", the longer the retention time



B

FFA 20:3 isomers ($M/Z = 253.2173 \pm 0.01$)

Supplemental Figure 4. FFA isomers characterization. **A.** Chromatograms showing the retention times of commercial standards of the following FFA isomers: 16:1 (n-5, n-7, n-9, n-10), 20:3 (n-3, n-6, n-9) and 22:5 (n-3 and n-6). All are in the cis configuration. **B.** Chromatograms obtained by HPLC coupled with HR-MS/MS for the m/z value of 305.2486 ± 0.01 , referring to FFA 20:3, which presented two peaks: a) FFA 20:3, n-6 (and possibly n-3) and b) FFA 20:3, n-9 (mead acid). Different chromatograms are presented for the different conditions (physiological vs. pathological) at three postnatal days (12, 15 and 17).

Supplemental Table 1: Mix of lipid internal standards used in lipidomic analysis

<i>Internal standards</i>	<i>Lipids</i>	<i>Conc. (ng/μL)</i>
Cholest-5-en-3β-yl (decanoate)	CE (10:0)	10
N-decanoyl-D-erythro-sphingosine	Cer d18:1/10:0	10
N-heptadecanoyl-D-erythro-sphingosine	Cer d18:1/17:0	10
1',3'-bis[1,2-dimyristoyl-sn-glycero-3-phospho]- glycerol	CL 14:0/14:0/14:0/14:0	10
1,2-diheptadecanoyl-sn-glycerol	DG 17:0/17:0	10
1-heptadecanoyl-2-hydroxy-sn-glycero-3- phosphocholine	LysoPC 17:0	10
1-(10Z-heptadecenoyl)-sn-glycero-3- phosphoethanolamine	LysoPE 17:1	10
1,2-diheptadecanoyl-sn-glycero-3-phosphate	PA 17:0/17:0	10
1,2-dimyristoyl-sn-glycero-3-phosphocholine	PC 14:0/14:0	10
1,2-diheptadecanoyl-sn-glycero-3-phosphocholine	PC 17:0/17:0	10
1,2-dimyristoyl-sn-glycero-3-phosphoethanolamine	PE 14:0/14:0	10
1,2-diheptadecanoyl-sn-glycero-3- phosphoethanolamine	PE 17:0/17:0	10
1,2-diheptadecanoyl-sn-glycero-3-phospho-(1'-rac- glycerol)	PG 17:0/17:0	10
1,2-diheptadecanoyl-sn-glycero-3-phospho-L-serine	PS 17:0/17:0	10
N-heptadecanoyl-D-erythro- sphingosylphosphorylcholine	SM d18:1/17:0	10
1,2,3-tritetradecanoyl-sn-glycerol	TG 14:0/14:0/14:0	10
1,2,3-triheptadecanoyl-sn-glycerol	TG 17:0/17:0/17:0	10

Supplemental material - Venn diagram

List of lipid species in the Venn Diagram (**Supplemental Figure 3**). Red upward arrow indicates increased concentration in retinopathy, while blue downward arrow means decreased concentration.

14 elements included exclusively in R12

FFA 20:2 (n-9) (↑)
FFA 22:3 (n-9) (↑)
PC 16:1/18:1 (↑)
PC 18:1/20:1 (↑)
PC 18:1/18:1 (↑)
PC 14:0/18:2 (↑)
CL 18:1/18:1/18:1/18:2 (↓)
PG 16:0/18:1 (↓)
CL 16:1/18:1/18:1/20:4 (↓)
PS 18:0/22:6 (↓)
CL 16:0/18:1/18:1/18:2 (↓)
PE 20:2/22:6 (↓)
PE 16:0/16:0 (↓)
TG 16:0/16:0/22:6 (↓)

10 elements included exclusively in R12.5

PC 34:6/16:0 (↓)
PC 36:6/20:4 (↓)
SM d18:1/18:1 (↓)
FFA 18:3 (↓)
PC 18:2/22:6 (↓)
PC 20:4/20:4 (↓)
PE 18:1/18:1 (↓)
FFA 22:3a (↓)
PC 16:1/18:2 (↓)
FFA 20:2 (n-6) (↓)

4 elements included exclusively in R15

pPE p16/22:3 (↑)
FFA 20:5 (↓)
FFA 22:5 (n-3) (↓)
CE 22:6 (↓)

37 elements included exclusively in R17

CE 18:1 (↑)
CE 22:3b (↑)
CE 18:0 (↑)
CE 20:2 (↑)
TG 16:0/18:2/22:4 (↑)
TG 18:1/18:1/20:4 (↑)
CE 16:0 (↑)
TG 16:0/18:1/20:2 (↑)
TG 18:0/18:1/22:5 (↑)

TG 16:0/18:1/22:4 (↑)
CE 16:1 (↑)
TG 16:1/18:1/18:1 (↑)
TG 18:0/18:0/20:4 (↑)
TG 18:1/18:2/18:2 (↑)
TG 18:1/18:2/20:4 (↑)
TG 16:0/16:0/16:0 (↑)
TG 14:0/16:0/16:1 (↑)
TG 16:0/18:1/20:1 (↑)
TG 16:0/18:0/20:4 (↑)
TG 14:0/16:0/16:0 (↑)
TG 18:0/18:1/22:6 (↑)
TG 18:1/18:1/22:6 (↑)
TG 16:0/16:0/18:0 (↑)
TG 16:0/18:1/24:5 (↑)
TG 18:0/18:0/22:6 (↑)
TG 14:0/14:0/16:0 (↑)
TG 14:0/14:0/16:1 (↑)
TG 12:0/16:0/18:1 (↑)
TG 18:0/18:0/18:1 (↑)
SM d18:0/18:0 (↑)
PC 16:1/16:1 (↑)
PC 18:1/20:0 (↑)
FFA 14:1 (↑)
PC 14:0/16:1 (↑)
LysoPE 18:0 (↓)
PE 20:4/22:6 (↓)
PE 22:6/22:6 (↓)

17 common elements in R12 and R12.5

PC 34:5/20:4 (R12↓, R12.5↓)
SM d18:1/24:1 (R12↓, R12.5↓)
SM d18:1/20:0 (R12↓, R12.5↓)
PC 18:2/20:4 (R12↓, R12.5↓)
SM d18:1/22:1 (R12↓, R12.5↓)
FFA 18:2 (R12↓, R12.5↓)
SM d18:1/22:0 (R12↓, R12.5↓)
PG 16:0/20:4 (R12↓, R12.5↓)
FFA 20:3 (n-6) (R12↓, R12.5↓)
PC 34:6/20:4 (R12↓, R12.5↓)
PG 18:0/20:4 (R12↓, R12.5↓)
TG 18:0/20:4/22:6 (R12↓, R12.5↓)
PC 16:0/20:3 (R12↓, R12.5↓)
PG 16:0/20:2 (R12↓, R12.5↓)
TG 16:0/20:4/22:6 (R12↓, R12.5↓)
TG 18:2/20:3/20:4 (R12↓, R12.5↓)
PE 18:2/22:6 (R12↓, R12.5↓)

1 common element in R12 and R15

PE 16:1/18:1 (R12↑, R15↑)

6 common elements in R12 and R17

PC 16:0/16:2 (R12↑, R17↑)
PC 32:6/22:6 (R12↓, R17↓)
TG 16:1/18:1/20:4 (R12↓, R17↑)
CE 18:3 (R12↓, R17↑)
CE 20:4 (R12↓, R17↑)
TG 16:0/18:2/22:6 (R12↓, R17↑)

2 common elements in R12.5 and R17

CE 20:1 (R12.5↑, R17↑)
FFA 17:1 (R12.5↓, R17↑)

25 common elements in R15 and R17:

TG 16:0/18:2/20:4 (R15↑, R17↑)
oPE o18/22:4 (R15↑, R17↑)
TG 16:0/16:1/18:1 (R15↑, R17↑)
PE 18:0/20:3 (R15↑, R17↑)
TG 16:0/18:1/18:1 (R15↑, R17↑)
TG 16:0/18:1/18:2 (R15↑, R17↑)
TG 14:0/16:0/18:1 (R15↑, R17↑)
TG 14:0/18:1/18:2 (R15↑, R17↑)
TG 16:0/16:0/18:1 (R15↑, R17↑)
TG 16:0/18:3/20:3 (R15↑, R17↑)
TG 18:1/18:1/18:2 (R15↑, R17↑)
pPE p18:1/18:1 (R15↑, R17↑)
TG 16:0/16:1/20:4 (R15↑, R17↑)
TG 16:0/18:1/18:3 (R15↑, R17↑)
TG 14:0/16:0/18:2 (R15↑, R17↑)
TG 16:0/16:1/16:1 (R15↑, R17↑)
TG 14:0/18:1/18:1 (R15↑, R17↑)
TG 16:0/16:0/18:2 (R15↑, R17↑)
TG 16:0/18:1/20:4 (R15↑, R17↑)
TG 18:1/18:1/18:1 (R15↑, R17↑)
TG 16:0/18:0/18:1 (R15↑, R17↑)
TG 16:0/16:0/16:1 (R15↑, R17↑)
FFA 22:6 (R15↓, R17↓)
CE 22:5 (R15↓, R17↑)
PC 22:6/22:6 (R15↓, R17↓)

7 common elements in R12, R12.5 and R17

PC 34:5/22:6 (R12↓, R12.5↓, R17↓)
PC 34:6/22:6 (R12↓, R12.5↓, R17↓)
PE 20:3/22:6 (R12↓, R12.5↓, R17↓)
PC 18:1/18:2 (R12↓, R12.5↓, R17↑)
TG 18:1/18:2/22:6 (R12↓, R12.5↓, R17↑)
CE 18:2 (R12↓, R12.5↓, R17↑)
TG 18:0/20:4/20:4 (R12↓, R12.5↓, R17↑)

10 common elements in R12, R15 and R17

TG 18:0/18:1/18:1 (R12↑, R15↑, R17↑)
TG 16:0/16:1/18:2 (R12↓, R15↑, R17↑)
TG 16:1/16:1/18:1 (R12↓, R15↑, R17↑)
TG 18:1/18:2/18:2 (R12↓, R15↑, R17↑)
CE 22:3a (R12↓, R15↓, R17↑)
TG 16:0/18:2/18:3 (R12↓, R15↑, R17↑)
CE 22:4 (R12↓, R15↓, R17↑)
TG 16:0/16:0/20:4 (R12↓, R15↑, R17↑)
TG 16:0/18:2/18:2 (R12↓, R15↑, R17↑)
TG 16:1/18:1/18:2 (R12↓, R15↑, R17↑)

5 common elements in R12, R12.5, R15 and R17

FFA 20:3 (n-9) (R12↑, R12.5↑, R15↑, R17↑)
PI 18:0/20:3 (R12↑, R12.5↑, R15↑, R17↑)
PC 16:0/22:3 (R12↑, R12.5↑, R15↑, R17↑)
pPE p18:2/22:6 (R12↓, R12.5↓, R15↓, R17↓)
CE 20:3 (R12↓, R12.5↓, R15↓, R17↑)

5. CAPÍTULO 3

Neste capítulo, serão apresentados os resultados prévios da nossa análise proteômica, que continua em andamento.

5.1. MATERIAIS E MÉTODOS

5.1.1. Animais.

As amostras de retinas geradas no modelo animal de OIR foram obtidas de camundongos C57BL/6NTac mantidos no biotério do Instituto de Química da Universidade de São Paulo de acordo com as normas e procedimentos aprovados pela comissão de ética animal e biossegurança do Instituto (CEUA 149/2019).

5.1.2. Amostras de retinas no modelo animal de OIR.

Filhotes de camundongos (C57BL/6NTac) recém-nascidos e suas mães foram colocados e mantidos em suas gaiolas entre os dias 7 pós-nascimento (P7) e P12 dentro de uma câmara com níveis de O₂ em 75%. Após este período, os camundongos retornaram para a sala do biotério com ar ambiente (20.8% O₂), e as retinas de cinco animais (N=10) foram coletadas em diferentes pontos de tempo (P12, P12.5, P15 e P17) para a análise proteômica. Retinas de filhotes de camundongos em desenvolvimento fisiológico também foram coletadas.

5.1.3. Preparo das amostras para a análise proteômica.

As retinas foram dissecadas com o auxílio de uma lupa, lavadas rapidamente em tampão PBS gelado contendo inibidor de protease.

Lise das retinas: a lise foi realizada com 500 µL de tampão de lise (10 mM HEPES, 42 mM KCl, 0.1 mM EDTA, 0.1 mM EGTA, e inibidor de protease 1X) e com *beads* de zircônia em um homogeneizador Mixer Mill MM 301 por dois ciclos de 30 segundos a uma frequência de 30 s⁻¹. Em seguida, as amostras foram centrifugadas a 15.000g por 45 minutos a 4°C. A concentração proteica foi determinada pelo kit de quantificação Pierce™ BCA Protein Assay Kit (Thermo Fisher) e as amostras foram aliquotadas e congeladas a -80 °C.

Passivação dos filtros Filtros Amicon 10kDa: foram adicionados 500 µL de ddH₂O em cada filtro e realizado uma centrifugação de 15 minutos a 14.000g, este processo foi repetido por mais uma vez, descartando o filtrado entre as centrifugações. Em seguida, os filtros foram imersos em uma solução Tween-20 5% v/v *overnight*. No dia seguinte, os filtros foram

lavados sete vezes e foram realizadas duas centrifugações de 15 minutos a 14.000g com 500 μ L de ddH₂O, sendo na última centrifugação realizado o descarte do volume morto com o auxílio de uma pipeta. 15 μ g de proteína de cada amostra foram adicionados em cada filtro com o volume ajustado para 500 μ L com solução tampão de ureia 8M em bicarbonato de amônio (Ambic) 25 mM e foi realizada uma centrifugação a 14.000 g por 20 minutos e 20 °C, este procedimento de adição do tampão ureia e centrifugação foi realizado por mais duas vezes.

Redução, alquilação e tripsinação: Foram adicionados 450 μ L de DTT (10 mM em Ambic 25 mM) e em seguida realizada uma incubação por 30 minutos a 30 °C e 600 RPM. Após a incubação, foi feita uma centrifugação de 20 minutos a 14.000 g e 20 °C. No próximo passo, foram adicionados 450 μ L de iodoacetamida (20 mM em Ambic 25 mM) e realizado uma incubação protegida da luz por 45 minutos a temperatura ambiente, seguida por uma centrifugação de 20 minutos a 14.000 g e 20 °C. Para realizar a remoção completa de DTT e iodoacetamida, foram realizadas quatro lavagens de 450 μ L com solução Ambic 25 mM seguidas de centrifugações de 20 minutos a 14.000 g e 20 °C. Por fim, foram adicionados 6 μ L da solução de tripsina 0,1 μ g/ μ L em ácido acético 1 mM [proporção 1:25 tripsina: proteínas m/m]. As amostras com essa solução foram incubadas durante a noite com agitação de 600 RPM apenas no primeiro minuto, para a mistura inicial das amostras com a tripsina.

Eluição dos peptídeos e interrupção da digestão: os filtros foram transferidos para novos tubos de coleta e centrifugados por 25 minutos a 14.000 g e 20 °C e ao filtrado foi adicionado 30 μ L de TFA 4% para interromper a digestão. Em seguida, as amostras foram secadas utilizando *SpeedVac*.

Ressuspensão das amostras: As amostras foram ressuspensas em 100 μ L de ácido fórmico 0,1% e incubadas a temperatura ambiente durante a noite a 600 RPM. No dia seguinte, as amostras foram centrifugadas a 14.000 g por 30 minutos a 4 °C e o sobrenadante foi transferido para um novo tubo.

5.1.4. Análise por espectrometria de massas

As análises foram realizadas em um sistema Easy-nanoLC 1200 (Thermo Fisher Scientific Corp., Waltham, MA, USA) acoplado a um instrumento Orbitrap Fusion Lumos contendo uma fonte nanospray (Thermo Fisher Scientific Corp., Waltham, MA, USA). Os solventes do Nano-LC foram água com 0,1% de ácido fórmico (A) e H₂O:ACN (20:80, v/v) com 0,1% de

ácido fórmico (B). Cada amostra (4 μ L) foi carregada em uma pré-coluna do tipo trap (Acclaim PepMap 100, C18, 3 μ m, 75 μ m \times 2 cm, nanoViper, Thermo Scientific) e lavada com 20 μ L de solvente (A) numa pressão constante (500 bar). Depois disso, a amostra foi eluída para a coluna do Nano-LC (Acclaim PepMap RSLC, C18, 2 μ m, 75 μ m \times 15 cm, nanoViper, Thermo Scientific) usando um fluxo de 300 nL/min. Um gradiente linear de 5% a 28% de (B) em 80 minutos foi seguido de um gradiente linear de 28 a 40% em dez minutos. Então, a porcentagem de solvente B foi aumentada de 40% para 95% em 2 minutos, e a coluna foi lavada por doze minutos nessa proporção de solvente. As amostras foram analisadas em um espectrômetro de massa Orbitrap Fusion Lumos (Thermo Scientific, Bremen, Alemanha) usando uma fonte de íons nanospray Flex NG (Thermo Scientific, Bremen, Alemanha) e operando no modo ESI positivo com temperatura capilar a 300°C. Os dados foram adquiridos no analisador Orbitrap usando um *scan* MS1 seguido de *scans* MS2 dependentes de dados num ciclo de 3 segundos. Os íons precursores foram fragmentados por HCD (*higher energy collision dissociation*) com uma energia de colisão normalizada de 30%. A resolução do modo MS1 foi 120.000 (a *m/z* 200), alvo AGC ajustado para 500.000, com a faixa de massa/carga monitorada entre 350 e 1550. O *scan* MS1 foi seguido por MS2 dependente de dados com resolução de 30.000 (em *m/z* 200), tempo máximo de preenchimento de 54 ms e janela de isolamento de 1,2 *m/z*.

5.1.5. Busca das proteínas e análise dos dados da proteômica de *shotgun*. Os arquivos gerados pelo espectrômetro de massas (arquivos *raw*) foram processados no software MaxQuant (TYANOVA; TEMU; COX, 2016). A busca dos espectros de MS/MS foi realizada pelo algoritmo Andromeda contra o banco de dados de proteínas de camundongos do Uniprot. A tripsina foi selecionada como enzima específica utilizada na digestão, com um máximo de 2 clivagens perdidas. Para normalização dos dados, comparação dos perfis de abundância das proteínas de retinas retinopáticas em relação às retinas dos grupos controle, e para uma quantificação *label-free* das proteínas identificadas, foi utilizado o algoritmo LFQ, disponível no MaxQuant. As análises das proteínas foram realizadas nos softwares Perseus. Inicialmente, os arquivos das proteínas foram carregados no Perseus (versão 1.6.15.0) e então os dados foram filtrados a partir de possíveis contaminantes, proteínas identificadas apenas com base em peptídeos modificados e de sequências identificadas no banco reverso. Em seguida, os valores foram transformados em log₂, nesse passo, aqueles valores apresentados como “0” – ausência de expressão ou detecção – foram convertidos em valores perdidos (*missing values* em experimentos LC-MS/MS – identificados com a expressão “NaN”). A

partir desses dados, o software Perseus foi utilizado para obter a Análise de Componente Principal (PCA), volcano e heatmap. Para PCA, foi realizado uma filtragem de 100% dos valores válidos, ou seja, sem os *missing values*. Para a análise das proteínas diferencialmente abundantes, os grupos foram nomeados e o tratamento dos *missing values* foi realizado com uma filtragem de pelo menos 60% de valores válidos em cada grupo, e os valores remanescentes de *missing values* foram imputados (*imputation width*= 0,3; *shift*= 1,8) para que esses valores fossem substituídos por intensidades baixas em uma distribuição normal. Para obter o volcano plot foi realizado um Teste-T, considerando FDR<0,05 e o grupo das amostras fisiológicas como referência ao grupo patológico. Para o heatmap, foram aplicados Student's T-test e Benjamini-Hochberg com FDR: 0.05, em seguida os dados foram normalizados utilizando o Z-Score e foi feita uma clusterização para a criação do heatmap. As proteínas diferencialmente expressas foram submetidas à plataforma STRING 11.5 (<http://https://string-db.org/>) para a construção de uma rede de interação proteína-proteína, utilizando confiança alta (score maior que 0,4). Por fim, para a identificação dos processos biológicos, funções moleculares e componentes celulares foi utilizado ferramenta GO (*Gene Ontology*) por meio do Software ShinyGO.

5.2. RESULTADOS PRÉVIOS

Para determinar o perfil proteômico das retinas de camundongos com angiogênese patológica, nós utilizamos o modelo OIR, conforme descrito em materiais e métodos. Resumidamente, camundongos com sete dias de idade (dia 7 pós-natal, P7) e suas mães lactantes foram submetidos a 75% de oxigênio por cinco dias. Quando os camundongos retornam aos níveis de oxigênio atmosférico, agora em P12, a retina mal vascularizada experimenta uma forte condição de hipóxia, o que leva ao aumento da expressão de VEGF além dos níveis fisiológicos (MICHALOSKI et al., 2016; SMITH et al., 1994). O resultado é o crescimento anormal dos vasos sanguíneos na retina periférica com a formação de tufos neovasculares, juntamente com uma área central de vaso-obliteração, causada pela exposição à hiperóxia nos estágios iniciais do modelo. A visualização por imunofluorescência confirmou a retinopatia nas retinas do modelo OIR (**Fig. 3**)

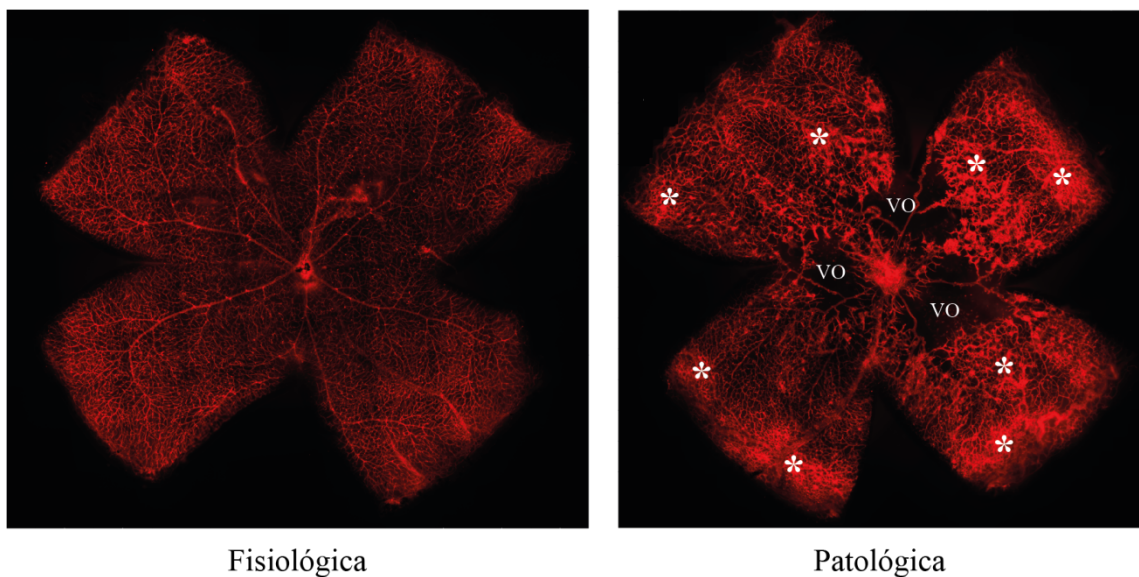


Figura 3. O modelo OIR e as retinas usadas para a determinação do proteoma. Retinas de camundongos (P17) em condições fisiológicas (esquerda) e retinopáticas (direita, modelo OIR). As retinas foram tratadas com isolectina-B4 conjugada com Alexa-594 e visualizadas por microscopia de imunofluorescência indireta. As regiões de tufos vasculares (*) e vaso-obliteração (VO) confirmam a presença de retinopatia nas retinas do modelo OIR.

Para realizar o estudo do proteoma, as retinas dos animais submetidos ao modelo OIR ou não, foram cuidadosamente dissecadas e mantidas a -80°C , até o momento da análise, na presença de inibidores de protease para prevenir a degradação indesejada das proteínas das nossas amostras. O estudo do proteoma foi realizado, ainda, nos diferentes estágios de desenvolvimento da retina e do modelo OIR: (1) durante a regressão dos vasos após

exposição à hiperóxia por cinco dias (R12); doze horas após a saída do estado de hiperóxia (R12.5) e durante a neovascularização, após o retorno à normóxia por 3 e 5 dias, R15 e R17, respectivamente (**Figs. 2 e 4**). No caso das retinas dos animais controle (angiogênese fisiológicas), as amostras foram coletadas nos dias P12, P15 e P17.

Após a coleta das amostras, as retinas foram tratadas com tripsina para fragmentar as proteínas nos seus respectivos peptídeos. A tripsina foi escolhida porque é uma protease que cliva proteínas em resíduos básicos (lisina e arginina), que podem ser protonados em condições ácidas. Uma vez fragmentadas as proteínas, as amostras foram analisadas empregando-se um sistema de cromatografia líquida (EASY nLC-1200) acoplado a um espectrômetro de massas de alta resolução (Orbitrap Fusion Lumos). Os diversos peptídeos foram ionizados, suas massas detectadas e reportadas na forma de espectro. No primeiro estágio de MS, cada pico no espectro representou a relação m/z de um dado íon (peptídeo). No segundo estágio, peptídeos selecionados do primeiro foram fragmentados pelo método de dissociação por colisão de alta energia (HCD – *higher energy collision dissociation*), resultando num segundo espectro do peptídeo, onde cada pico representara um fragmento do peptídeo. O passo seguinte foi a identificação da sequência primária dos peptídeos baseado no padrão dos fragmentos obtidos (MS/MS).

Em função do elevado número de espectros produzidos no nLC-MS/MS, é essencial o uso de ferramentas computacionais para a atribuição de uma sequência peptídica de cada espectro. Nesse sentido, os dados gerados pelo espectrômetro de massas foram processados pelo software MaxQuant, que utiliza o algoritmo Andromeda e o banco de dados Uniprot (acesso em fevereiro de 2022) para associar uma proteína para um determinado conjunto de peptídeos dos espectros analisados. Ao todo, foram identificadas 2.806 proteínas nos sete grupos das amostras (fisiológicos: P12, P15 e P17; patológicos: R12, R12.5, R15 e R17).

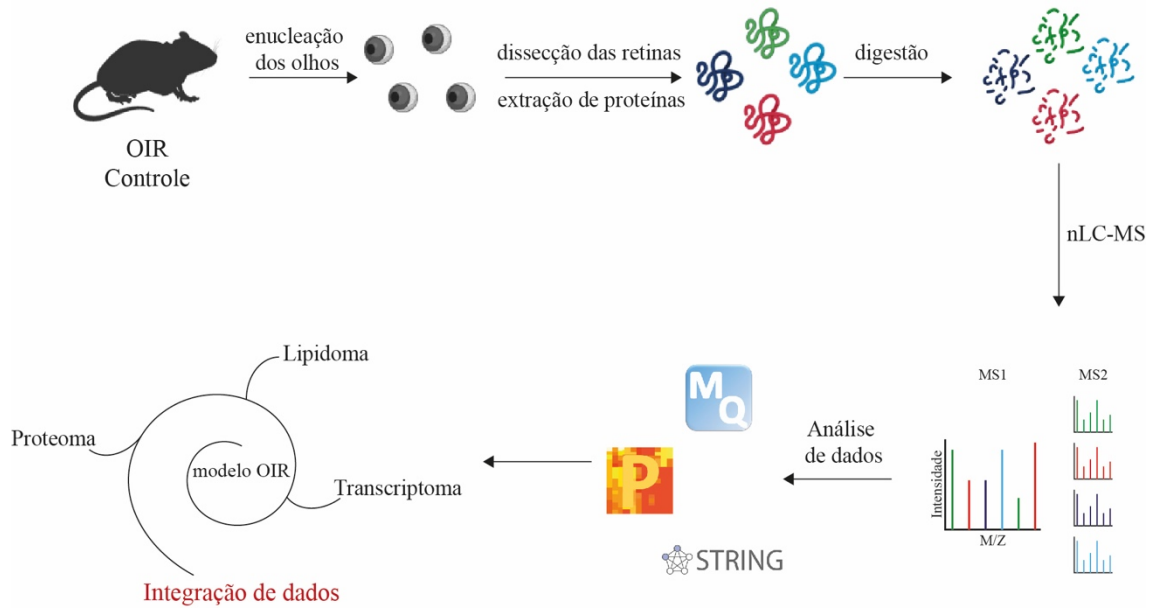


Figura 4. Workflow do nosso estudo de proteômica. Retinas de camundongos controles (P) e camundongos OIR (R) foram dissecadas, preparadas e processadas para análise proteômica e de bioinformática.

5.2.1. Variáveis que influenciam o proteoma

Uma vez obtido o conjunto de proteínas, procedemos para uma análise de componentes principais (PCA) para identificar as principais variáveis que influenciam nossos dados. A análise de PCA foi realizada com os dados de quantificação (*LFQ intensity*) das proteínas presentes em todas as amostras de um dado grupo (P12, P15 e P17; e R12, R12.5, R15 e R17); ou seja, com 615 proteínas no grupo OIR e 688 no grupo controle (angiogênese fisiológica).

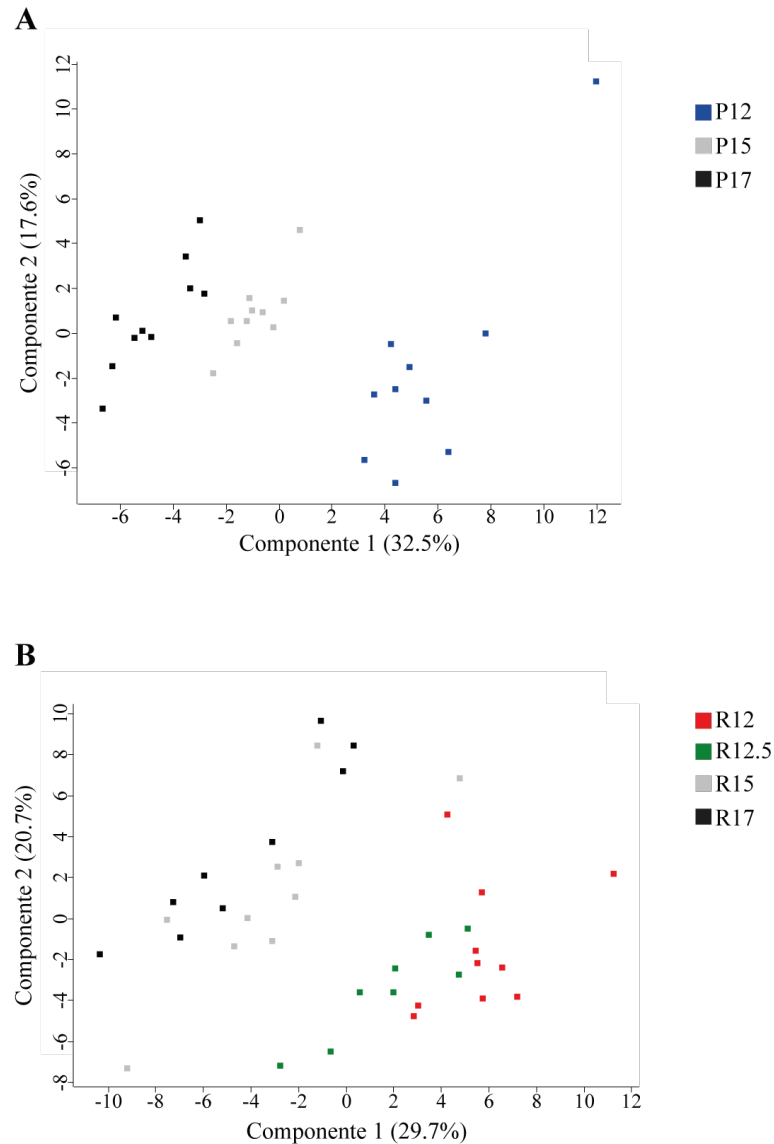


Figura 5. Correlação entre as amostras do proteoma. Análise de componentes principais (PCA) com 615 proteínas no grupo OIR (R) e 688 no grupo controle (angiogênese fisiológica - P). A) amostras dos grupos fisiológicos (P12, P15 e P17). B) Amostras dos grupos retinopáticos (R12, R12.5, R15 e R17).

A análise de PCA mostrou que há uma boa correlação das diferentes réplicas das amostras de retinas fisiológicas, onde observamos uma clara separação entre os grupos P12, P15 e P17 (**Fig. 5A**). Porém, essa mesma separação não é tão clara nas amostras do grupo OIR (**Fig. 5B**). Observa-se que as amostras se separam em dois agrupamentos, um contendo as amostras dos dias R12 e R12.5 e outro contendo as amostras dos grupos R15 e R17. Tal fato pode ser explicado pela semelhança do estado patológico, pois R12 e R12.5 estão no início do processo de angiogênese patológica e R15 e R17 se encontram no pico desse

estágio. Como a expressão gênica precede a síntese de proteína, que é um processo mais lento, acreditamos que o período de 12h não permite uma síntese adequada de proteínas suficiente para mudar o proteoma destas amostras. Por outro lado, embora haja uma separação discreta entre as amostras dos dias R15 e R17, ela não é significativa. Em resumo, a análise de PCA indicou que há uma boa correlação dos dados do proteoma das nossas réplicas biológicas, tanto das amostras obtidas dos animais mantidos em condições fisiológicas, como dos animais do modelo OIR, sugerindo ainda que a angiogênese patológica está alterando a produção de proteínas na retinopatia (**Fig. 6**).

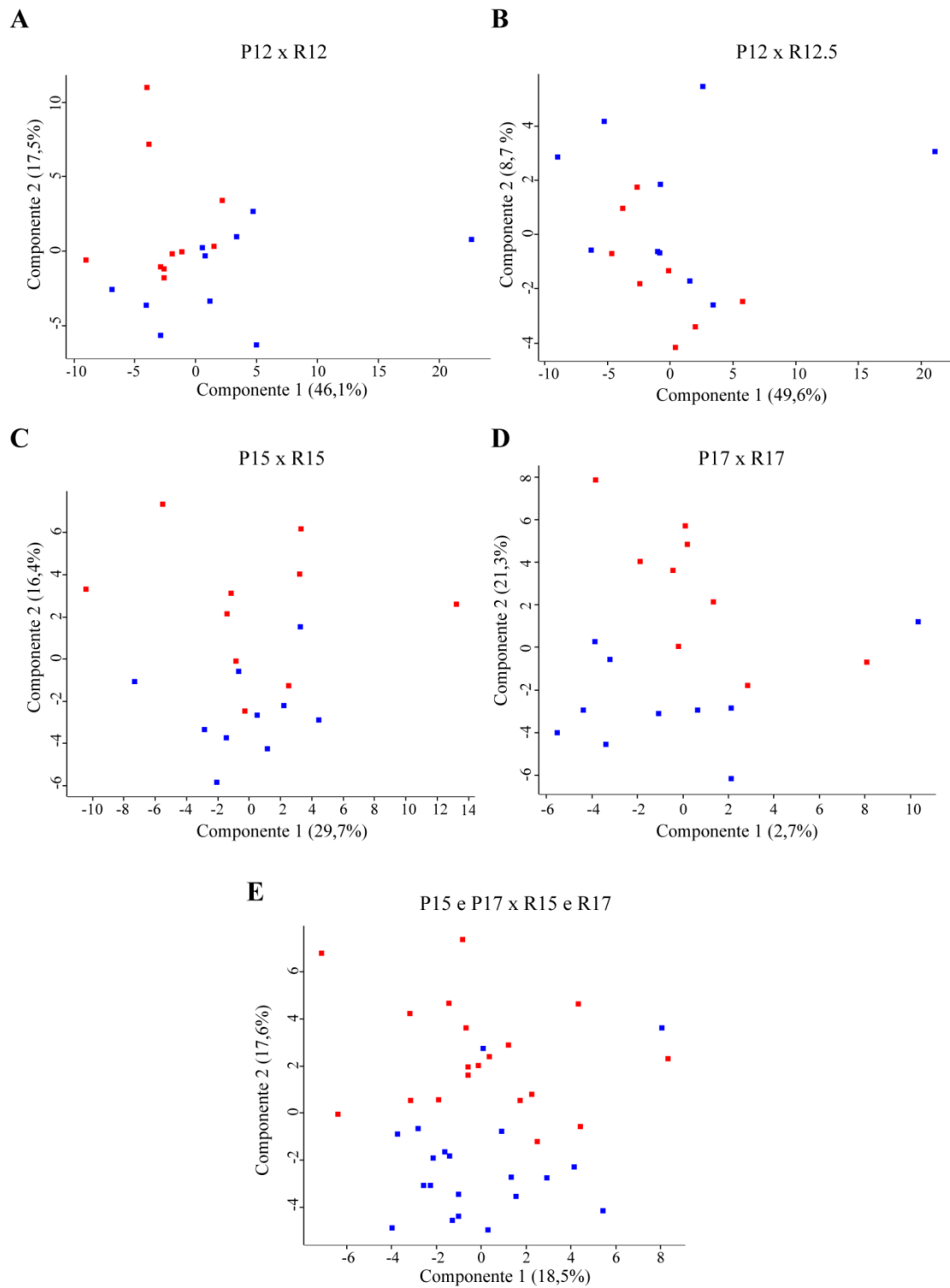


Figura 6. A angiogênese patológica altera o proteoma da retina. Análise de componentes principais dos grupos das amostras retinopáticas e fisiológicas. A) amostras dos grupos P12 x R12. B) amostras dos grupos P12 x R12.5. C) amostras dos grupos P15 x R15. D) amostras dos grupos P17 x R17. E) amostras dos grupos P15 e P17 x R15 e R17. Em vermelho: amostras retinopáticas e em azul: amostras fisiológicas.

5.2.2. Identificação de proteínas diferencialmente produzidas na angiogênese fisiológica e patológica

Uma vez confirmada a influência do modelo OIR na produção de proteínas na retina, e com o objetivo de estudar a dinâmica de síntese das diferentes proteínas da retina ao longo da retinopatia, realizamos a identificação e quantificação das proteínas com diferenças significativas de abundância entre a condição fisiológica e a patológica (teste t, FDR (*false discovery rate*) < 0,05) (**Fig. 7**).

Para esta análise, nós levamos em conta os resultados das análises de PCA. Por exemplo, os grupos R15 e R17 foram combinados, assim como P15 e P17, em busca de proteínas produzidas diferencialmente durante a retinopatia (**Fig. 7A**). Fizemos também uma comparação entre as amostras do grupo P12 e R12, o que permitiu indicar proteínas cujas produções foram afetadas pela hiperóxia (cinco dias expostos a 75% pO₂) (**Fig. 7B**). Finalmente, realizamos uma análise comparativa entre as proteínas presentes nas amostras R12 e R12.5 para identificar as proteínas alteradas pela variação na pressão de oxigênio (**Fig. 7C**).

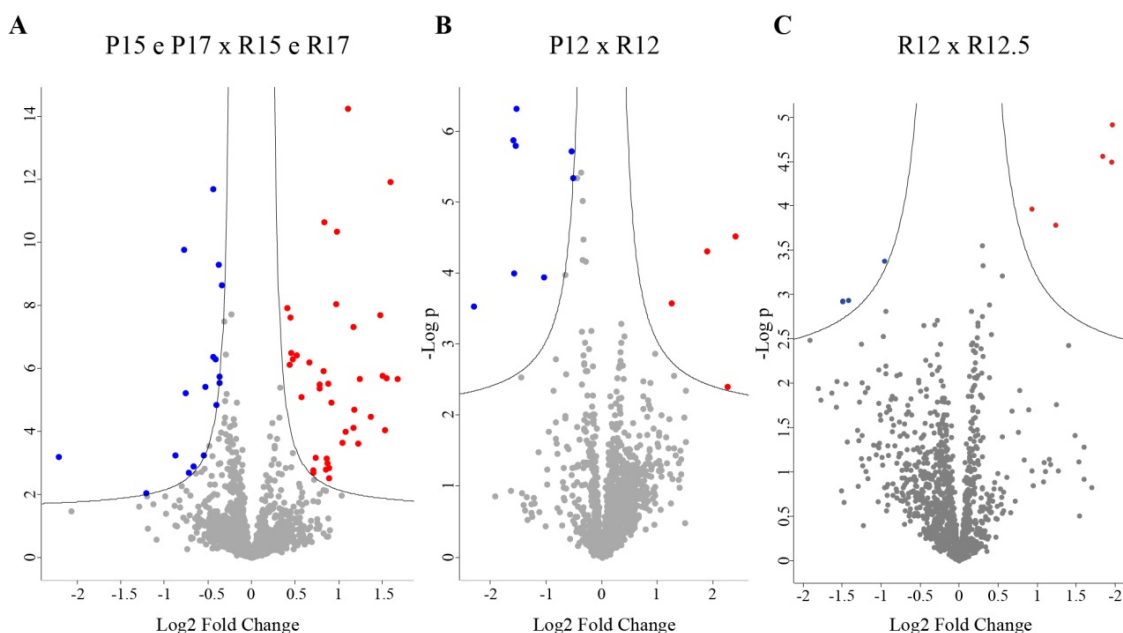


Figura 7: Identificação de proteínas mais abundantes na retinopatia. *Volcano plot* indicando os perfis de abundância relativa (log₂ FC) e a significância (*p*-valor) entre as amostras fisiológica e patológica. A) Análise das amostras dos grupos retinopáticos R15 e R17 em relação às amostras dos

grupos fisiológicos P15 e P17. B) Análise dos grupos P12 e R12. C) Análise dos grupos R12 e R12.5. Pontos vermelhos: proteínas mais abundantes, pontos azuis: proteínas menos abundantes, $p \leq 0.05$.

Quatro proteínas apresentaram produção aumentada pela hiperóxia: Crocc, Lsm4, Fbl e Myef2; e sete proteínas apresentaram produção reduzida (**Tabela 1**). Em relação à comparação das amostras dos grupos do R12.5, não apresentou nenhuma proteína significativamente mais ou menos abundante em relação ao grupo controle (P12). Isso pode ser justificado pelo fato de que o efeito de hipóxia relativa, causado pela remoção dos animais 12 horas após a saída da câmara com alto nível de oxigênio, disparou uma resposta e, que, em razão da síntese proteica ser um processo mais demorado, não foi possível detectar a tradução dos genes transcritos nesse processo. Outra hipótese que vale ressaltar é que pode ter ocorrido degradação, modificações pós-traducionais ou ubiquitinação de proteínas, dificultando a sua detecção; finalmente, a perda de peptídeos durante a cromatografia ou a formação espectros de massas inadequados também podem explicar esses resultados (ARMIROTTI; DAMONTE, 2010). Na análise de R12.5 e R12, proteínas do plasma que estão em abundância, dentre elas, a Apoa1.

Tabela 1. Lista das proteínas com diferença de abundância significativa após exposição à hiperóxia (R12).

Proteína	Gene	Uniprot	Fold Change
U6 snRNA-associated Sm-like protein LSm4	Lsm4	D3YTP8	5.271
Myelin expression factor 2	Myef2	A2ATP6	4.775
rRNA 2-O-methyltransferase fibrillarin	Fbl	P35550	3.700
Rootletin	Crocc	Q8CJ40	2.366
Fructose-bisphosphate aldolase	Aldoa	Q5FWB7	0.700
Fructose-bisphosphate aldolase C	Aldoc	P05063	0.689
Filamin-B	Flnb	Q80X90	0.486
Beta-globin	Hbbt1	A8DUP0	0.346
Annexin A2	Anxa2	P07356	0.335
Alpha globin 1	Hba-a1	Q91VB8	0.331
Odorant-binding protein 1b	Obp1b	A2AEP0	0.203

Quanto às amostras no pico de angiogênese patológica (R15 e R17), o número de proteínas foi maior: 55 proteínas com diferença significativa de abundância. Dessas, 38 proteínas com maior abundância e 17 com menor abundância significativa em relação ao grupo controle P15 e P17 (**Fig. 8**). Um fato interessante é que algumas proteínas, como a Anxa2 (Anexina 2) e a Flnb (Filamina B), apresentaram valores de menor abundância nas

retinas retinopáticas no ponto P12 e valores altos no pico de angiogênese (P15 e P17). A proteína Anxa2 está envolvida em vários processos celulares essenciais, como proliferação celular, adesão celular, motilidade celular, angiogênese e endocitose. Essa proteína é abundantemente expressa em vários tipos de tumor, outra doença dependente da angiogênese, e, portanto, é proposta como um marcador potencial para cânceres. (BHARADWAJ et al., 2013; LOKMAN et al., 2011; WANG et al., 2019). Por sua vez, a Flnb é conhecida por regular o início da migração celular e também desempenha um papel fundamental na motilidade das células endoteliais e no desenvolvimento vascular (BALDASSARRE et al., 2009; VALLE-PE et al., 2010).

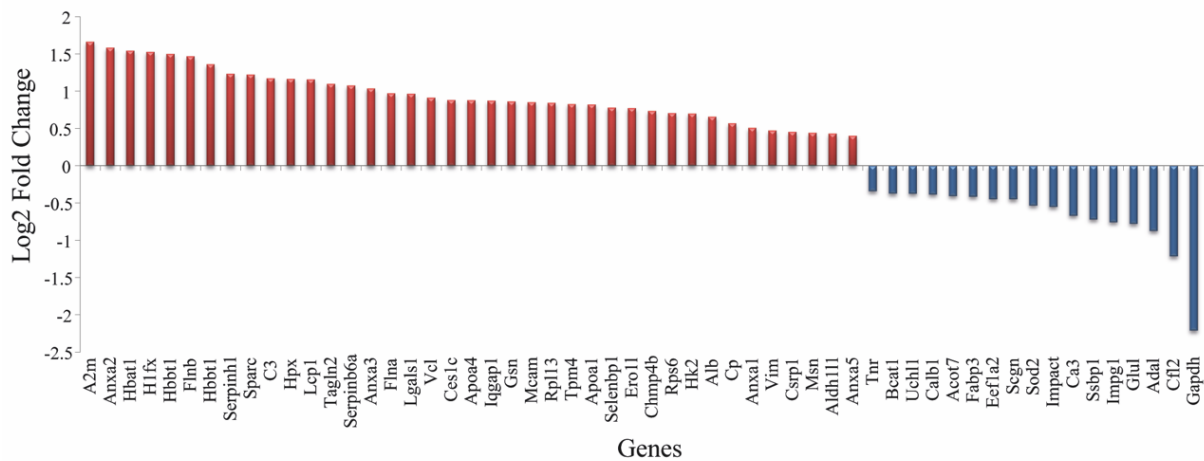


Figura 8. Proteínas com diferença significativa de abundância no pico da retinopatia. Gráfico com valores de Log₂ Fold Change das proteínas estatisticamente mais e menos abundantes do grupo retinopático (R15 e R17) em relação ao grupo controle (P15 e P17).

Com essa análise foi possível observar que ocorre um remodelamento proteico importante entre o início da angiogênese patológica e o seu pico e, que, o modelo OIR, de fato, mimetiza uma condição de angiogênese patológica, visto que a nossa identificação de proteínas apresenta marcadores de doenças dependentes de angiogênese patológica. Os valores de Fold-change dessas e de outras proteínas estão apresentados nas tabelas 1 e 2.

Tabela 2. Lista das proteínas com diferença de abundância significativa no pico de angiogênese patológica (R15 e R17).

Proteína	Gene	Uniprot	Fold Change
Alpha-2-macroglobulin	A2m	Q61838	3.173
Annexin A2	Anxa2	Q9CZI7	3.001
Hemoglobin subunit alpha	Hbat1	Q91VB8	2.918
H1 histone family, member X	H1fx	Q80ZM5	2.885
Beta-globin	Hbbt1	A8DUP0	2.830

Filamin-B	Flnb	Q80X90	2.768
Beta-globin	Hbbt1	A8DUP7	2.571
Serpin H1	Serpinh1	Q8BVU9	2.351
SPARC	Sparc	Q5NCU4	2.334
Complement C3	C3	P01027	2.256
Hemopexin	Hpx	Q91X72	2.244
Plastin-2	Lcp1	Q3U9M7	2.235
Transgelin-2	Tagln2	Q9WVA4	2.144
Serpinb6a protein	Serpinb6a	Q4FJQ6	2.111
Annexin A3	Anxa3	Q8C1X9	2.056
Filamin-A	Flna	B7FAV1	1.963
Galectin-1	Lgals1	P16045	1.955
Vinculin	Vcl	Q64727	1.885
Carboxylesterase 1C	Ces1c	P23953	1.843
Apolipoprotein A-IV	Apoa4	P06728	1.841
Ras GTPase-activating-like protein IQGAP1	Iqgap1	Q9JKF1	1.834
Gelsolin	Gsn	Q6PAC1	1.821
Cell surface glycoprotein MUC18	Mcam	Q8R2Y2	1.807
60S ribosomal protein L13	Rpl13	Q5RKP3	1.797
Tropomyosin alpha-4 chain	Tpm4	Q6IRU2	1.775
Apolipoprotein A-I	Apoa1	Q3V2G1	1.768
Selenium-binding protein 1	Selenbp1	P17563	1.717
ERO1-like protein alpha	Ero1l	Q4FK57	1.710
Charged multivesicular body protein 4b	Chmp4b	Q9D8B3	1.665
40S ribosomal protein S6	Rps6	Q8BT09	1.633
Hexokinase-2	Hk2	E9Q5B5	1.626
Serum albumin	Alb	P07724	1.579
Ceruloplasmin	Cp	G3X9T8	1.486
Annexin A1	Anxa1	Q4FJV4	1.425
Vimentin	Vim	P20152	1.387
Cysteine and glycine-rich protein 1	Csrp1	Q4FJX4	1.370
Moesin	Msn	P26041	1.358
Cytosolic 10-formyltetrahydrofolate dehydrogenase	Aldh11l	Q8R0Y6	1.348
Annexin A5	Anxa5	P48036	1.322
Tenascin-R	Tnr	Q8BYI9	0.790
Branched-chain-amino-acid aminotransferase	Bcat1	Q3TJN1	0.773
Ubiquitin carboxyl-terminal hydrolase isozyme L1	Uchl1	Q9R0P9	0.772
Calbindin	Calb1	P12658	0.766
Cytosolic acyl coenzyme A thioester hydrolase	Acot7	E9PYH2	0.755
Fatty acid-binding protein, heart	Fabp3	Q5EBJ0	0.751
Elongation factor 1-alpha 2	Eef1a2	P62631	0.733
Secretagogin	Scgn	Q91WD9	0.733
Superoxide dismutase	Sod2	Q4FJX9	0.691
Protein IMPACT	Impact	O55091	0.683
Carbonic anhydrase 3	Ca3	P16015	0.629
Single-stranded DNA-binding protein	Ssbp1	Q8R2K3	0.607
Interphotoreceptor matrix proteoglycan 1	Impg1	Q8R1W8	0.592
Glutamine synthetase	Glul	P15105	0.584
Adenosine deaminase-like protein	Adal	Q80SY6	0.546
Cofilin-2	Cfl2	P45591	0.431
Glyceraldehyde-3-phosphate dehydrogenase	Gapdh	S4R1W8	0.216

Outra análise importante é a de correlação entre os dados do proteoma e do transcriptoma. Nesse sentido, partimos para uma comparação dos dados de proteoma das amostras dos grupos R15 e R17 com os dados de transcriptoma gerados pelo nosso grupo. Eles apresentaram perfis de transcrição e tradução simultâneos. Para isso, selecionamos as 55 proteínas com produção alterada no proteoma e comparamos com os valores de variação de expressão no transcriptoma. De maneira geral, observamos uma boa correlação entre os dados, com um coeficiente de correlação de Pearson com o valor de $R = 0,5561$ (**Fig.9**). Apenas oito proteínas não apresentaram os valores semelhantes aos dados do transcriptoma. Isso pode ser explicado, por exemplo, pelo efeito de RNAs regulatórios (miRNA), embora estudos futuros sejam necessários para confirmar esta hipótese.

É interessante observar que, das 55 proteínas com produção diferencial, sete delas se encontram na nossa lista de transcritos de maior abundância: A2m, Anxa2, Lcp1, Tagln2, Mcam, Tpm4 e Msn. Isso sugere que as mesmas possam ser alvos terapêuticos e diagnósticos interessantes para as doenças dependentes da angiogênese.

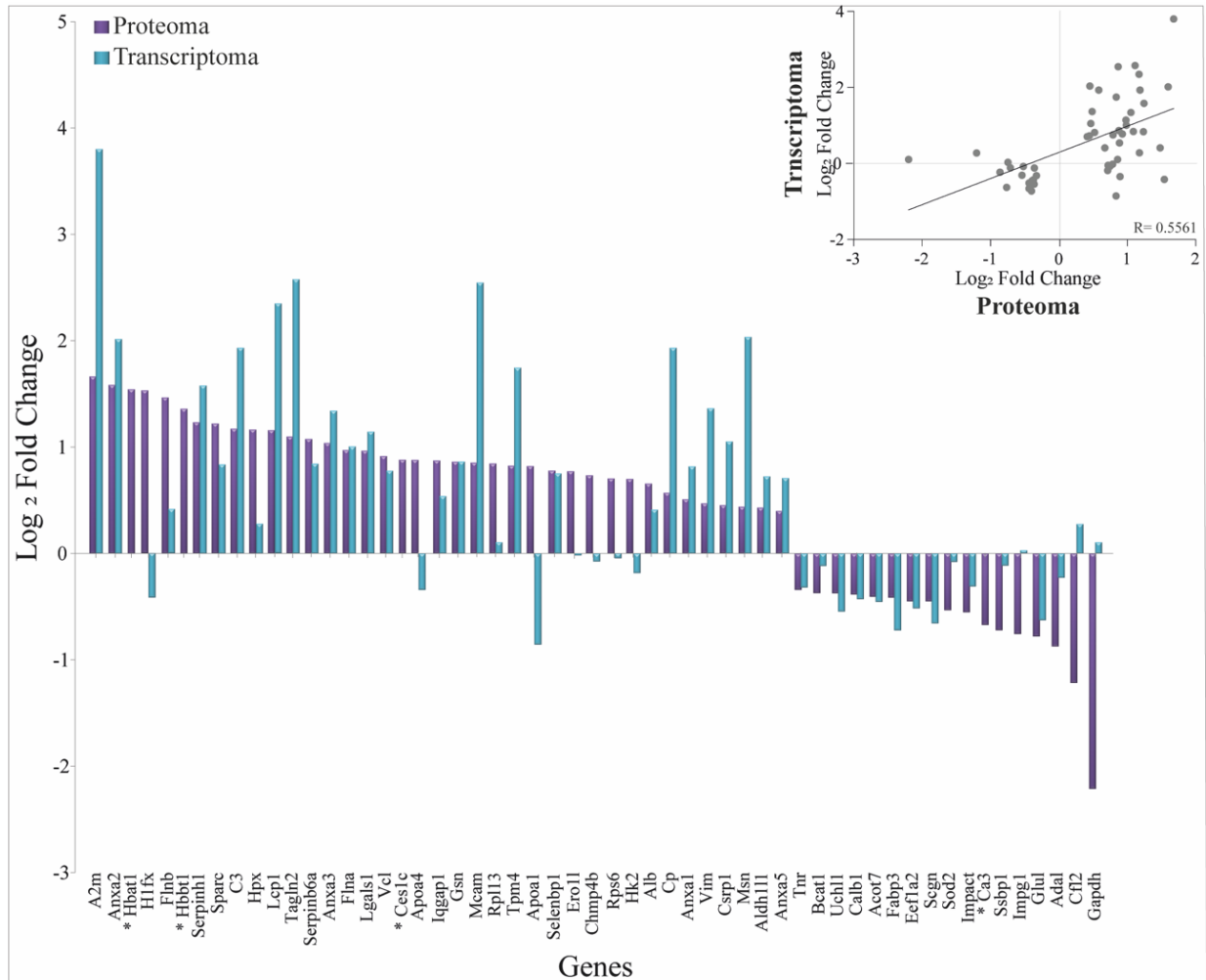


Figura 9. Dinâmica do transcrito de mRNA e sua relação com alterações no proteoma. Gráfico correlacionando as variações da expressão de mRNA e da produção de proteínas (Log₂ fold change) para as proteínas com maior ou menor variação no proteoma da retina (ver Figs. 7, 8 e Tabela-2). O coeficiente da correlação de Pearson foi igual a 0,5561 e p -value < 0,0001. As proteínas com * significa que não estão presentes no nosso estudo de transcriptoma.

5.2.3. Processos biológicos enriquecidos na retinopatia

Uma vez identificadas proteínas cujas produções foram alteradas pela retinopatia, podemos estudar os processos biológicos das quais elas fazem parte. Como já dito anteriormente, uma questão importante na retinopatia é a identificação de novos alvos terapêuticos. Entender os processos biológicos das quais essas proteínas participam é uma etapa importante para selecionar novos alvos moleculares. Vale lembrar que o aumento na expressão gênica nem sempre resulta em aumento de produção de proteína, uma vez que podem ocorrer várias interferências no meio do caminho, uma delas é a ação dos MicroRNAs (miRNAs). Os miRNAs são moléculas regulatórias importantes que podem inibir a tradução

do mRNA, afetando o proteoma, ou acelerar a degradação do mRNA (GEBERT; MACRAE, 2019; HA; KIM, 2014). Porém, como observamos anteriormente (Fig. 9), para a maioria das proteínas identificadas no nosso estudo, observamos uma boa correlação entre alteração na expressão gênica e abundância da proteína.

Para esta análise, consideramos as médias dos valores de intensidade (LFQ *intensity*) significativamente diferentes entre as amostras fisiológicas e patológicas. As proteínas com abundâncias relativas alteradas nas retinas fisiológicas (P15 e P17) e patológicas (R15 e R17) (Student's T-test e Benjamini-Hochberg, FDR<0,05), foram identificadas. Observamos um conjunto de 141 proteínas com diferença na abundância, que puderam ser subdividas em dois clusters: um de alta abundância na OIR e outro de baixa abundância (Fig. 10).

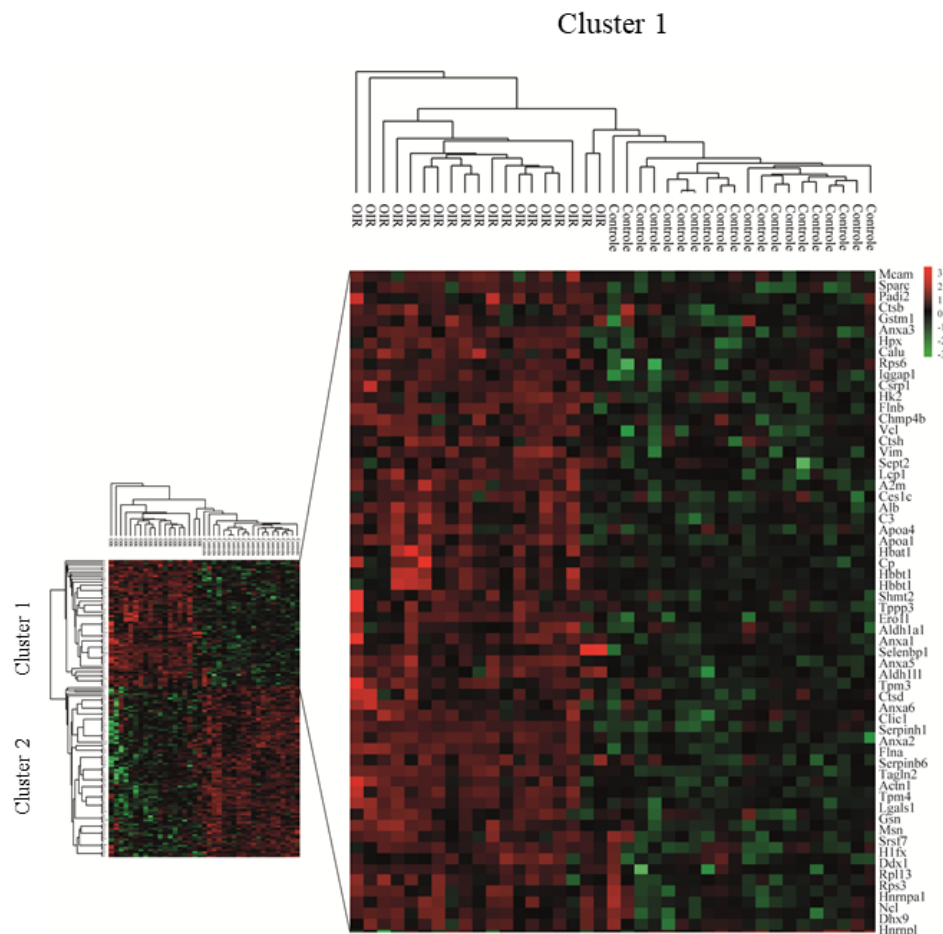


Figura 10. As proteínas presentes no pico de angiogênese foram claramente separadas em dois clusters. *Heatmap* indicando a abundância relativa das proteínas nas retinas OIR (R15 e R17) em comparação com os controles (P15 e P17). Essas proteínas estão separadas em dois clusters. Em destaque: cluster que apresenta as proteínas mais abundantes no grupo retinopático. Em vermelho: proteínas mais abundantes na angiogênese patológica e em verde as proteínas menos abundantes (Student's T-test e Benjamini-Hochberg, FDR<0,05).

Como o nosso interesse inicial é o de avaliar potenciais alvos terapêuticos e diagnósticos, vamos concentrar as análises no primeiro cluster, de proteínas mais abundantes no modelo OIR. A fim de investigar os processos em que as proteínas mais abundantes na retinopatia da análise acima estão envolvidas, realizamos a identificação das principais redes de interações utilizando o Software String. Para identificar os processos biológicos, funções moleculares e componentes celulares que essas proteínas estão envolvidas, utilizamos a ferramenta GO (*Gene Ontology*) por meio do Software ShinyGO.



Figura 11. Rede de interações proteína-proteína das proteínas mais abundantes das amostras retinopáticas. As redes de interação das proteínas estão representadas pelos nós, que correspondem às proteínas e pelas as linhas, que representam as evidências de associações.

Com a ferramenta do String, observamos interações de 61 proteínas mais abundantes no grupo retinopático, que foram divididas em 7 clusters (**Fig. 11**). Dois clusters se destacam pelo número de proteínas: o cluster-1 tem a presença de proteínas relacionadas às vias de lipoproteínas, colesterol, quilomicrons e triacilglicerol, ou seja, corrobora com o nosso estudo do lipidoma, apresentado no capítulo 2, no qual apresentamos que a alta concentração de lipídios neutros está relacionada com a formação de gotículas lipídicas e com a ocorrência de transporte reverso de colesterol em retinas patológicas. Já o cluster-2 contém proteínas relacionadas à junção aderente, interação entre célula e matriz extracelular e à formação do citoesqueleto. Interpretamos isso como proteínas importantes para migração de células endoteliais, e remodelamento dos novos vasos sendo formados, com deposição de nova matriz extracelular e formação de junções entre as células vasculares.

No cluster-3 estão presentes três proteínas da família das anexinas, além de *Lgals1*, *Mcam* e *Vim*. As anexinas são uma família composta por doze proteínas, se ligam a fosfolipídeos da membrana e são dependentes de cálcio. De acordo com sua distribuição tecidual distinta e localização subcelular, as anexinas têm sido funcionalmente implicadas em uma variedade de processos biológicos relevantes para condições fisiológicas e patológicas (PRIETO-FERNÁNDEZ et al., 2022). A desregulação dos padrões e funções de expressão da anexina foi revelada como uma característica comum em vários tipos de câncer, manifestando como potenciais biomarcadores e alvos moleculares para aplicação clínico, como já comentado anteriormente.

Proteínas envolvidas no processamento e *splincing* de RNA foram agrupadas no cluster-4 e proteínas ribossomais no cluster-5, indicando um processo ativo de síntese proteica. No cluster-6, estão as catepsinas B e D. As catepsinas são proteases lisossômicas que estão envolvidas em vários processos intra e extracelulares, como a remodelação da matriz extracelular, processamento de antígenos e apoptose (CONUS; SIMON, 2008; DROGA-MAZOVEC et al., 2008; VIZOVIŠEK; FONOVIC; TURK, 2019). Além disso, elas são os principais mediadores da degradação de proteínas no lisossomo e têm sido associadas a várias doenças neurodegenerativas, nas quais ocorre a formação de agregados e inclusões de proteínas tóxicas para as células (DROBANY et al., 2022). Vale lembrar que a retina é considerada uma extensão do sistema nervoso.

Por fim, no cluster-7 estão presentes duas proteínas envolvidas no metabolismo de um carbono (1C), *Aldh1l1* e *Shmt2*. A serina hidroximetiltransferase 2 (*Shmt2*) desempenha um

papel crítico no metabolismo da serina-glicina para conduzir a proliferação de células cancerígenas (LIU et al., 2021). O metabolismo de 1C é importante para a produção de nucleotídeos e duplicação do DNA, condizente com o processo de angiogênese. Como podemos notar, a maioria das proteínas identificadas nesse nosso estudo do proteoma de retinas retinopáticas está, de alguma forma, envolvida processos malignos, como o câncer ou em mecanismos que favorecem a formação e proliferação dessa doença.

Tabela 3: Relação dos clusters e suas respectivas proteínas.

Nome do cluster	Proteínas
Cluster 1	A2m, Alb, Apoa1, Apoa4, C3, Cp, Hbb-bs, Hpx Serpinh1, Sparc
Cluster 2	Actn1, Anxa5, Flna, Flnb, Gsn, Iqgap1, Msn, Tagln2, Tpm4, Vcl
Cluster 3	Anxa1, Anxa2, Anxa6, Lgals1, Mcam, Vim
Cluster 4	Ddx1, Dhx9, Hnrnpa1, Hnrnpl, Srsf7
Cluster 5	Ncl, Rpl13, Rps3, Rps6
Cluster 6	Ctsb, Ctsd Shmt2
Cluster 7	Aldh111, Shmt2

Para categorizar os clusters e identificar os processos biológicos, função molecular e componente celular com os quais eles se relacionam, realizamos uma análise de enriquecimento dos termos de anotação do *Gene Ontology* (GO) das proteínas mais abundantes do grupo retinopático (R15 e R17) (**Fig. 12**). Na categoria de processos biológicos, destacou-se: secreção de prolactina, processos de lipoproteínas, colesterol, triacilglicerol, fosfolipídeos, ácidos graxos e podossomos. Quanto às funções moleculares, observamos um maior enriquecimento das atividades inibitórias de lipases, atividades de helicase, transferência de esterol e colesterol, e ligação de: interleucina-8, subunidade catalítica de fosfatidilinositol 3-quinase, selênio, galactose, proteína S100 e receptor de apolipoproteína A-I. No que se refere aos componentes celulares, é possível observar que se destacam as proteínas relacionadas às partículas de lipoproteínas, quilomicrons e complexo inibidor de serina protease, novamente, compartilhando processos biológicos identificados no estudo do lipidoma (capítulo 2).

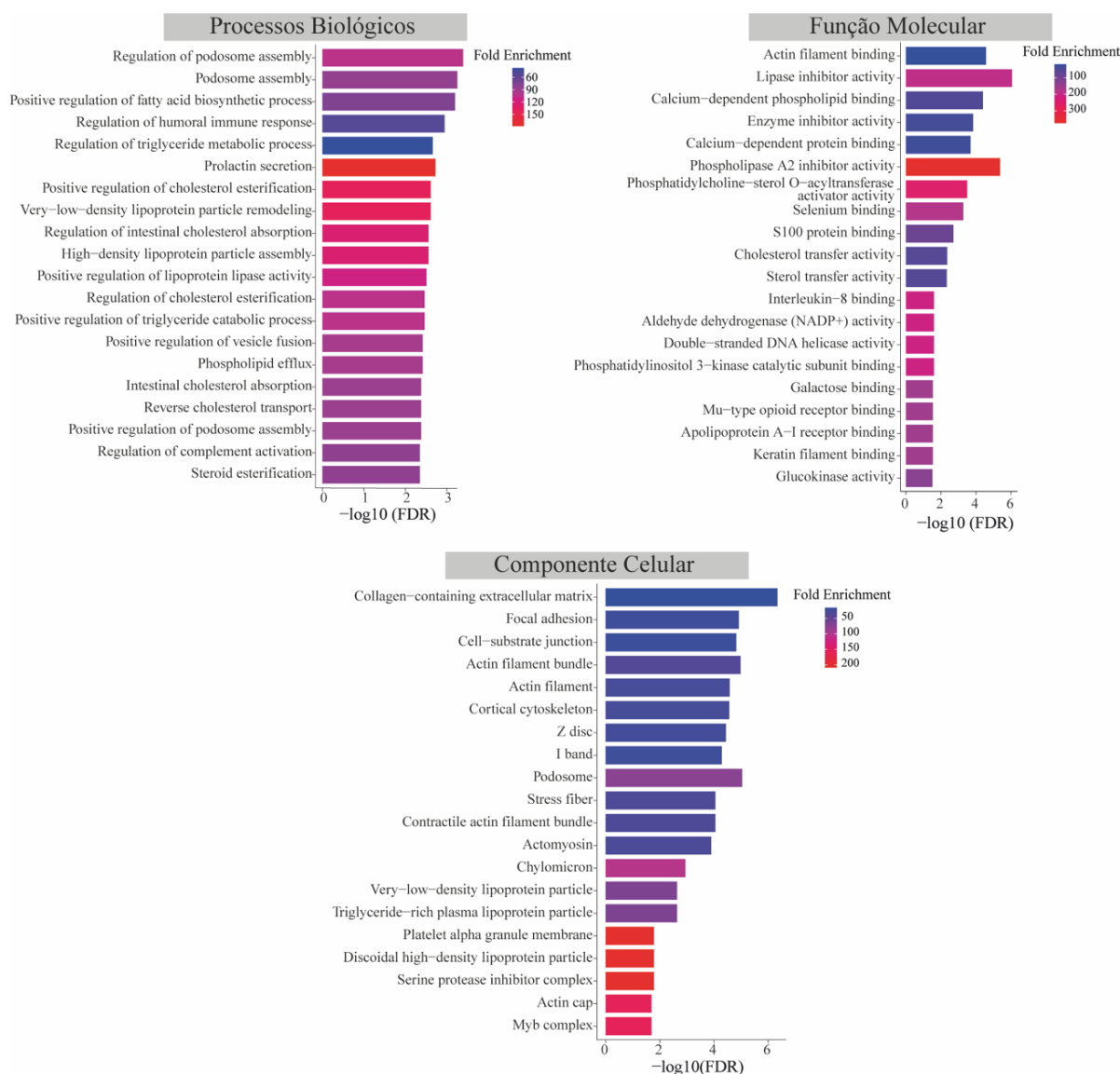


Figura 12. Processos biológicos associados com as alterações do proteoma da retinopatia. A análise do GO foi realizada com as proteínas mais abundantes do grupo retinopático (R15 e R17). As vias celulares, moleculares e processos biológicos estão ordenadas em ordem decrescente de número de proteínas, o eixo x indica valores de $-\log_{10}(\text{FDR})$ e as cores das barras estão de acordo com o enriquecimento.

5.2.4. Proteoma, lipidoma e transcriptoma convergem no metabolismo de gotículas de gordura

Outro aspecto relevante é que a nossa análise proteômica converge com a integração dos dados do transcriptoma e do lipidoma, apresentando proteínas relacionadas às vias de lipoproteínas, colesterol, quilomicrons e triacilglicerol. Dentre elas, as proteínas A2m, C3 e

Hpx apresentam valores significativos de FoldChange (**Tab.2**) e são marcadoras de partículas de HDL (*High Density Lipoproteins*).

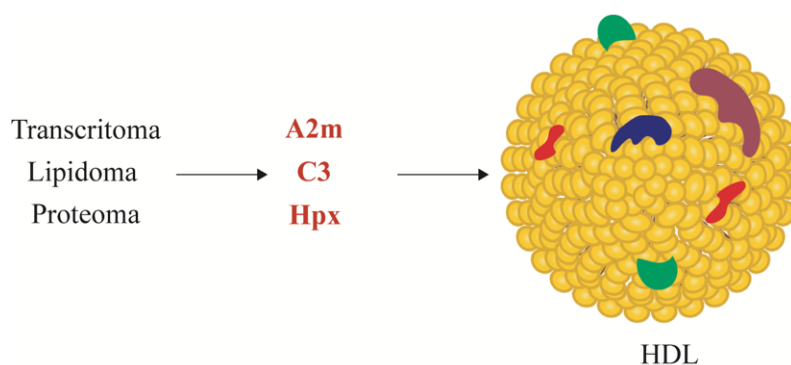


Figura 13. Proteínas importantes nos dados de integração da técnicas ômicas. Com a integração dos dados do transcriptoma, lipidoma e proteoma, as proteínas Alfa-2-macroglobulina (A2m), complemento C3 (C3) e hemopexina (Hpx), marcadoras de HDL, apresentam grande destaque.

5.3. DISCUSSÃO

As patologias associadas às mais diversas doenças com impacto na saúde humana, de forma geral, são frutos de alteração mensuráveis em processos biológicos. Desta forma, tecnologias de ômica, como as utilizadas nessa tese (transcriptômica, proteômica e lipidômica), podem ser ferramentas importantes para avaliar genes, lipídeos e proteínas que se associam a doenças específicas. No entanto, uma limitação considerável para esses estudos é obtenção de amostras humanas. Não é fácil ter acesso a amostras de retinas humanas. Além disso, a diversidade genética dos diferentes indivíduos (pacientes) também é um fator importante que afeta a variabilidade das amostras. Por isso, a utilização de modelos animais relevantes para uma dada doença, como o OIR, é, portanto, importante para ajudar a elucidar a biologia de sistemas da retina em um modelo de patologia. Camundongos são isogênicos, o que diminui a influência das variações genéticas entre as amostras; no modelo OIR, o início e fim do processo da angiogênese podem ser bem controlados, no tempo, e pela administrações (não invasiva) de oxigênio.

Nesse sentido, nos últimos anos, nosso grupo de pesquisa tem explorado esse modelo através dessas diferentes tecnologias, em busca de identificar novos marcadores da angiogênese patológica. Nosso primeiro estudo, o de transcriptômica (GUARISCHI-SOUSA et al., 2019), foi, portanto, um marco importante. Demonstramos que a expressão de mRNA na retina de camundongos do modelo OIR pôde ser utilizada de forma prognóstica para uma doença humana dependente da angiogênese: o câncer de mama. Isso nos sugeriu que dados de ômicas, obtidos desse modelo, de forma geral, podem ser correlacionados com doenças humanas. Com isso em mente, nossos resultados do lipidoma e de proteoma poderão contribuir para uma melhor compreensão dos mecanismos moleculares de angiogênese patológica na retina e, talvez, em outras doenças dependentes da angiogênese.

Por exemplo, a análise de lipidômica em conjunto com a de transcriptômica identificou uma assinatura lipídica para a angiogênese patológica do modelo OIR, a qual destaca a esterificação do colesterol, formação de gotículas lipídicas, transporte reverso do colesterol e aumento da síntese de ácidos graxos n-9 (por exemplo, ácido de *mead*) como sendo processos celulares importantes na retinopatia. O *mead acid* já foi demonstrado como um indicador de deficiência de ácidos graxos essenciais (ICHI et al., 2014). Portanto, nossa sugestão é de que o *mead acid*, em alta concentração, possa ser utilizado como um marcador de retinopatia da prematuridade. De fato, isso está de acordo com estudos que indicam que os

baixos níveis do ácido graxo n-6 estão associados ao desenvolvimento de ROP (LÖFQVIST et al., 2018). A nossa história fica ainda mais interessante com a análise proteômica, a qual converge com a integração dos dados do transcriptoma e lipidoma, onde proteínas relacionadas às vias de lipoproteínas, colesterol, quilomicrons e triacilglicerol apresentam produção aumentada na retinopatia. Dentre elas, têm grande destaque as proteínas A2m, C3, Hpx, Alb, Apoa1, Apoa4, Cp, Hbb-bs, Serpinh1 e Sparc. É interessante observar que muitas delas são proteínas presentes no plasma, o que indica, novamente, a possibilidade de serem utilizadas como marcador molecular com uso diagnóstico.

Um artigo recente demonstrou que a proteína Alfa-2-macroglobulina (A2m), que é um inibidor de protease que regula a estabilidade e o *turnover* da matriz extracelular, tem a expressão induzida por VEGF e mediada pelo epitélio pigmentar da retina (RPE - *retinal pigment epithelium*) em células endoteliais da coroide do olho humano (LEHMANN et al., 2022). Isso é interessante, pois a função dos fotorreceptores, que são as células da retina que capturam os fótons recebidos no olho e os transformam em pulsos elétricos que, por fim, levam à percepção visual, depende do epitélio pigmentar da retina (RPE), uma camada de células adjacente aos fotorreceptores que permite a função visual reciclando componentes do ciclo visual, eliminando produtos residuais da retina e regulando o fluxo de íons e fluidos entre o espaço sub-retiniano e a coroide (STRAUSS, 2005). Disfunções na RPE ou dos vasos sanguíneos da coroide (como observado em doenças da retina, como a degeneração macular relacionada à idade) podem interromper alguns desses mecanismos, levando a alterações na homeostase da matriz extracelular da coroide, membrana de Bruch e função visual.

De acordo com a Organização Mundial da Saúde, a degeneração macular relacionada à idade (DMRI) é a principal causa de cegueira no mundo desenvolvido. A DMRI afeta pacientes com idade ≥ 55 anos e estima-se que existam 200 milhões de pessoas com DMRI no mundo e isso pode aumentar para 300 milhões em todo o mundo até 2040 (MITCHELL et al., 2018). A DMRI em estágio inicial inclui sinais clínicos como drusas (espécie de “cristais” no fundo do olho) e anormalidades do epitélio pigmentar da retina. Em estágio avançado, a DMRI pode ser neovascular (também conhecida como úmida) ou não neovascular (conhecida seca). Na DMRI não neovascular, há uma degradação gradual das células sensíveis à luz na mácula que transmitem informação visual ao cérebro e ao tecido de suporte sob a mácula. Já na DMRI neovascular, a forma mais grave desta doença, os vasos sanguíneos anormais crescem embaixo da retina por angiogênese patológica. Esses vasos podem apresentar vazamento de líquido e sangue, o que pode causar danos à mácula. A DMRI tardia resulta em

perda da acuidade visual central, levando a deficiência visual grave e permanente, o que tem grande impacto na qualidade de vida.

A proteína do complemento C3 (C3), que apresentou um grande destaque no transcriptoma, lipidoma e proteoma, além de ser um componente de HDL, desempenha um papel fundamental na fisiopatologia da DMRI. O sistema complemento é uma rede de proteínas altamente interativa que se torna ativada de forma semelhante a uma cascata, neutralizando rapidamente microorganismos ou sinais de estresse endógeno por meio de potentes mecanismos opsonofagocíticos e inflamatórios (RICKLIN et al., 2010). Ao coordenar a sinalização imune inata e adaptativa, o complemento contribui para a homeostase tecidual e a imunovigilância do hospedeiro. C3 tem uma importante posição dentro da cascata do complemento e tornou-se como um dos principais alvos terapêuticos em muitas doenças inflamatórias, incluindo DMRI (KIM et al., 2021). Estudos de associação do genoma revelaram que variações genéticas em vários componentes da cascata do complemento estão associadas a um risco aumentado de DMRI, apontando predominantemente para um papel patogênico chave da desregulação de via alternativa, levando ao aumento *turnover* C3 nesta doença (PARK; CONNOR; LAMBRIS, 2019).

A hemopexina (Hpx), também conhecida como beta-1B-glicoproteína, também já foi relatada em outras doenças oculares. Ela é sintetizada no fígado e liberada em alta concentração para combinar com o heme-livre e a hemoglobina-livre para proteger o corpo do dano oxidativo. A barreira hemato-retiniana (BRB - *blood-retinal barrier*) impede que Hpx plasmática entre na retina, porém, altas concentrações Hpx foram identificadas no fluido vítreo de pacientes diabéticos com edema macular sendo, provavelmente, um indicativo da quebra da integridade desta barreira e vazamento da BRB (HERNÁNDEZ; GARCIA-RAMÍREZ; SIMÓ, 2013). No entanto, fotorreceptores e células ganglionares também têm o potencial de expressar *Hpx* localmente na retina (CHEN et al., 1998). Em um estudo de proteoma do modelo de camundongo de uveíte induzida por endotoxina também foi apresentada alta produção de Hpx (ZHANG et al., 2022). A uveíte é uma condição inflamatória ocular grave da úvea, que é responsável por aproximadamente 10-15% dos casos de cegueira, segundo a Organização Mundial de Saúde (OMS). Ela é caracterizada por dor ocular, vermelhidão, fotofobia e perda da acuidade visual podendo ser desencadeada por infecções por bactérias ou vírus, ou por algumas doenças autoimunes sistêmicas, como a doença de Behçet, lúpus e doença de Vogt-Koyanagi-Harada (VKH) (LEE et al., 2017). No entanto, a causa exata da uveíte e como as respostas inflamatórias levam ao mau

funcionamento da retina e à perda da visão permanecem desconhecidos.

Gostaria de também chamar a atenção para as apolipoproteínas ApoA1 e ApoA4, presentes no proteoma da retina angiogênica. Alguns estudos epidemiológicos indicaram que essas lipoproteínas estão intimamente relacionadas com a incidência de retinopatia diabética (KLEIN et al., 1991). A retinopatia diabética é uma complicação importante da diabetes que ameaça muitos dos portadores desta doença com a perda da visão. Desenvolve-se gradualmente, apresentando alterações progressivas na microcirculação retiniana, levando a um aumento da permeabilidade vascular, hipoperfusão retiniana e proliferação vascular retiniana. Evidências associam a hiperlipidemia com complicações da retinopatia diabética, o excesso de colesterol se combina com proteínas, fosfolípidios e triglicerídeos para formar lipoproteínas. As lipoproteínas são compostas por uma parte interna feita de ésteres de colesterol hidrofóbicos e triglicerídeos, e uma parte externa que é feita de proteínas hidrofílicas chamadas apolipoproteínas, colesterol livre e fosfolípidios (BRYL et al., 2022). Um estudo realizado mostrou a expressão aumentada de ApoA1 nas retinas de pacientes diabéticos em comparação com pacientes sem diabetes mellitus (SIMÓ et al., 2009).

Como podemos observar, a presença das proteínas detectadas no nosso modelo se associa a diversas outras doenças oculares. Isso, de certa forma, corrobora para a validação do nosso modelo como uma ferramenta para estudos de doenças dependentes de angiogênese.

É importante destacar que este trabalho não é o primeiro proteoma descrito do modelo OIR. Um estudo realizado, utilizando a abordagem iTRAQ (*Isobaric Tags for Relative and Absolute Quantitation*), se restringiu a analisar apenas os tempos P12 e P17 da retinopatia, e identificou apenas metade das proteínas do nosso estudo (1.422 proteínas) (KIM et al., 2012). Neste trabalho, foi evidenciada a produção alterada pela retinopatia de proteínas cristalinas, proteínas associadas a células de Müller, proteínas associadas à neurodegeneração e proteínas associadas à angiogênese, como a proteína regulada por oxigênio de 150 kDa (ORP150). Com a abordagem de SWATH-MS (*Sequential Window Acquisition of All Theoretical Mass Spectra*), um segundo trabalho executou as análises nos pontos P13, P17 e P40, e identificou quase 3.000 proteínas. As cristalinas foram as proteínas mais proeminentes induzidas pela hipóxia na retina, enquanto as proteínas relacionadas à angiogênese, como a Filamin A e a miosina IIA, se destacam no pico da angiogênese (VÄHÄTUPA et al., 2018). Esses estudos trouxeram contribuições importantes, apresentaram as classes de proteínas mais abundantes, como também, disponibilizaram os dados. Além de termos coletado as nossas amostras nos

pontos P12, P15 e P17 para as amostras fisiológicas e R12, R12.5, R15 e R17 para as amostras patológicas, o que diferencia a nossa análise dos estudos prévios citados acima foi a abordagem que utilizamos (*Shotgun*), implicando em um perfil proteômico distinto. Isso nos mostra que diferentes técnicas e formas de análise do proteoma, podem apresentar estados de “flutuações” nos níveis de proteínas detectadas.

Finalmente, um diferencial importante do trabalho apresentado nessa tese é a integração de dados de ômicas. De maneira geral, em sistemas biológicos, alterações na expressão gênica resultam, mais tardiamente, em variações no proteoma, na produção de enzimas e outros fatores, que, por fim, irão resultar em alterações no perfil de metabólitos (como lipídios). Entender a dinâmica deste processo, como uma biologia de sistemas, é um passo importante para a elucidação de mecanismos moleculares e celulares, podendo, desta forma, identificar novos alvos terapêuticos e/ou de diagnóstico.

6. CONCLUSÃO DA TESE

As doenças dependentes de angiogênese, como a retinopatia da prematuridade e a retinopatia diabética, afetam crianças e jovens adultos, ainda na sua fase produtiva, podendo levar a perda significativa da visão ou mesmo cegueira. São, portanto, doenças com alto impacto na nossa sociedade. Atualmente, o tratamento para essas retinopatias ainda é limitado às fases iniciais da doença e com certo risco para o paciente (injeções intraoculares). No caso da retinopatia da prematuridade, a suplementação de oxigênio e nutricional nas unidades neonatais são fatores críticos para o sucesso do tratamento. Mas, a suplementação da dieta do bebê prematuro com ácidos graxos essenciais ainda é tema de debate e dúvida entre os médicos. Desta forma, é necessário entender melhor os mecanismos moleculares dessas doenças para buscar novas alternativas terapêuticas e nutricionais para o tratamento dessas doenças. Diante disso, neste trabalho, foram realizadas análises de transcriptoma, lipidoma e proteoma de um processo angiogênico *in vivo*, utilizando um modelo animal relevante para essas doenças, para uma melhor compreensão dos mecanismos celulares e de metabolismo das retinopatias causadas pela angiogênese patológica.

Com a integração dos dados das análises de transcriptômica e lipidômica, identificamos que no modelo de retinopatia da prematuridade ocorre intensa esterificação do colesterol e síntese de triacilglicerol, culminando na formação de gotículas lipídicas; concomitantemente, as vias de importação/exportação de colesterol estão aumentadas na retinopatia. Esses processos são importantes para combater stress oxidativo e, também, servem como fonte de energia para as células fotorreceptoras. E o fato mais importante que identificamos é que as retinas retinopáticas apresentam uma diminuição dos níveis de ácidos graxos poliinsaturados n-3 e n-6 e um aumento do n-9 da retina (*mead acid*). Os ácidos graxos n-3 e n-6 são essenciais para a saúde da retina e deficiência nessas vias pode ser um fator agravante na doença. Finalmente, o acúmulo de *mead acid* pode ser um possível marcador de severidade da doença; estudos futuros poderão avaliar essa possibilidade. Por último, os estudos de proteômica indicaram abundância de proteínas relacionadas às vias de lipoproteínas, colesterol, quilomicrons e triacilglicerol, convergindo com os dados do lipidoma e transcriptoma, corroborando os achados da lipidômica.

7. REFERÊNCIAS

ADAMS, R. H.; ALITALO, K. Molecular regulation of angiogenesis and lymphangiogenesis. **Nature Reviews Molecular Cell Biology**, v. 8, n. 6, p. 464–478, 2007.

AHRENS, C. H. et al. Generating and navigating proteome maps using mass spectrometry. **Nature Reviews Molecular Cell Biology**, v. 11, n. 11, p. 789–801, 2010.

ALON, T. et al. Vascular endothelial growth factor acts as a survival factor for newly formed retinal vessels and has implications for retinopathy of prematurity. **Nature Medicine**, v. 1, n. 10, p. 1024–1028, 1995.

ARMIROTTI, A.; DAMONTE, G. Achievements and perspectives of top-down proteomics. **Proteomics**, v. 10, n. 20, p. 3566–3576, 2010.

BALDASSARRE, M. et al. Filamins Regulate Cell Spreading and Initiation of Cell Migration. **PLoS One** v. 4, n. 11, 2009.

BENSIMON, A.; HECK, A. J. R.; AEBERSOLD, R. Mass spectrometry-based proteomics and network biology. **Annual Review of Biochemistry**, v. 81, p. 379-405, 2012.

BHARADWAJ, A. et al. Annexin A2 Heterotetramer: Structure and Function. **International Journal of Molecular Sciences**, v. 14, p. 6259-6305, 2013.

BRYL, A. et al. The Effect of Hyperlipidemia on the Course of Diabetic Retinopathy—Literature Review. **Journal of Clinical Medicine**, v. 11, n. 10, 2022.

BUENO, M. J.; MOURON, S.; QUINTELA-FANDINO, M. Personalising and targeting antiangiogenic resistance: A complex and multifactorial approach. **British Journal of Cancer**, v. 116, n. 9, p. 1119–1125, 2017.

CAMPOCHIARO, P. A. Molecular pathogenesis of retinal and choroidal vascular diseases. **Progress in Retinal and Eye Research**, v. 49, p. 67–81, 2015.

CARMELIET, P. et al. Abnormal blood vessel development and lethality in embryos lacking a single VEGF allele. **Nature**, v. 380, p. 435-439, 1996.

CARMELIET, P. Angiogenesis in health and disease. **Nature Medicine**, v. 9, n. 6, p. 653–

660, jun. 2003.

CARMELIET, P. Angiogenesis in life, disease and medicine. **Nature**, v. 438, n. 7070, p. 932–936, 2005.

CARMELIET, P.; JAIN, R. K. Molecular mechanisms and clinical applications of angiogenesis. **Nature**, v. 473, n. 7347, p. 298–307, 2011.

CHEN, J.; SMITH, L. E. H. Retinopathy of prematurity. **Angiogenesis**, v. 10, n. 2, p. 133–140, 2007.

CHEN, W. et al. Expression of the protective proteins hemopexin and haptoglobin cells of the neural retina. **Experimental Eye Research**, v. 67, n. 1, p. 83–93, 1998.

CHINTALGATTU, V. et al. Coronary microvascular pericytes are the cellular target of sunitinib malate-induced cardiotoxicity. **Science Translational Medicine**, v. 5, n. 187, 2013.

CONUS, S.; SIMON, H. U. Cathepsins: Key modulators of cell death and inflammatory responses. **Biochemical Pharmacology**, v. 76, n. 11, p. 1374–1382, 2008.

DROBNY, A. et al. The role of lysosomal cathepsins in neurodegeneration: Mechanistic insights, diagnostic potential and therapeutic approaches. **Biochimica et Biophysica Acta - Molecular Cell Research**, v. 1869, n. 7, p. 119243, 2022.

DROGA-MAZOVEC, G. et al. Cysteine cathepsins trigger caspase-dependent cell death through cleavage of bid and antiapoptotic Bcl-2 homologues. **Journal of Biological Chemistry**, v. 283, n. 27, p. 19140–19150, 2008.

ELLIS, L. M.; HICKLIN, D. J. VEGF-targeted therapy: Mechanisms of anti-tumour activity. **Nature Reviews Cancer**, v. 8, n. 8, p. 579–591, 2008.

FLIESLER, S. J. Introduction to the thematic review series: Seeing 2020: Lipids and lipid-soluble molecules in the eye. **Journal of Lipid Research**, v. 62, p. 100007, 2021.

FOLKMAN, J. Angiogenesis: An organizing principle for drug discovery? **Nature Reviews Drug Discovery**, v. 6, n. 4, p. 273–286, 2007.

FONG, G. H. et al. Role of the Flt-1 receptor tyrosine kinase in regulating the assembly of vascular endothelium. **Nature**, v. 376, p. 66-70, 1995.

FU, Z. et al. Fatty acid oxidation and photoreceptor metabolic needs. **Journal of Lipid Research**, v. 62, n. 26, p. 100035, 2021.

GEBERT, L. F. R.; MACRAE, I. J. Regulation of microRNA function in animals. **Nature Reviews Molecular Cell Biology**, v. 20, n. 1, p. 21–37, 2019.

GRAVES, P. R. et al. Molecular Biologist's Guide to Proteomics. **Microbiology and Molecular Biology Reviews**, v. 66, n. 1, p. 39–63, 2002.

GUARISCHI-SOUSA, R. et al. A transcriptome-based signature of pathological angiogenesis predicts breast cancer patient survival. **PLoS Genetics**, v. 15, n. 12, 2019.

HA, M.; KIM, V. N. Regulation of microRNA biogenesis. **Nature Reviews Molecular Cell Biology**, v. 15, n. 8, p. 509–524, 2014.

HERNÁNDEZ, C.; GARCIA-RAMÍREZ, M.; SIMÓ, R. Overexpression of hemopexin in the diabetic eye: A new pathogenic candidate for diabetic macular edema. **Diabetes Care**, v. 36, n. 9, p. 2815–2821, 2013.

HIRATSUKA, S. et al. Flt-1 lacking the tyrosine kinase domain is sufficient for normal development and angiogenesis in mice. **Proceedings of the National Academy of Sciences of the United States of America**, v. 95, n. 16, p. 9349–9354, 1998.

ICHI, I. et al. Identification of genes and pathways involved in the synthesis of Mead acid (20:3n - 9), an indicator of essential fatty acid deficiency. **Biochimica et Biophysica Acta - Molecular and Cell Biology of Lipids**, v. 1841, n. 1, p. 204–213, 2014.

IDE, A. G., BAKER, N. H., Warren, S.L. Vascularization of the Brown Pearce rabbit epithelioma transplant as seen in the transparent ear chamber. **American Journal of Roentgenology**, v. 42, p. 891-899, 1939.

JOYAL, J. S. et al. Retinal lipid and glucose metabolism dictates angiogenesis through the lipid sensor Ffar1. **Nature Medicine**, v. 22, n. 4, p. 439–445, 2016.

KIM, B. J. et al. Targeting complement components C3 and C5 for the retina: Key concepts and lingering questions. **Progress in Retinal and Eye Research**, v. 83, n. October 2020, p. 100936, 2021.

KIM, S. J. et al. Retinal proteome analysis in a mouse model of oxygen-induced retinopathy.

Journal of Proteome Research, v. 11, n. 11, p. 5186–5203, 2012.

KLEIN, B. E. K. et al. The Wisconsin Epidemiologic Study of Diabetic Retinopathy: XIII. Relationship of Serum Cholesterol to Retinopathy and Hard Exudate. **Ophthalmology**, v. 98, n. 8, p. 1261–1265, 1991.

KOWANETZ, M.; FERRARA, N. Vascular endothelial growth factor signaling pathways: Therapeutic perspective. **Clinical Cancer Research**, v. 12, n. 17, p. 5018–5022, 2006.

KUMAWAT, D. et al. Aggressive posterior retinopathy of prematurity: a review on current understanding. **Eye (Basingstoke)**, v. 35, n. 4, p. 1140–1158, 2021.

LAM, S. W.; JIMENEZ, C. R.; BOVEN, E. Breast cancer classification by proteomic technologies: Current state of knowledge. **Cancer Treatment Reviews**, v. 40, n. 1, p. 129–138, 2014.

LANGE, C. et al. Vascular endothelial growth factor: A neurovascular target in neurological diseases. **Nature Reviews Neurology**, v. 12, n. 8, p. 439–454, 2016.

LEE, J. H. et al. Viral posterior uveitis. **Survey of Ophthalmology**, v. 62, n. 4, p. 404–445, 2017.

LEHMANN, G. L. et al. Retinal Pigment Epithelium-Secreted VEGF-A Induces Alpha-2-Macroglobulin Expression in Endothelial Cells. **Cells**, v. 11, p.2975, 2022.

LIU, C. et al. Cytoplasmic SHMT2 drives the progression and metastasis of colorectal cancer by inhibiting β -catenin degradation. **Theranostics**, v. 11, n. 6, p. 2966–2986, 2021.

LÖFQVIST, C. A. et al. Association of retinopathy of prematurity with low levels of arachidonic acid a secondary analysis of a randomized clinical trial. **JAMA Ophthalmology**, v. 136, n. 3, p. 271–277, 2018.

LOKMAN, N. A. et al. The Role of Annexin A2 in Tumorigenesis and Cancer Progression. **Cancer Microenvironment**, v.4, p. 199–208, 2011.

LUTTUN, A.; TJWA, M.; CARMELIET, P. Placental Growth Factor (PlGF) and Its Receptor Flt-1 (VEGFR-1). **Annals of the New York Academy of Sciences**, v. 979, n. 1, p. 80–93, 2002.

MA, J. et al. Lipidomic analysis and diagnosis of glioblastoma multiforme with rapid

evaporative ionization mass spectrometry. **Electrophoresis**, v. 42, n. 19, p. 1965–1973, 2021.

MICHALOSKI, J. S. et al. Discovery of pan-VEGF inhibitory peptides directed to the extracellular ligand-binding domains of the VEGF receptors. **Science Advances**, v. 2, n. 10, 2016.

MITCHELL, P. et al. Age-related macular degeneration. **The Lancet**, v. 392, n. 10153, p. 1147–1159, 2018.

MONTEIRO, J. S. Investigações sobre os mecanismos moleculares da angiogênese com base em dados de expressão gênica num modelo murino, e sua aplicação no prognóstico do câncer de mama. Tese (Doutorado em Bioinformática) - Bioinformática, Universidade de São Paulo, São Paulo, 2022.

NEILSON, K. A. et al. Less label, more free: approaches in label-free quantitative mass spectrometry. **Proteomics**, v. 11, p. 535–553, 2011.

PARK, D. H.; CONNOR, K. M.; LAMBRIS, J. D. The challenges and promise of complement therapeutics for ocular diseases. **Frontiers in Immunology**, v. 10, n. MAY, p. 1–14, 2019.

PIERCE, E. A.; FOLEY, E. D.; SMITH, L. E. H. Regulation of vascular endothelial growth factor by oxygen in a model of retinopathy of prematurity. **Archives of Ophthalmology**, v. 114, n. 10, p. 1219–1228, 1996.

PIERCE, I. A. et al. Vascular endothelial growth factor/vascular permeability factor expression in a mouse model of retinal neovascularization. **Proceedings of the National Academy of Sciences of the United States of America**, v. 92, n. 3, p. 905–909, 1995.

PRIETO-FERNÁNDEZ, L. et al. Pathobiological functions and clinical implications of annexin dysregulation in human cancers. **Frontiers in Cell and Developmental Biology**, v. 10, n. September, p. 1–29, 2022.

RICKLIN, D. et al. Complement: A key system for immune surveillance and homeostasis. **Nature Immunology**, v. 11, n. 9, p. 785–797, 2010.

SHALABY, F. et al. **Failure of blood-island formation and vasculogenesis in Flk-1-deficient mice** *Nature*, 1995.

SHAMIM, A. et al. Lipids: An insight into the neurodegenerative disorders. **Clinical Nutrition Experimental**, v. 20, p. 1–19, 2018.

SIMÓ, R. et al. Apolipoprotein A1 Is Overexpressed in the Retina of Diabetic Patients. **American Journal of Ophthalmology**, v. 147, n. 2, p. 319- 325.e2, 2009.

SMITH, L. E. H. et al. Oxygen-induced retinopathy in the mouse. **Investigative Ophthalmology and Visual Science**, v. 35, n. 1, p. 101–111, 1994.

STRAUSS, O. The retinal pigment epithelium in visual function. **Physiological Reviews**, v. 85, n. 3, p. 845–881, 2005.

TYANOVA, S.; TEMU, T.; COX, J. The MaxQuant computational platform for mass spectrometry-based shotgun proteomics. **Nature Protocols**, v. 11, n. 12, p. 2301–2319, 2016.

VÄHÄTUPA, M. et al. SWATH-MS proteomic analysis of oxygen-induced retinopathy reveals novel potential therapeutic targets. **Investigative Ophthalmology and Visual Science**, v. 59, n. 8, p. 3294–3306, 2018.

VALLE-PÉREZ, B. et al. Filamin B plays a key role in vascular endothelial growth factor-induced endothelial cell motility through its interaction with Rac-1 and Vav-2. **The Journal of Biological Chemistry**, v. 285, n. 14, p. 10748–10760, 2010.

VIZOVIŠEK, M.; FONOVIĆ, M.; TURK, B. Cysteine cathepsins in extracellular matrix remodeling: Extracellular matrix degradation and beyond. **Matrix Biology**, v. 75–76, p. 141–159, 2019.

VOGEL, C.; MARCOTTE, E. M. Insights into the regulation of protein abundance from proteomic and transcriptomic analyses. **Nature Reviews Genetics**, v. 13, n. 4, p. 227–232, 2012.

WANG, T. et al. Crucial role of Anxa2 in cancer progression: highlights on its novel regulatory mechanism. **Cancer Biology & Medicine**, v. 16, n. 4, p. 671-687, 2019.

WANG, Z.; GERSTEIN, M.; SNYDER, M. The transcriptome is the complete set of transcripts in a cell, and their quantity. **Nature Reviews Genetics**, v. 10, n. 1, p. 57–63, 2009.

YANG, K.; HAN, X. Lipidomics: Techniques, Applications, and Outcomes Related to Biomedical Sciences. **Trends in Biochemical Sciences**, v. 41, n. 11, p. 954–969, 2016.

ZHANG, J. et al. Retinal Proteomic Analysis in a Mouse Model of Endotoxin-Induced Uveitis Using Data-Independent Acquisition-Based Mass Spectrometry. **International Journal of Molecular Sciences**, v. 23, n. 12, 2022.

1. APÊNDICE

Lista de proteínas do cluster 1 do *heatmap*

Proteínas do cluster 1	Gene	ID
Charged multivesicular body protein 4b	Chmp4b	Q9D8B3
Septin-2	Septin2	P42208
Carboxylesterase 1C	Ces1c	P23953
SPARC	Sparc	Q5NCU4
ATP-dependent RNA helicase DDX1	Ddx1	Q91VR5
Hexokinase	Hk2	E9Q5B5
Vimentin	Vim	P20152
H1 histone family, member X	H1fx	Q80ZM5
40S ribosomal protein S3	Rps3	Q5YLR3
Heterogeneous nuclear ribonucleoprotein A1	Hnrnpa1	Q3U7F3
Nucleolin	Ncl	Q8CD23
Serine/arginine-rich splicing factor 7	Srsf7	A0A3Q4EH04
Heterogeneous nuclear ribonucleoprotein L	Hnrnpl	Q3UMT7
ATP-dependent RNA helicase A	Dhx9	A0A087WPL5
60S ribosomal protein L13	Rpl13	Q5RKP3
Protein-arginine deiminase type-2	Padi2	Q08642
Cathepsin D	Ctsd	P18242
Tubulin polymerization-promoting protein family member 3	Tppp3	Q9CRB6
Ceruloplasmin	Cp	G3X9T8
Apolipoprotein A-IV	Apoa4	P06728
Hemopexin	Hpx	Q91X72
Ras GTPase-activating-like protein IQGAP1	Iqgap1	Q6ZQK2
40S ribosomal protein S6	Rps6	Q8BT09
ERO1-like protein alpha	Ero1l	Q4FK57
Transgelin-2	Tagln2	Q9WVA4
Serine hydroxymethyltransferase	Shmt2	Q9CZN7
Cell surface glycoprotein MUC18	Mcam	Q8R2Y2
Tropomyosin alpha-4 chain	Tpm4	Q6IRU2
Alpha-2-macroglobulin	A2m	Q61838
Tpm3 protein	Tpm3	Q58E70
Plastin-2	Lcp1	Q3U9M7
Moesin	Msn	P26041
Annexin	Anxa2	Q9CZI7
Complement C3	C3	P01027
Serpin B6	Serpinb6a	Q4FJQ6
Annexin	Anxa3	Q8C1X9
Filamin-B	Flnb	Q80X90
Alpha-actinin-1	Actn1	Q7TPR4
Gelsolin	Gsn	Q6PAC1

Apolipoprotein A-I	Apoa1	Q3V2G1
Cysteine and glycine-rich protein 1	Csrp1	Q4FJX4
Serpin H1	Serpinh1	Q8BVU9
Galectin-1	Lgals1	P16045
Serum albumin	Alb	P07724
Pro-cathepsin H	Ctsh	A0A087WR20
Filamin-A	Flna	B7FAV1
Vinculin	Vcl	Q64727
Annexin A5	Anxa5	P48036
Annexin	Anxa1	Q4FJV4
Retinal dehydrogenase 1	Aldh1a1	P24549
Hemoglobin subunit alpha	Hba-a1	Q91VB8
Beta-globin	Hbbt1	A8DUP7
Calumenin	Calu	Q3TUF3
Annexin	Anxa6	Q3UI56
Chloride intracellular channel protein 1	Clic1	Q9Z1Q5
Cathepsin B	Ctsb	Q3TVS6
Selenium-binding protein 1	Selenbp1	P17563
Cytosolic 10-formyltetrahydrofolate dehydrogenase	Aldh1l1	Q8R0Y6
Glutathione S-transferase Mu 1	Gstm1	P10649

Lista de proteínas do cluster 2 do *heatmap*

Proteínas do cluster 2	Gene	ID
Glutamate dehydrogenase 1, mitochondrial	Glud1	P26443
SEC14-like protein 2	Sec14l2	Q99J08
Recoverin	Rcvrn	Q2TB46
CB1 cannabinoid receptor-interacting protein 1	Cnrip1	Q5M8N0
Pyruvate dehydrogenase E1 component subunit alpha	Pdha1	Q3UFJ3
Retinoschisin	Rs1	B1AU64
Thioredoxin-dependent peroxide reductase, mitochondrial	Prdx3	P20108
Interphotoreceptor matrix proteoglycan 1	Impg1	Q8R1W8
CaM kinase-like vesicle-associated protein	Camkv	Q3UHL1
Interphotoreceptor matrix proteoglycan 2	Impg2	Q80XH2
Transgelin-3	Tagln3	Q9R1Q8
Protein kinase C	Prkca	Q4VA93
Phytanoyl-CoA hydroxylase-interacting protein-like	Phyhipl	Q8BGT8
Calretinin	Calb2	Q08331
F-actin-capping protein subunit beta	Capzb	Q923G3
Pyridoxal kinase	Pdxk	Q8K183
Fumarate hydratase, mitochondrial	Fh	P97807
Glycogen phosphorylase, muscle form	Pygm	Q9WUB3

Glyceraldehyde-3-phosphate dehydrogenase	Gapdh	P16858
Cytosolic acyl coenzyme A thioester hydrolase	Acot7	E9PYH2
WD repeat-containing protein 1	Wdr1	Q3TJY2
Calmodulin-like protein 3	Calm1	P0DP28
Phosphatidylethanolamine-binding protein 1	Pebp1	Q5EBQ2
Aconitate hydratase, mitochondrial	Aco2	Q99KI0
Transketolase	Tkt	P40142
Serine/threonine-protein phosphatase 2A catalytic subunit beta isoform	Ppp2cb	P62715
Neurexin-3	mKIAA0743	Q6ZQ56
Contactin-1	Cntn1	P12960
SH3 domain-binding glutamic acid-rich-like protein	Sh3bgr1	Q3U9A8
Insulin-degrading enzyme	Ide	Q8CGB9
Ubiquitin carboxyl-terminal hydrolase isozyme L3	Uchl3	Q9JKB1
NAD kinase 2, mitochondrial	Nadk2	Q8C5H8
Heat shock 70 kDa protein 4	Hspa4	Q3U2G2
Neurofascin	Nfasc	Q810U3
Ubiquitin carboxyl-terminal hydrolase isozyme L1	Uchl1	Q9R0P9
Profilin-2	Pfn2	Q9JJV2
Adenosine deaminase-like protein	Adal	Q80SY6
Carbonic anhydrase 3	Ca3	P16015
14-3-3 protein beta/alpha	Ywhab	Q9CQV8
Sepiapterin reductase	Spr	G3UXX3
Tenascin-R	Tnr	Q8BYI9
Peroxiredoxin-6	Prdx6	Q6GT24
Malate dehydrogenase, mitochondrial	Mdh2	P08249
Hypoxanthine-guanine phosphoribosyltransferase	Hprt	Q99KF5
L-lactate dehydrogenase B chain	Ldhb	A0A618MX27
Isocitrate dehydrogenase [NADP]	Idh1	Q5HZJ8
Glyceraldehyde-3-phosphate dehydrogenase	Gapdh	S4R1W8
Adenylate kinase isoenzyme 1	Ak1	Q9R0Y5
Pyruvate dehydrogenase E1 component subunit beta, mitochondrial	Pdhb	Q9D051
Single-stranded DNA-binding protein	Ssbp1	Q8R2K3
Alpha-1,4 glucan phosphorylase	Pygb	Q3V3U0
Pyridoxal phosphate phosphatase	Pdpx	P60487
Glutamine synthetase	Glul	P15105
Calbindin	Calb1	P12658
Superoxide dismutase	Sod2	Q4FJX9
Carbonic anhydrase 2	Ca2	P00920
Pyruvate carboxylase	Pcx	G5E8R3
Discs large MAGUK scaffold protein	Dlg2	A0A2L2P595
Succinate-semialdehyde dehydrogenase, mitochondrial	Aldh5a1	B2RS41
Secretagoin	Scgn	Q91WD9
F-box only protein 22	Fbxo22	Q78JE5
Rab GDP dissociation inhibitor alpha	Gdi1	P50396
Branched-chain-amino-acid aminotransferase	Bcat1	Q3TJN1
Fatty acid-binding protein, heart	Fabp3	Q5EBJ0

Non-specific serine/threonine protein kinase	Pak3	B1GX80
Aspartate aminotransferase, mitochondrial	Got2	P05202
Visinin-like protein 1	Vsn11	Q4W4C9
Protein IMPACT	Impact	O55091
Elongation factor 1-alpha 2	Eef1a2	P62631
Malate dehydrogenase, cytoplasmic	Mdh1	P14152
Prolyl endopeptidase-like	Prepl	Q8BKS6
THUMP domain-containing protein 1	Thumpd1	Q99J36
10 kDa heat shock protein, mitochondrial	Hspe1	Q64433
Protein unc-119 homolog A	Unc119	Q3V299
Aspartate aminotransferase, cytoplasmic	Got1	P05201
Hydroxyacylglutathione hydrolase, mitochondrial	Hagh	A0A0R4J052
14-3-3 protein theta	Ywhaq	A3KML3
Secernin-1	Scrn1	Q9CZC8
Dihydropteridine reductase	Qdpr	Q8BVI4
Peptidyl-prolyl cis-trans isomerase	Ppia	Q5SVY2
Spermidine synthase	Srm	Q8BSZ8

SÚMULA CURRICULAR

DADOS PESSOAIS

Nome: Lilian Cristina Costa Alecrim de Oliveira

Local e data de nascimento: Apucarana-PR, 22/02/1992

EDUCAÇÃO

2017 – 2023 Doutorado em Ciências Biológicas (Bioquímica)
 Universidade de São Paulo, São Paulo-SP
 Orientador: Prof. Dr. Ricardo José Giordano

2010 – 2015 Graduação em Química (Licenciatura)
 Universidade Estadual de Maringá, Maringá-PR

OCUPAÇÃO

Bolsista de Doutorado Direto, Coordenação de Aperfeiçoamento de Pessoal de Nível Superior (CAPES), vigência da bolsa 08/2019-01/2023

Bolsista de Mestrado, Coordenação de Aperfeiçoamento de Pessoal de Nível Superior (CAPES), vigência da bolsa 10/2017-08/2019

PUBLICAÇÕES

Artigos

Guarisch-Sousa, R., Monteriro, J.S., **Alecrim, L.C.**, Michaloski, J.S., Cardeal, L.B., Ferreira, E.N., Carraro, D.M., Nunes, D.N., Dias-Neto, E., Reimand, J., Boutros, P.C., Setubal, J.C., Giordano, R.J. A transcriptome-based signature of pathological angiogenesis predicts breast cancer patient survival. *PLoS Genetics*, v. 15, n. 12. Dec. 2019.

Alecrim, L.C., Inague, A., Monteiro, J.S., Yoshinaga, M.Y., Setubal, J.C., Miyamoto, S., Giordano, R.J. Oxygen-induced pathological angiogenesis promotes intense lipid synthesis and remodeling in the retina. *Manuscripto submetido*.

Resumos

Alecrim, L.C., Inague, A., Monteiro, J.S; Yoshinagua, M.Y.; Setubal, J.C.; Giordano, R.J. An integrated study of transcriptome, lipidome and proteome in search of new therapeutic targets for pathological angiogenesis. 50th Annual Meeting of The Brazilian Biochemistry and Molecular Biology Society. 2021

Piccirillo, E., **Alecrim, L.C.**, Amaral, A.T., Giordano, R.J. Identification of novel class of VEGF inhibitors using virtual screening. 50th Annual Meeting of The Brazilian Biochemistry and Molecular Biology Society. 2021

Inague, A.; **Alecrim, L.C**; Monteiro, J.S; Yoshinagua, M.Y.; Setubal, J.C.; Giordano, R.J.; Miyamoto, S. Lipidomic analysis reveals changes in lipid metabolism in a mouse model of retinal pathological angiogenesis. Keystone Symposia – Lipidomics and Function Metabolic Pathways in Disease. 2019

Inague, A.; **Alecrim, L.C**; Monteiro, J.S; Yoshinagua, M.Y.; Setubal, J.C.; Giordano, R.J. Lipidomic Analysis reveals changes in lipid metabolism in a mouse model of retinal pathological angiogenesis. Tsukuba Conference. 2019

Oliveira, L.C.A.; Guarischi-Sousa, R.; Tang, F.H.F.; Boutros, P.C.; Setubal, J.C.; Giordano, R.J.. The oxygen-induced retinopathy mouse model for drug discovery in angiogenesis. 47th Annual Meeting of The Brazilian Biochemistry and Molecular Biology Society. 2018

MONITORIA EM DISCIPLINADA GRADUAÇÃO

QBQ2457 - Tecnologia do DNA Recombinante - Instituto de Química, Universidade de São Paulo, 2020.

FORMAÇÃO COMPLEMENTAR

III Workshop em Bioterismo – Inovação e Capacitação. Biotério do Departamento de Parasitologia do Instituto de Ciências Biomédicas da Universidade de São Paulo, 2017.